Laser Direct-Write Fabrication of MEMS

by

Prashant Patil

S.M., Massachusetts Institute of Technology (2013)
M.Tech., Engineering Physics & Nanoscience
Indian Institute of Technology, Bombay (2011)
B.Tech., Engineering Physics
Indian Institute of Technology, Bombay (2011)

Submitted to the Program in Media Arts and Sciences,
School of Architecture and Planning
in partial fulfillment of the requirements for the degree of

Doctor of Philosophy

at the

MASSACHUSETTS INSTITUTE OF TECHNOLOGY

September 2019

© Massachusetts Institute of Technology 2019. All rights reserved.

Author . . . .
Program in Media Arts and Sciences
School of Architecture and Planning
August 9, 2019

Certified by . . . .
Neil Gershenfeld
Director, Center for Bits and Atoms
Thesis Supervisor

Accepted by . . . .
Tod Machover
Academic Head, Program in Media Arts and Sciences

Laser Direct-Write Fabrication of MEMS

by

Prashant Patil

Submitted to the Program in Media Arts and Sciences,
School of Architecture and Planning
on August 9, 2019, in partial fulfillment of the
requirements for the degree of
Doctor of Philosophy

Abstract

Micro-electromechanical systems (MEMS) have many applications in healthcare, consumer electronics, and automobile industry. Unfortunately, the development of novel MEMS is significantly hindered by the limitations of the state-of-the-art MEMS microfabrication processes such as high cost of equipment ownership, long development time, and limited choice of fabrication material selection and integration. Recent developments in alternate MEMS fabrication processes such as PCB-MEMS, laminate MEMS, pop-up book MEMS, and soft-MEMS have reduced fabrication cost, increased material choice, and facilitated material integration. However, MEMS fabricated using these methods have a large lateral feature size, and low aspect ratio as compared to MEMS produced utilizing conventional deep reactive ion etching (DRIE) microfabrication process. Moreover, fabricating MEMS with six degrees of freedom (DOF) free-standing microstructures using these processes is challenging. Finally, the choice of fabrication material is relatively limited, and each material requires a separate manufacturing process.

This thesis presents a novel MEMS fabrication process called multi-lamina assembly of laser micromachined laminates (MALL), which can fabricate MEMS comparable to DRIE, enable creating free-standing microstructures with six degrees of freedom, and further expand the choice of fabrication material. Moreover, the proposed approach offers a single microfabrication method to process a wide range of materials. A novel microfabrication process called laser-assisted material phase-change and expulsion (LAMPE) micromachining is developed. Using this process, the fabrication of high aspect ratio structures with lateral features as small as $10\mu m$, and aspect ratio as large as 10:1 is demonstrated in metals, silicon, and diamond. Previously, such high aspect ratio and small lateral feature structures could be fabricated in silicon alone using the deep reactive ion etching process.

The LAMPE micromachining process is used to manufacture individual layers of a MEMS. Subsequently, the micromachined laminates are stack assembled and bonded to construct MEMS devices. Using the MALL process, fabrication of six degrees of freedom free-standing structures as thin as $10\mu m$ is demonstrated. In addition, the gap between the free-standing structure and the substrate can be as small as $12.5\mu m$. The utility of the MALL process is demonstrated by fabricating three MEMS. First, an electrostatic comb-drive actuator is fabricated using copper as the structural material. The distance

between the comb-drive fingers is $10\mu m$, and the thickness of the fingers is $100\mu m$. This is the first demonstration of using metal to fabricate comb-drive structure with such small lateral feature and high aspect ratio. Second, a MEM relay for high-current switching application is demonstrated. The current carrying capacity of the MEM relay is higher than $100mA$. Finally, the development of high-aspect-ratio diamond rotors for enhancing the resolution of magic-angle spinning nuclear magnetic resonance spectroscopy (MAS-NMR) is presented. This is the first demonstration of micromachining such ultra-deep (5 mm), and ultra-high aspect ratio (10:1) holes in the diamond.

The MALL process can manufacture MEMS comparable to the conventional DRIE microfabrication process. Moreover, the manufacturing cost per device in the MALL is less than DRIE. However, DRIE offers a high part production rate than MALL. The part production rate in MALL can be matched with DRIE using multiple laser sources. For matching the part production rate, the investment required to purchase a laser micromachining tool with multiple lasers is comparable to the cost of a DRIE tool. Thus, an equal investment in MALL and DRIE results in an equal part production rate. The MALL process significantly reduces the time required for material integration, process development, and design iteration. As a result, the MEMS device development time is reduced from many months (in DRIE) to a day. The MALL process empowers rapid testing of new MEMS concepts and theory. Moreover, MALL can be used to fabricate one-of-a-kind MEMS devices and used for low-volume production, where initial high investment can not be justified.

The MALL process enables greater material selection and integration, rapid development, and integrated packing, thereby empowering a new paradigm in MEMS design, functionality, and application. The tools and material cost of MALL fabrication can be as low as $\$25,000$, which is affordable to a wider scientific community. The low capital investment and use of low-cost materials enable MEMS fabrication for masses and can expedite the development of novel MEMS.

Thesis Supervisor: Neil Gershenfeld
Title: Director, Center for Bits and Atoms

Laser Direct-Write Fabrication of MEMS

by

Prashant Patil

This dissertation has been reviewed and approved by the following committee members:

Carol Livermore . . . .

Associate Professor of Mechanical Engineering

Mechanical and Industrial Engineering

Northeastern University

Jeffrey Lang . . . .

Professor of Electrical Engineering

Electrical Engineering and Computer Science

Massachusetts Institute of Technology

Acknowledgments

I would like to express my deepest gratitude to my advisor, Neil Gershenfeld. Without your guidance and encouragement, this work would not have been possible. Thank you for putting your time and energy in mentoring me, providing space and resources, and fostering my creativity. The Truth is Empowering. Neil, thank you for providing honest constructive criticism and advises. For shaking my self-satisfying assumptions, raising my bar for achievement, and from a place of care, pushing me beyond my comfort zone. You taught me to think big, ask difficult questions, tackle hard problems, and push the envelope of what is possible. Thank you for believing in me.

I would also like to extend my deepest gratitude to my thesis committee - Carol Livermore and Jeffrey Lang - for their unwavering guidance. I am extremely grateful to be mentored by you. Thank you for taking the time to periodically meet with me, helping solve my problems, providing invaluable insights, and sharing your extensive knowledge. The completion of my dissertation would not have been possible without your guidance.

I also wish to thank Joe Jacobson, Shuguang Zhang, Ed Boyden, and Robert Griffin for their suggestions and collaborations.

CBA is a special place. It is a perfect fit for many misfits like myself. Neil, thank you for creating such a wonderful place and making me part of it. I will certainly miss this place.

Special thanks to Nadya for being a dear friend over many years. Meeting you at the MIT-India workshop in India was certainly the most life-changing moment of my life, and has led to this fascinating journey. My early days in the US were difficult, but you made them much easier.

I cannot leave CBA without mentioning Joe, who has been there from the beginning and done many behind-the-scene work which has made this thesis possible. Joe, thank you for everything, for many life advises, creative nicknames, and many interesting conversations. I will miss it. I would also like to extend my sincere thanks to CBA staff James, Kara, Tom, John, and Ryan. Thank you for operating everything smoothly, creating a sense of community, and sharing many lunches together. Thanks should also go to Jamie. Thank you Jamie, for being a dear friend, and for many proofreading sessions (and for secretly correcting my English).

I am extremely grateful to my cohort-mates Will, Sam, and Noah. Thank you for many brainstorming sessions, encouragement, and training sessions. Thank you for being generous with your time and entertaining my never-ending CAD/CAM/FAB questions. Many thanks to Ben for entertaining conversations, and letting me be Yoko's work dad (read fun dad).

I'd like to thank my dear friend, Filippos. Thank you for being there during my high and low, and for introducing me to Greek culture. I will miss our entertaining conversations about research, academics, and Greece. I'd like to thank Patritsia for helping me with my presentation and documents. Thank you for all the encouragement, appreciation, and friendship. I'd like thank Charles for building the lab together, many conversations, road trips, and friendship over the year. I'd like to thank Sarah Hovsepian, you were the first friend made in the US. Thanks for friendship over the year.

Thank you, Sherry and Neil, for introducing me to the amazing world for fablab.

I wish to thank CBA family - Amira, Erik, Jake, Sara, James P, Eric W., Matt C., Matt K., Soma, Amanda, Grace, Kenny, Rehmi, Kimin Jun, Manu Prakash, and Ara. I

had a great pleasure working with you, learning from you, and hanging out with you. Many thanks extended family at molecular machine - Pranam, Lisa, and Rui. I also wish to thank Dan and Salima for collaborating on the diamond rotor project. Thanks should also go to Bianca and Sunny for helping with building the laser micromachining system.

I would like to extend my sincere thanks to Amna, Joseph, Anirudh, and Kshitij. You have made my stay at MIT extra special. I will forever cherish those MIT days (and night outs). Many thanks to the design innovation workshop team, Dolly, Paul Anand, Anna, and Misha. I'd like to thank Rajesh for making me part of his workshop series, for many years of friendship, and mentorship.

Many thanks to Pragun, Dhairya, Udayan, Shrishti, Harshit, Harpreet, Santosh, Pranav, Neil, Tanuj, Vishal, Jitendra and Deepak. Many thanks to JNV, Betul friends Apurve, Hemant, Lalchand, Dinesh, Kumudini, Kepin, Surendra, Shivendra, Kamlesh, and all my classmates. Special thanks to folks at MIT Yoga club.

I am also grateful to my previous mentors Prof. Subhabhrata Dhar, Prof. S.S. Major, and Dr. So-Hye Cho. And many thanks to my previous lab mates at IIT Bombay - Jitendra, and Hari.

Special thanks to little furry friends Rumba, Eddy, Yoko, Lola, Penelope for bringing joy in my life.

I'd like to thank my high-school teacher Shamim Turki ma'am for admitting me to Jawahar Navodaya Vidyalaya, Betul. There is an old saying, "If you change the beginning of the story, you change the whole story". Ma'am, you have changed my story.

Thank you Nupur, for our special friendship, for encouraging me to be my best, and always supporting me. Thank you for being with me in this journey; your presence made every part of it wonderful.

Finally, I'd like to thank my parents - Mom and Dad, you have made so many sacrifices for me. Your unconditional love and support has made me who I am today. Many thanks to my brother Rinku, bhaiya you have been my first science teacher, thank you for infecting me with your tinkering habits. My sister Pranjali for pampering me when I was a baby, and my sister Pranoti for many life lessons.

Contents

Appendices **9**

1 Introduction **16**

1.1 Motivation . . . 16

1.2 Background . . . 18

1.2.1 PCB-MEMS . . . 18

1.2.2 Laminate MEMS . . . 18

1.2.3 Pop-up Book MEMS . . . 20

1.2.4 Limitations of Laser Micromachining . . . 20

1.3 MALL . . . 22

1.3.1 LAMPE Micromachining . . . 22

1.3.2 Electro-deburring . . . 24

1.3.3 Multi-Lamina Assembly . . . 24

1.4 Comparison with Prior Work . . . 25

1.4.1 High Aspect Ratio & Small Lateral Feature . . . 26

1.4.2 Freestanding Structures with Six Degrees of Freedom . . . 27

2 Theory of Pulsed Laser Ablation **30**

2.1 Pulsed Laser Ablation . . . 30

2.2 Laser-Micromachining System . . . 32

2.2.1 Laser Source . . . 33

2.2.2 Beam Delivery & Focusing Optics 36
2.2.3 Motion System 39
2.3 Summary 40

3 Laser-assisted Material Phase-change & Expulsion 41

3.1 Introduction 41
3.2 LAMPE 43
3.2.1 Difference between PLA and LAMPE Micromachining 45
3.3 Feature Size in LAMPE Micromachining 46
3.3.1 Experiment & Results 47
3.3.2 Analytical Model 48
3.3.3 Numerical Simulation 52
3.4 LAMPE High-Aspect-Ratio Micromachining 55
3.5 Electro-deburring of LAMPE Micromachined Parts 58
3.6 LAMPE Micromachining of Silicon 60
3.6.1 Introduction 60
3.6.2 Numerical Simulation 65
3.6.3 Results & Discussion 67
3.7 Conclusions 70

4 MALL MEMS Fabrication 72

4.1 Multi-Lamina Assembly 73
4.2 Comb-Drive Actuator 75
4.2.1 Design 75
4.2.2 Fabrication 78
4.2.3 Results & Discussion 80
4.2.4 Time Required for First Prototype 83
4.3 Micro-Electromechanical Relay 86
4.3.1 Design 86

4.3.2 Fabrication . . . 91
4.3.3 Results & Discussion . . . 94
4.4 Diamond Rotor . . . 99
4.4.1 Introduction . . . 99
4.4.2 Diamond Rotor . . . 100
4.4.3 Laser Micromachining of Diamond . . . 101
4.4.4 Theoretical Explanation . . . 101
4.5 Conclusions . . . 104
5 Discussion & Conclusion **106**
5.1 Advantages of MALL . . . 106
5.1.1 Greater Choice of Fabrication Materials . . . 106
5.1.2 Fabrication with Incompatible Materials . . . 107
5.1.3 Low-Cost Fabrication . . . 107
5.1.4 Rapid Development . . . 110
5.1.5 Integrated Packaging . . . 112
5.2 Limitations of MALL . . . 112
5.2.1 Inadequate for Fabricating 2.5D Structures . . . 112
5.2.2 Limit on Minimum Thickness of Microstructures . . . 113
5.2.3 Limit on the Gap Between Laminates . . . 116
5.2.4 Poor Alignment Accuracy . . . 117
5.2.5 Heat Affected Zone . . . 117
5.3 Volume Manufacturing . . . 117
5.4 MEMS for Masses . . . 119
5.5 Thesis Contributions . . . 122
5.6 Conclusion . . . 123
5.7 Recommendations for Future Work . . . 124

A **126**

A.1 Manufacturing Cost Estimates for DRIE and MALL 126

A.1.1 Cost of Manufacturing Using DRIE 127

A.1.2 Cost of Manufacturing Using MALL 128

B **131**

B.1 Equipment Required for MALL Fabrication 131

B.2 MEMS Design 133

B.3 Fabrication 133

B.3.1 Laser Micromachining 133

B.3.2 Electro-deburring 134

B.3.3 Lamination Process 135

B.4 MEMS Device Testing 136

B.5 Things That did Not work 136

List of Figures

1-1 Literature review of alternate MEMS fabrication methods. 19

1-2 Literature review of laser micromachining 21

1-3 Schematic diagram of MALL fabrication process. 23

1-4 Schematic diagram of multi-lamina assembly. 25

1-5 Schematic diagram of surface micromachining process. 27

2-1 Schematic diagram of pulsed laser ablation (PLA) process. 31

2-2 The plot of the average power , P_{avg} with respect to the pulse frequency . . . 34

2-3 The plot of pulse energy, E_p with respect to the pulse frequency. 34

2-4 The plot of peak power (left) and pulse intensity (right)with respect to the pulse frequency. 35

2-5 Intensity profile of the focused laser beam. 38

3-1 Schematic diagram of the LAMPE micromachining process. 44

3-2 Comparison of lateral features produced in PLA and LAMPE micromachining 46

3-3 Minimum feature size achievable using LAMPE micromachining. 48

3-4 Electro-deburring of LAMPE micromachined crater. 49

3-5 Pulse exposure with varying pitch distance to confirm material melting & expulsion. 53

3-6 Simulation of LAMPE micromachining of copper 56

3-7 High-aspect-ratio microfabrication using LAMPE micromachining 57

3-8 SEM image showing resolidified melt ejects. 58

3-9 Polarization curve of copper in phosphoric acid. 59
3-10 Electro-deburring of LAMPE micromachined parts. 61
3-11 High aspect ratio interdigitated fingers fabricated using LAMPE micromachining. 62
3-12 Pulsed laser ablation (PLA) of silicon. 63
3-13 The cross-section image showing laser-assisted oxidation of silicon. 65
3-14 The optical microscope & energy dispersive x-ray spectroscopy (EDS) image confirming oxidation of silicon 66
3-15 Simulation of LAMPE micromachining of silicon. 68
3-16 Example of high-aspect-ratio microstructures fabricated using LAMPE micromachining of silicon. 69

4-1 Alignment accuracy of multi-lamina assembly. 74
4-2 Schematic diagram of comb-drive actuator. 76
4-3 Fabrication of comb-drive device layer using LAMPE micromachining of copper. 78
4-4 Electro-deburring of LAMPE micromachined comb-drive structure. 79
4-5 Layers of the comb-drive actuator fabricated using LAMPE micromachining . 80
4-6 Assembled and bonded layers of the comb-drive actuator 81
4-7 SEM image of the fabricated comb-drive actuator. 81
4-8 Features of the fabricated comb-drive actuator. 82
4-9 Displacement measurement of comb-drive actuator fingers. 83
4-10 Schematic diagram of the micro-electromechanical (MEM) relay. 87
4-11 The bottom view of the actuator electrode showing movable contact and the insulating polyimide layer. 88
4-12 Schematic diagram showing design parameters of the the MEM relay. 89
4-13 Optical microscope image of the fabricated actuator electrode of MEM relay. 92
4-14 SEM image of the fabricated substrate layer of MEM relay. 93
4-15 Fabricated MEM relay. 95

4-16 The source-drain current-voltage measurement at various gate voltage. 96
4-17 The SEM images showing the operation of the MEM relay. 96
4-18 The current I_D vs. time plot of MEM relay demonstrating current switching. 97
4-19 Damaged polyimide insulating layer due to the dielectric break down of air . . 98
4-20 Maximum theoretical MAS frequency for various diameter rotors. 100
4-21 Schematic diagram showing the dimensions of the diamond rotor 101
4-22 Laser micromachined inner and outer diameter of diamond rotor.. 102
4-23 The transmittance and absorption coefficient of CVD grown diamond. 103
4-24 The optical penetration depth of CVD diamond. 104

5-1 Cost of fabricating the comb-drive actuator using DRIE and MALL process. . 108
5-2 Cost of fabricating MEM relay using DRIE and MALL process. 110
5-3 Fabrication of 2.5D structure in silicon using laser-micromachining followed by anisotropic etch 113
5-4 Fabrication of 2.5D structures using micro-milling. 114
5-5 Manipulation and laser micromachining of ultra-thin metal foils using a rigid frame. 115
5-6 The $12.5\mu m$ gap between the freestanding structure and the substrate fabricated using $12,5\mu m$ thick adhesive layer. 116
5-7 Part production rate of MEM relay fabrication using DRIE and MALL process.119

B-1 Broken comb-drive actuators 138
B-2 More broken comb-drive actuators 139
B-3 MEM relay designs tested in this work 141
B-4 Broken MEM relays 143
B-5 Failed attempt to fabricate comb-drive in nitride wafer 144

Chapter 1

Introduction

1.1 Motivation

Micro-electromechanical systems (MEMS) have many applications in fields like healthcare, consumer electronics, automobile, and energy. However, the development of novel MEMS devices has been significantly hindered by several limitations of the lithography-based microfabrication processes used to manufacture MEMS. First, these processes require access to expensive microfabrication tools such as photolithography systems, mask aligners, and deposition and etching tools. Moreover, these processes have a lengthy process development time. The high cost of equipment ownership and long development time associated with the lithography-based microfabrication processes makes them unsuitable for research and development, and low-volume MEMS production.

Second, the fabrication material is largely restricted to silicon and related materials such as silicon oxide and silicon nitride. The restriction in the choice of fabrication material limits the variety of MEM systems that can be designed and fabricated. For example, magnetic MEMS can potentially have distinct advantages over electrostatic/piezoelectric actuators such as high strength, polarity, and long actuation distance. However, fabricating magnetic MEMS is challenging due to the incompatibility of magnetic materials with lithography-based MEMS fabrication processes [1]. Furthermore, the performance of MEMS devices

is compromised due to the restricted choice of fabrication materials. For example, even though spring steel is an excellent choice for making high-performance micro-springs for MEMS, generally silicon is used because spring steel is incompatible with lithography-based MEMS fabrication processes.

Finally, during MEMS design and fabrication, integrating various materials and corresponding fabrication process is often the most difficult task [2]. In the lithography-based fabrication process, MEM systems are fabricated in monolithic fashion by successive deposition and patterning layers of materials. Each material layer is deposited and patterned using a unique process, which must be compatible with the previously deposited materials. However, integrating these processes is difficult due to material incompatibilities, thermal constraints (for example, polymeric parts cannot be subjected to high-temperature processing step such as LPCVD silicon deposition), and mechanical stability of interim structures. In summary, the conventional lithography-based MEMS fabrication processes are costly, offer a limited choice of fabrication materials, and the integration of various materials is challenging.

In this thesis, I present a novel approach for MEMS fabrication to overcome the above mentioned limitations. This approach uses multi-lamina assembly of laser micromachined laminates to fabricate MEMS and consists of two steps. First, the individual microstructure laminates are fabricated using direct-write laser-micromachining process. Next, the fabricated microstructure laminates are stack assembled and bonded to fabricate MEM systems. The presented MALL MEMS fabrication process enables greater material section and integration, low-cost manufacturing, rapid development, and integrated packaging.

Section 1.2 reviews the current work on laminate assembly and laser-micromachining. Section 1.3 presents the MALL process and its application in fabricating MEMS. Finally, section 1.4 compares the MALL process with prior work.

1.2 Background

In recent years, there has been a considerable interest in developing alternative fabrication methods to manufacture MEM systems. These fabrication methods and their limitations are discussed in the following sections:

1.2.1 PCB-MEMS

PCB-MEMS utilizes printed circuit board (PCB) fabrication technology to fabricate MEM systems. Figure1-1(a), (b), and (c) shows mesoscale RF MEMS switches fabricated using PCB technology [3][4][5]. The functionalities and performance of these PCB-MEMS have been far from the MEMS fabricated using conventional lithography-based processes. This is due to several limitations of the PCB fabrication technology. First, the minimum feature size produced using PCB fabrication technology is larger than the feature size achievable in lithography-based microfabrication processes. Moreover, the aspect ratio of the fabricated structures is less than the aspect ratio achievable in conventional microfabrication processes such as deep reactive ion etching (DRIE). Second, the fabrication material is limited to materials available for PCB manufacturing such as copper foils, FR4, and certain polymers [6]. Finally, the alignment accuracy achievable in PCB technology is an order larger than the alignment accuracy required for silicon-based MEMS [3].

1.2.2 Laminate MEMS

Another method that is used to fabricate MEMS is laminate MEMS. In the laminate MEMS fabrication process, first, individual layers of the MEM systems are fabricated using various post semiconductor manufacturing (PSM) processes, and then the fabricated layers are laminated to manufacture MEMS. Since individual layers are fabricated separately, the lamination process enables the fabrication of MEMS from heterogeneous materials with incompatible fabrication processes. Some examples of laminate MEMS that are reported in the literature are optical waveguide switch [7](figure1-1(d)), magnetically actuated micro-

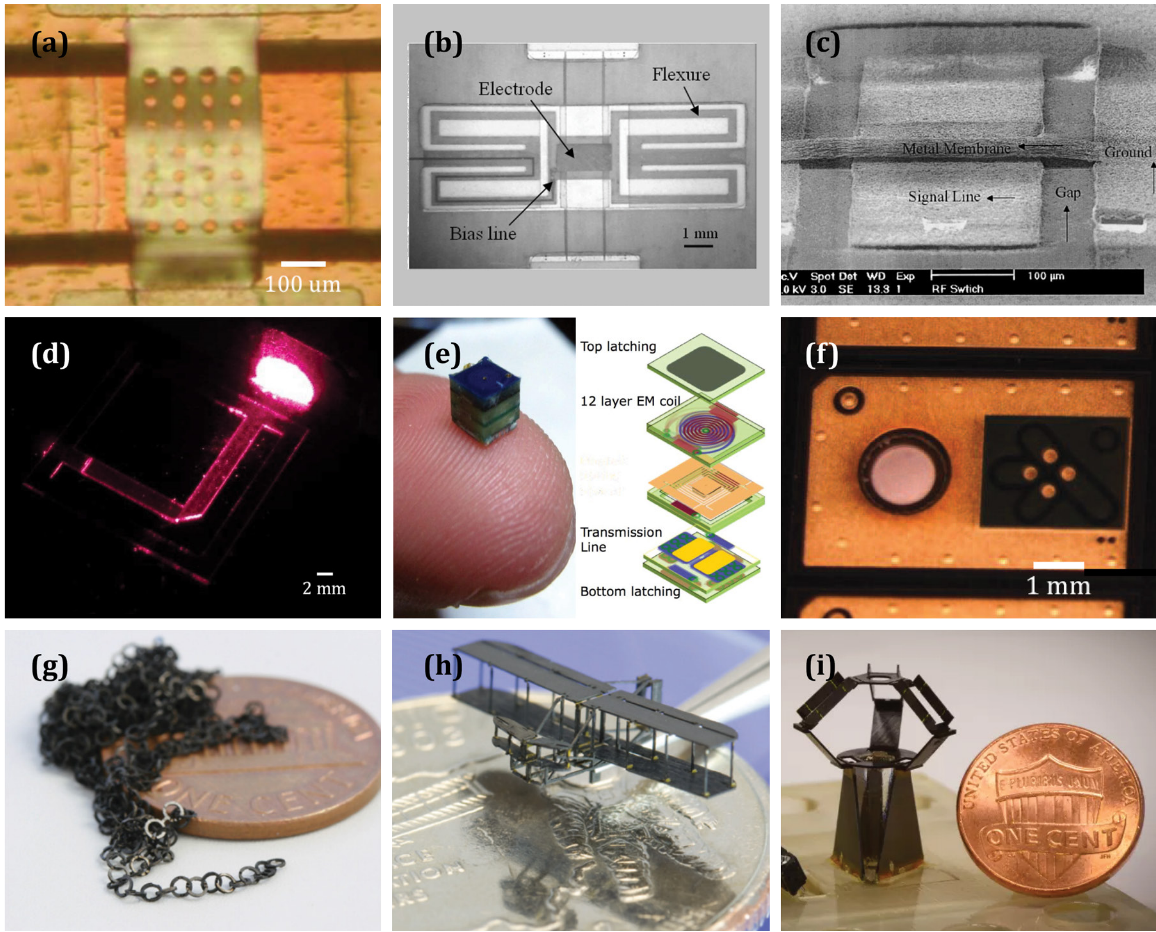

Figure 1-1: (a), (b) & (c) Mesoscale RF MEMS switches fabricated using PCB manufacturing technology [3][4][5]. (d) Optical waveguide switch fabricated using laminate MEMS technology [7]. (e) Laminate MEMS magnetically actuated micro-switch [8]. The device measures $3.2mm \times 3.2mm$. (f) MEMS Microphone fabricated using laminate MEMS [9]. (g) & (h) Meso-scale micro-structures fabricated using Pop-Up MEMS [9] . (i) Millimeter-scale robots fabricated using Pop-up MEMS [10]

switch [8] (figure1-1(e)), and laminate microphone [11] (figure 1-1(f)).

The laminate MEMS utilize many fabrication processes common to conventional microfabrication such as photolithography, wet etching, and deep reactive ion etching (DRIE). As a result, the laminate MEMS fabrication processes have similar limitations as the conventional MEMS fabricator processes, mainly high cost, long development time, and limited choice of fabrication materials.

1.2.3 Pop-up Book MEMS

Another method that has been reported to fabricate MEMS is pop-up book MEMS [9]. In this method, three-dimensional MEMS are fabricated by first, bulk micromachining rigid and flexible layers, then, laminating them, and finally folding the multi-layered rigid-flex laminate to build MEM systems. Figure 1-1(g) and (h) show reported mesoscale microstructures [9], and figure 1-1(i) shows fabricated millimeter-scale robots [10] using pop-up MEMS process. However, the pop-up book MEM systems are an order larger than the MEMS that can be fabricated using lithography-based microfabrication technology.

1.2.4 Limitations of Laser Micromachining

Although laser-micromachining has been around for many years, its application in fabricating MEMS has been limited [12][13][14][15] due to several reasons. First, manufacturing MEMS requires fabricating microstructures with small lateral feature-size (typically $10\mu m$) and large aspect ratio (typically 10:1 or higher). On the other hand, laser micromachining produces structures with larger lateral-features and low aspect ratio. As a result, the application of laser-micromachining has been largely limited to patterning surfaces [13] (figure 1-2(a)), drilling holes (figure 1-2(b)) [16][17], fabricating polymer micro-trenches (figure 1-2(c)) [18], and making millimeter-scale structures (figure 1-2(d), (e) & (f)) [19][18][13].

Second, the laser micromachined parts suffer from micro-burrs and debris around the machined parts. These imperfections are of the order of tens of microns, making these laser-

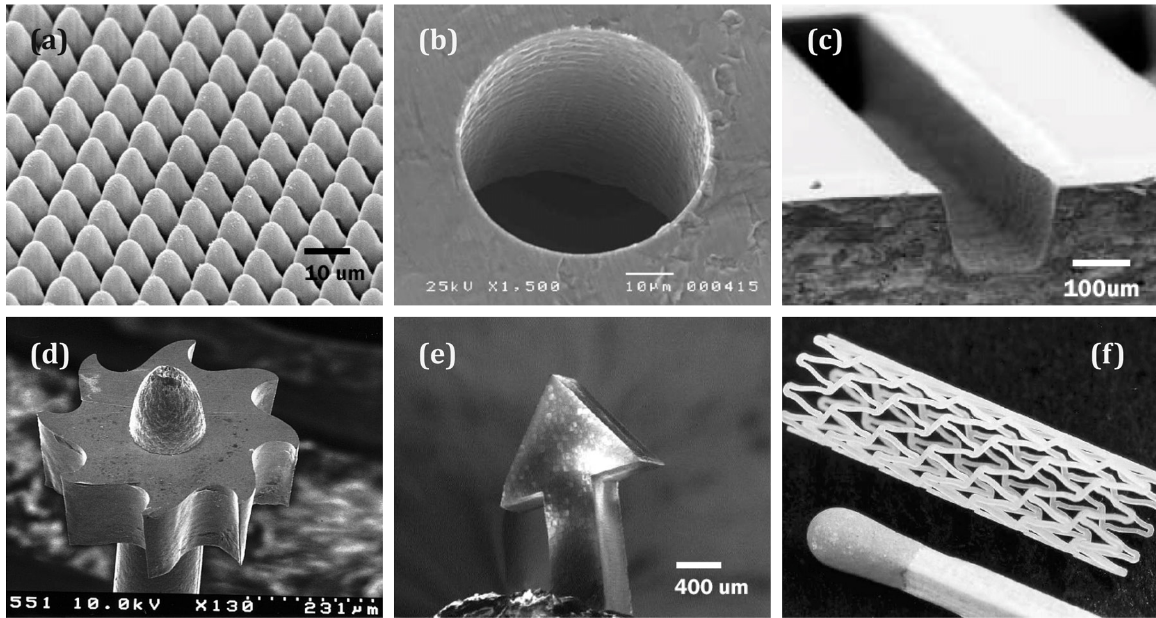

Figure 1-2: a) Surface patterning using an excimer laser [13]. (b) A 52μm diameter hole drilled through stainless steel using a copper vapor laser (CVL) [16][17]. (c) Micro-trench machined into PMMA using femtosecond laser [18]. (d) Nickel micro-turbine motor (outside diameter is 470μm and height is 150μm) fabricated using Laser-LIGA [19]. (e) Silicon wafer micromachined using nanosecond laser [13]. (f) A medical stent micromachined from a biodegradable polymer using a femtosecond laser [18].

micromachined parts unsuitable for MEMS fabrication. Eliminating these micro-burrs from delicate MEMS microstructure parts is challenging. Methods like sonication and physical scrub are not practical for MEMS structures due to their fragile nature. Similarly, etching process often results in dissolving the MEM structures along with the burrs because the size of the burrs is of the same order as the size of MEMS parts. Due to this reason, the laser-micromachining process has been largely used to fabricate rigid parts such as patterned surfaces, holes and trenches, where physical scrub or sonication can be utilized to remove burrs.

1.3 MALL

This thesis presents a novel approach to fabricate MEMS using multi-lamina assembly of laser-micromachined laminates (MALL). First, a novel microfabrication method called laser-assisted material phase-change and expulsion (LAMPE) micromachining is developed and used to manufacture small lateral-feature and high aspect ratio microstructure laminates. Second, these fabricated microstructure laminates are stack assembled to construct MEM systems. Figure 1-3 shows the schematic diagram of the MALL fabrication process.

1.3.1 LAMPE Micromachining

This thesis develops a novel approach to laser micromachine material sheets to create high aspect ratio structures significantly exceeding the optical penetration depth and thermal diffusion length of the material. The proposed approach utilizes laser-assisted material phase-change and expulsion (LAMPE) process to achieve the high aspect ratio while still maintaining the small lateral features. In this process, low energy laser power is used to first, induce a phase-change in the material, and then expel the altered material through the rear of the sheet utilizing pressure generated by vapor baubles formed at the laser-material interface due to the partial vaporization of material.

The proposed LAMPE micromachining can be used for a wide range of materials such

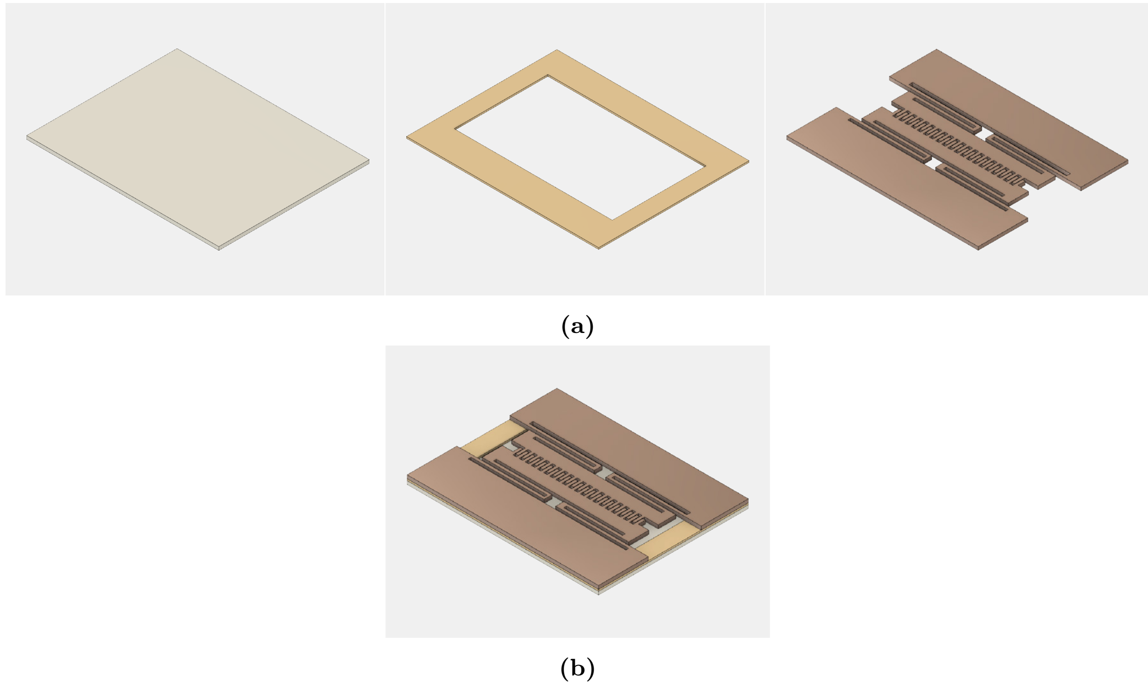

(a)

(b)

Figure 1-3: Schematic diagram of the MALL fabrication process. It consists of two steps: (a) fabricating the individual layer of MEM system using LAMPE micromachining, and (b) Multi-lamina assembly of LAMPE micromachined parts to fabricate MEM system.

as metals, silicon, and diamond. In LAMPE micromachining of metal sheets, first, the longitudinal profile of the laser beam is used to melt (i.e., induce phase-change) the material, and then, the liquid-phase metal is expelled through the rear of the sheet; as a result, creating features as small as the diffraction-limited spot size and as deep as the Rayleigh length of the focused beam. Such small features-size and high aspect ratio are not achievable using conventional laser micromachining utilizing vaporization to remove the material.

Similarly, in LAMPE micromachining of silicon, low energy laser pulses are used to oxidize the silicon (i.e. induce phase-change). The newly formed silicon oxide transmits the laser (due to its low absorption coefficient), causing further oxidation of silicon beneath it. As a result, enabling oxidation far beyond the optical penetration depth of silicon. The formed silicon oxide is granular and expelled through the rear of the wafer utilizing pressure generated by vapor baubles formed at the laser-material interface due to the partial vaporization of material.

Likewise, in LAMPE micromachining of diamond, first, the laser is used to convert the diamond into graphite (i.e. induce phase-change), and then the newly formed graphite is removed by oxidizing the graphite into carbon dioxide. Using LAMPE micromachining of diamond, a very high aspect ratio machining of diamond is reported.

Using the LAMPE micromachining process, lateral-features as small as $10\mu m$ and aspect ratio as large as 10:1 can be fabricated. These features are comparable to features produced using conventional lithography-based microfabrication processes such as deep reactive ion etching (DRIE). The LAMPE micromachining process is described in chapter 3.

1.3.2 Electro-deburring

For metals, the expelled liquid-metal resolidifies at the edges of the LAMPE micromachined part. These resolidified liquid-metal burrs are removed using an electro-deburring process developed in this thesis. The process utilizes high current density at sharp burrs and edges to selectively electrochemically etch burrs without significantly affecting the dimensions of the LAMPE micromachined part. It must be noted that for MEM systems that do not require high aspect ratio structures with small lateral features, traditional pulsed laser ablation (PLA) micromachining in conjunction with the electro-deburring process can be used for MALL MEMS fabrication. The electro-deburring process is described in section 3.5.

1.3.3 Multi-Lamina Assembly

The next step in the MALL process is to assemble the laser-micromachined layers. Mechanical alignment of laminates using dowel pins and alignment holes is widely used in precision macro-fabrication, and employed to align and bond microstructure laminates. Figure 1-4 shows the schematic diagram of the alignment-pin and alignment-hole assembly process. Using this method, alignment accuracy exceeding $2.5\mu m$ is demonstrated. The multi-lamina assembly process is described in section 4.1.

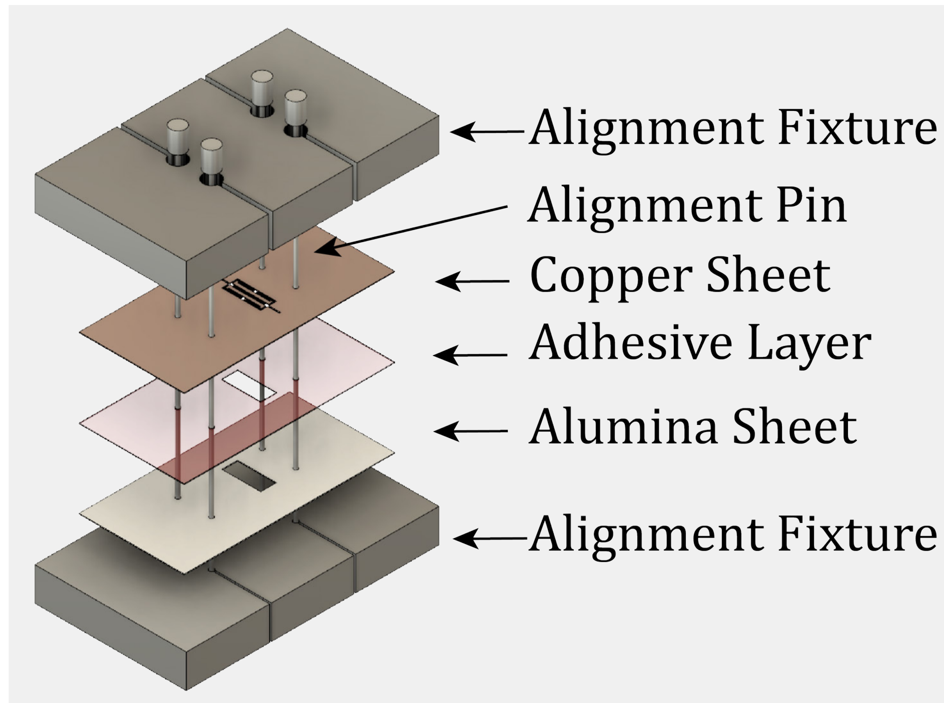

Figure 1-4: Schematic diagram of multi-lamina assembly.

1.4 Comparison with Prior Work

Table 1.1 provides a thorough comparison of MALL fabrication with other alternate MEMS fabrication processes. As can be seen, DRIE is desirable for small lateral features and high aspect ratio, however, falls short on the choice of fabrication material. After DRIE, the LIGA process is desirable for small lateral features and high aspect ratio, however, fall short on creating free-standing microstructures and require expensive x-ray source.

The MALL process presented in this thesis uses the similar lamination process that is used in PCB-MEMS, laminate MEMS, and Pop-up book MEMS. However, there are two major differences between the MALL process and other laminate PCB-MEMS, laminate MEMS, and pop-up book MEMS processes described in section 1.2. These differences are discussed in the following sections.

1.4.1 High Aspect Ratio & Small Lateral Feature

In the conventional MEMS fabrication process, deep reactive ion etching (DRIE) is used to fabricate structures with high aspect ratio and small lateral features. Typically, structures with the aspect ratio as large as 10:1 and lateral features as small as $5 - 10\mu m$ can be micromachined using DRIE [20]. The high aspect ratio machining is required to fabricate MEMS structures that can move in the direction parallel to the MEMS device plane such as interdigitated comb fingers and beam springs. These structures are common in many MEMS such as comb-drive actuators [21], accelerometers [22], resonators [23], and electromechanical filters [24].

In the PCB-MEMS, individual layers of the MEM system are fabricated using photolithography, followed by wet etching. However, the wet etching process is isotropic, thereby resulting in low aspect ratio. Similarly, in laminate MEMS, the individual layers are fabricated using various processes such as stamping, laser cutting, and electroforming [6]. These processes produce structures with larger features and limited aspect ratio than DRIE. Hence, the performance of these MEMS has been far from MEMS produced using conventional microfabrication process utilizing DRIE [4][25][26][27][11]. Moreover, the low aspect ratio structures have restricted movement in the direction of the device plane, and the motion is constrained to the direction normal to the device. As a result, the application of PCB-MEMS and laminate MEMS have been limited to MEM systems in which the structures move perpendicular to lamination plane, such as MEMS RF switch [4] and microphones [11].

In the MALL process, individual layers of the MEM systems are fabricated using LAMPE micromachining. The LAMPE micromachining process can fabricate microstructure laminates with aspect ratio as large as 10:1 and features as small as $10\mu m$. Such high aspect ratio while maintaining the small lateral features is not achievable in PCB-MEMS, laminate MEMS, and pop-up book MEMS fabrication processes. In fact, traditionally, such high aspect ratio and small lateral features were attainable exclusively using deep reactive ion etching (DRIE) [28]. The small features and large aspect ratio

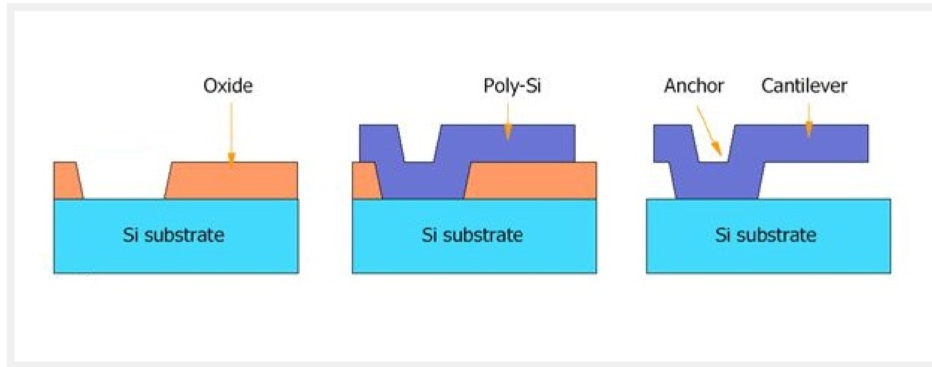

Figure 1-5: Schematic diagram of surface micromachining process. (a) First, a sacrificial layer is deposited and patterned. (b) Subsequently, structural layer is deposited on top of the sacrificial layer. (c) Finally, the sacrificial layer is removed to create free-standing microstructures.

structures fabricated using LAMPE micromachining are comparable to structures produced in DRIE. Hence, the MALL fabrication process can manufacture MEMS that are comparable to MEMS fabricated using DRIE.

1.4.2 Freestanding Structures with Six Degrees of Freedom

In conventional MEMS fabrication, surface micromachining [48][49][50] is used to fabricate free-standing microstructures. Figure 1-5 shows the schematic diagram of the surface micromachining process. First, a sacrificial layer is deposited on a substrate and patterned using photolithography and etching. Next, a structural layer is deposited and patterned on top of the sacrificial layer. Finally, the sacrificial layer is removed to create free-standing microstructures. The deposition process, such as chemical vapor deposition (CVD) used to deposit the sacrificial layer and structural layer, allows a high degree of control over the thickness of the deposited material and the gap created between structure and the substrate.

Fabricating similar thin freestanding structures in the lamination process is challenging. The difficulty is due to two reasons. First, as the thickness of the laminate is reduced, handling and micromachining these ultra-thin layers becomes difficult. Second, the freestanding structures are created using a spacer layer, which is patterned and sandwiched between the layer containing freestanding structure and the substrate. The

thickness of the spacer layer determines the gap between the freestanding structure and the substrate. As this gap and the size of freestanding structures is reduced, manipulating and patterning the ultra-thin spacer layer gets challenging. As a result, the applications of PCB-MEMS and laminate MEMS have been largely limited to either fabricating MEMS with no freestanding structures such as microfluidic devices [51][52] and optical MEMS [7] or MEMS with large gap between the freestanding structure and substrate such as such as MEMS microphone and electromagnetic switch [4][11][8][25][27].

The laser micromachining process used in MALL allows effortless patterning of B-staged epoxy adhesive layers. By using patterned adhesive layers as a spacer layer, tack bonding process, and high alignment accuracy, this thesis demonstrates fabricating freestanding structures with a gap between the structures as small as $12.5\mu m$ (as shown in figure 5-6). Similarly, by bonding ultra-thin film to rigid frame for manipulation and performing LAMPE micromachining, this thesis demonstrates fabricating freestanding structures as thin as $10\mu m$ (as shown in figure 5-5). These microstructures can be fabricated with small features and satisfactory aspect ratio to allow six degrees of freedom (DOF) movement.

Parameter	Material Choice	Minimum Lateral Features	Maximum Aspect Ratio	Minimum Layer Thickness	Minimum Gab Between Layers	Allow Sacrificial Layer?	Comments
DRIE	Silicon	$0.374\mu m$ [29], $10 - 15\mu m$ [30]	107:1 [29], $\sim 40:1$, [30]	$< 1\mu m$	$< 1\mu m$	Yes	High cost
PCB-MEMS / Laminate MEMS	Metals, FR4, polymers [32][33]	$10\mu m$ [34] , $25\mu m$ [35][36]	Quantitative data not available [6][37]	$\sim 50\mu m$[38]	$20 - 30\mu m$ [39], $87\mu m$ [40], $70\mu m$ [41]	Yes	Low aspect ratio due to isotropic wet etching of metals
Pop-up Book MEMS	Metals, FR4, and polymers	few microns [42], $\sim 20\mu m$ [43]	NA	NA	NA	NA	Produces Meso-scale MEMS
Direct-write Printing	Colloidal metal and ceramic particles	$20\mu m$ [44], $100\mu m$ [45], $5\mu m$ [46]	400 [46]	$20\mu m$ [44], $100\mu m$ [45], $5\mu m$ [46]	NA	NA	Very slow process [46]
LIGA	Metals that can be electroplated	$7\mu m$ [47]	50:1 [47]	$\sim 1\mu m$	NA	Yes	Require expensive x-ray source
MALL	Metals, Silicon, Diamond, and Polymers	$5 - 10\mu m$	10:1	$12.5\mu m$	$12.5\mu m$	Potentially yes but not demonstrated in this thesis	Rapid development, low-cost fabrication

Table 1.1: Comparison of various MEMS fabrication processes.

Chapter 2

Theory of Pulsed Laser Ablation

This chapter describes the theory of pulsed laser ablation (PLA) and its application in micromachining. The theoretical understanding of PLA is essential in estimating the limits on feature size and aspect ratio achievable in PLA micromachining, causes of these limitations, and potential solutions. Section 2.1 describes the analytical model of the pulsed laser ablation process and its application in laser micromachining. Section 2.2 characterizes the laser micromachining system used in this work.

2.1 Pulsed Laser Ablation

Figure 2-1 shows the schematic diagram of pulsed laser ablation process. When a laser beam hits a material target, it is absorbed by the free electron gas of the material through electromagnetic interaction, thereby increasing the temperature of the electron gas. Then, the energy of the electron gas is transferred to the lattice through the electron-phonon coupling, causing an increase in temperature of the material [53].

The duration between laser absorption and heating of the material is in the order of a few picoseconds. As a result, the electron-lattice interaction can be ignored for laser ablation utilizing long pulse duration in the order of nanoseconds, and the temperature distribution can be modeled using the classical heat diffusion equation. The absorbed laser heats the

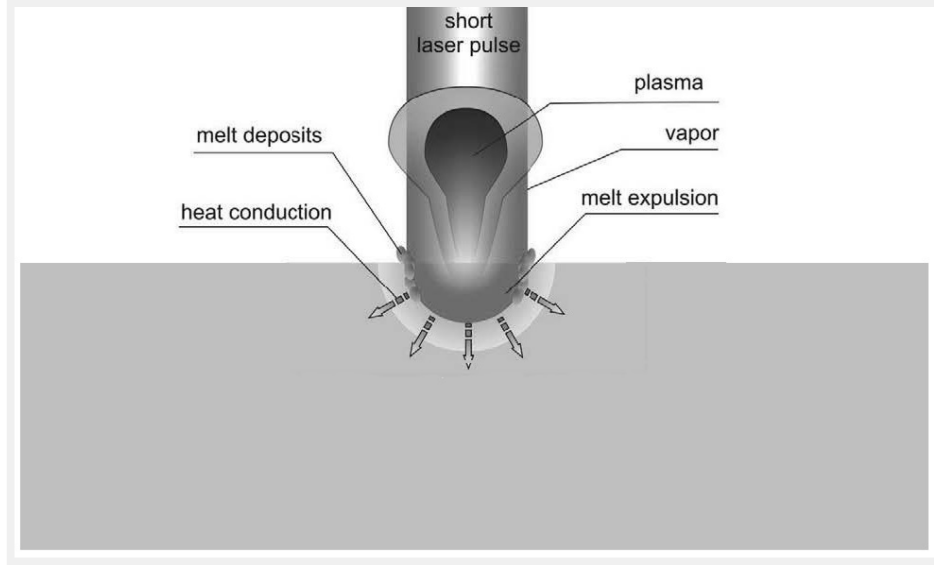

Figure 2-1: Schematic diagram of pulsed laser ablation (PLA) process. [54]

material and increases its temperature. When the temperature reaches the boiling point, the material vaporizes and gets removed from the target material.

The absorbed laser energy per unit volume and per unit time, Q is given by the expression [55]:

$$Q(x, y, z) = (1 - R)I(x, y, t)f(x) \tag{2.1}$$

where R is reflective of the material surface, $I(x, y, t)$ is the intensity of the laser beam, and $f(z)$ is the attenuation function due to laser beam absorption, given by the equation [55]:

$$f(z) = \alpha(T(z))exp\left[-\int_0^z \alpha(T(z'))dz'\right] \tag{2.2}$$

where $\alpha(T(z))$ is the temperature-dependent absorption coefficient. For pulsed ablation of metals studied in this work, it is assumed that the value of α is temperature independent. As a result, the above equation reduces to:

$$f(z) = \alpha e^{-\alpha z} \tag{2.3}$$

Substituting the expression for $f(z)$ in equation 2.1, we get the expression for the laser heat source as:

$$Q(x, y, z) = (1 - R)\alpha I(x, y, t)e^{-\alpha z} \tag{2.4}$$

Here, the characteristic length, known as optical penetration depth, l_α is defined as the distance at which the intensity is $1/e$ times the maximum intensity. Therefore,

$$l_\alpha = \frac{1}{\alpha} \tag{2.5}$$

Note that in the derivation of equation 2.4, it is assumed that the laser intensity is constant in the direction of propagation of the laser. This assumption is valid in situations where the optical penetration depth is smaller than the Rayleigh length of the laser beam. This assumption holds for the laser micromachining performed in this work.

The heat conduction in the material can be modeled using the heat diffusion equation [55]:

$$\rho c_p \frac{\partial T}{\partial t} = \rho c_p D \nabla^2 T + Q\delta(\vec{x}, t) \tag{2.6}$$

This heat conduction leads to an increase in temperature of the material. Once the temperature reaches boiling point, the material gets vaporized and removed from the target, resulting in micromachining. Next section describes the laser micromachining system used in this work.

2.2 Laser-Micromachining System

This work uses a commercially available laser micromachining system from Oxford Lasers Ltd [56]. The system consists of three major components: 1) Laser source, 2) Focusing optics, and 3) Motion system. These components are discussed in the following sections.

2.2.1 Laser Source

The laser source is an important component of a laser micromachining system and determines the feature size and type of materials that can be processed. There are two types of lasers that are employed in laser micromachining: pulsed laser and continuous-wave (cw) laser. The pulsed laser has two advantages over continuous-wave laser. First, the short laser pulse enables fine control over the energy dumped into the target, which is essential for machining small features. Second, the peak power of the individual pulse is several orders of magnitude higher than the average power of the laser. As a result, the pulsed laser can ablate the material even with much lower average power.

The laser source used in this work is a Q-switched frequency-doubled Nd:YAG diode-pumped solid-state (DPSS) laser. The wavelength of the laser is $532nm$ and the pulse duration is $20ns$. The mode of the laser beam is $TEM00$ and the beam quality $M^2 < 1.2$.

The average power, P_{avg} of the laser is between $2 - 6.5W$ and depends upon the pulse frequency. Figure 2-2 shows the variation of measured average power, P_{avg} with respect to the laser pulse frequency, F_p. The average power at $5KHz$ pulse repetition rate is $2.8W$.

The pulse energy E_p for individual pulses can be calculated by dividing the average measured power by pulse frequency, F_p.

$$E_p(J) = \frac{P_{avg}\ (W)}{F_p\ (Hz)} \tag{2.7}$$

Figure 2-3 shows the variation of pulse energy, E_p with respect to pulse frequency, F_p.The pulse energy at $5KHz$ pulse repetition rate is $561\mu J$.

The peak power (or pulse power) can be calculated by dividing the pulse energy with pulse duration ($20ns$ for the laser used).

$$Peak\ Power\ (W) = \frac{E_p\ (J)}{Pulse\ Duration\ (s)} \tag{2.8}$$

Figure 2-4 shows the variation of the peak power with respect to pulse frequency. It can be seen that the peak power is in the order of kilowatts even though the average power is

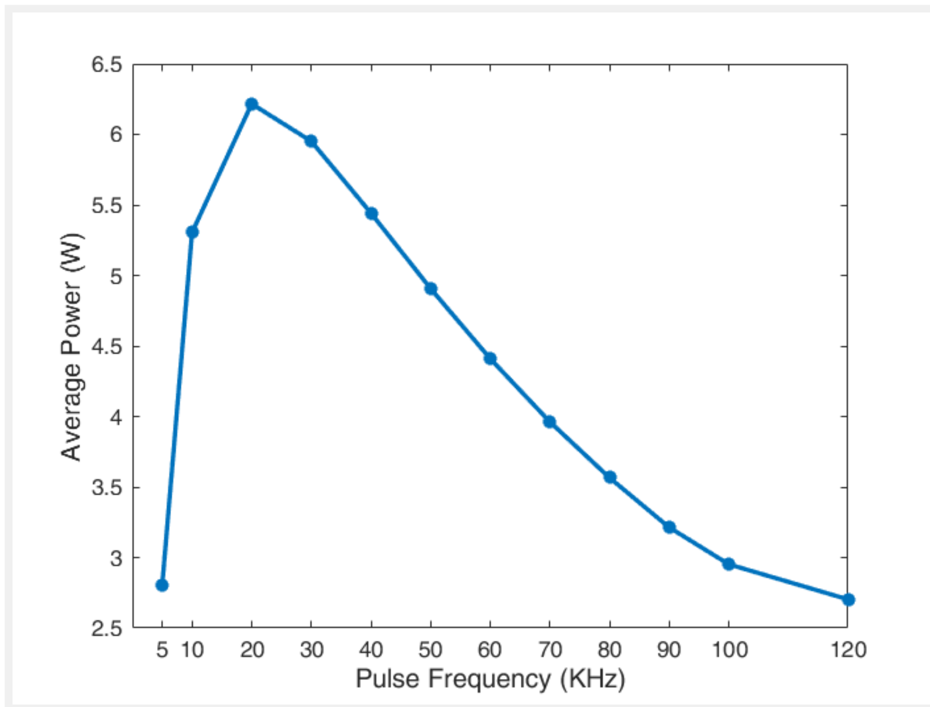

Figure 2-2: The plot of the average power , P_{avg} with respect to the pulse frequency

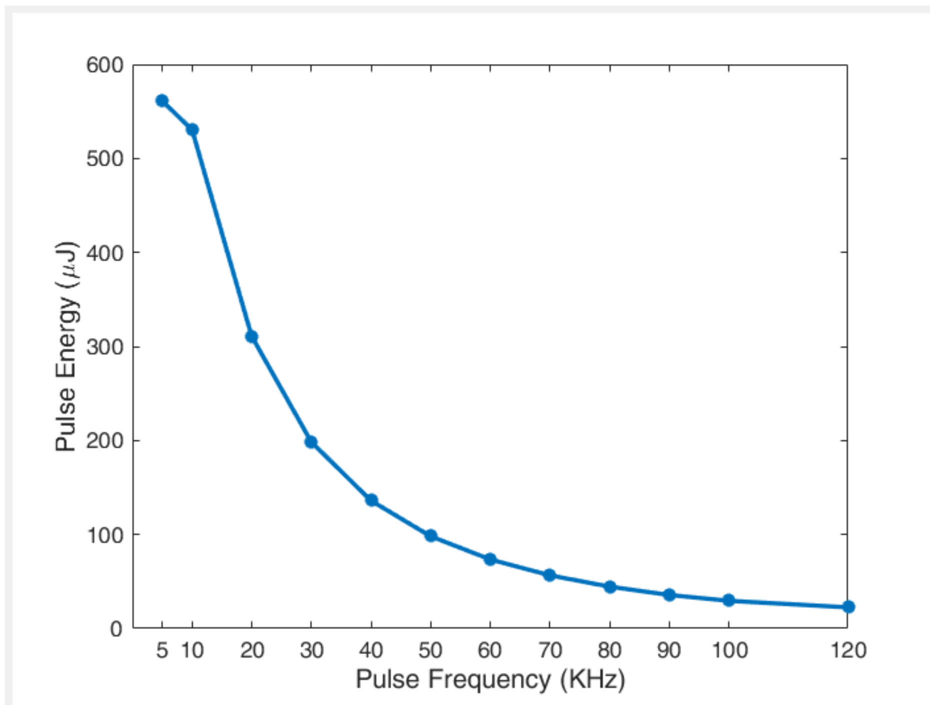

Figure 2-3: The plot of pulse energy, E_p with respect to the pulse frequency.

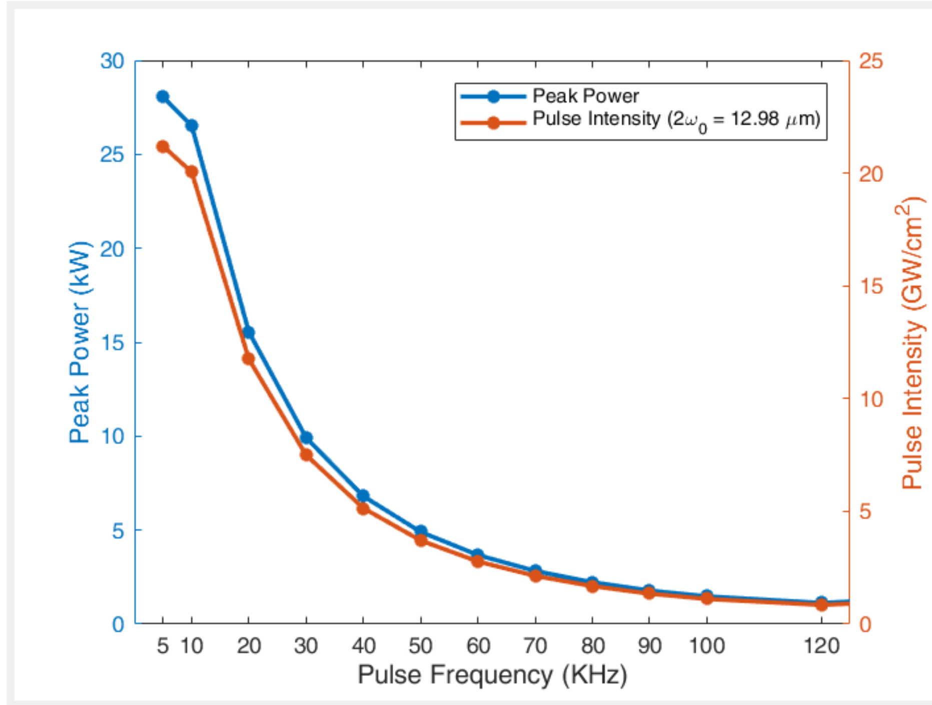

Figure 2-4: The plot of peak power (left) and pulse intensity (right)with respect to the pulse frequency.

less than $6.5W$. The peak power of the laser pulses is responsible for the ablation of the material. The peak power at $5KHz$ pulse repetition rate is $28kW$. Table 2.1 summarizes the values of the parameters calculated for the laser used in this work.

Laser Parameter	**Value**
Wavelength, λ	$532nm$
Average Power, P_{avg}	$2.8W$
Pulse Frequency, F_p	$5KHz$
Pulse Duration, τ_l	$\approx 20ns$
Pulse Energy, E_p	$561\mu J$
Peak Power, P_{pk}	$28kW$

Table 2.1: The values of various parameters of laser source.

2.2.2 Beam Delivery & Focusing Optics

The laser beam is delivered to the target material using a series of mirrors, lenses, and other optical elements. First, the laser beam emitted from the source is expanded using a beam expander. The diameter of the laser beam after the beam expansion is $10mm$. The beam is then allowed to pass through a variable attenuator, which is used to attenuate the laser beam and control the energy dumped into the target. Finally, the laser beam is focused onto the target using either a lens or a microscope objective.

Diameter of Focused Beam

For a TEM_{00} mode laser focused using a thin lens, the intensity profile at the focal plane has a Gaussian distribution and given by the equation [55]:

$$I(r) = I_0 exp\left(-\frac{2r^2}{\omega_0^2} \right) \tag{2.9}$$

where ω_0 is the beam spot radius, defined as the distance at which the intensity $I(\omega_0) = I_0/e^2 = 0.135 I_0$ (2.2.2). The Gaussian intensity distribution has no obvious boundaries to give it a characteristic dimension. However, the distance between the points where the intensity has fallen to $1/e^2 = 0.135$ of the maximum value is generally considered as the diameter of the focused beam and contains 86% of the total power of the laser beam [57].

The value of the diameter of beam spot size, $2\omega_0$ is given by the equation [57]:

$$2\omega_0 \; (Beam\ Spot\ Diameter) = 2.44\frac{f\lambda}{d} \tag{2.10}$$

where λ is the wavelength of laser beam, d is the beam waist, and f is the focal length of the lens.

For the laser used in this work, the wavelength $\lambda = 532nm$, beam waist (or aperture diameter) $d = 10mm$, and focal length $f = 100mm$. The calculated focused spot size $2\omega_0 = 12.98\mu m$. The focused beam spot size $2\omega_0$ is an important parameter in determining the minimum achievable feature size in laser-micromachining.

In addition to lens, microscope objectives can also be used for focusing the beam. Generally, an infinity-corrected objective is desirable as it enables simultaneous laser micromachining and imaging, and easy insertion of additional optical components. In an infinity-corrected objective, the light effectively travels parallel to the optical axis. As a result, additional optical components such as optical filters, polarizer and beamsplitters can be inserted between the tube lens. To create an image with an infinity-corrected objective, a tube lens must be used to focus the image.

The diffraction-limited spot size of a laser beam focused using a microscope objective is given by the equation:

$$2\omega_0 = \frac{1.22 * \lambda}{NA} \tag{2.11}$$

where λ = wavelength of light and NA is the numerical aperture.

Intensity of Focused Beam

The average pulse intensity of the focused laser beam is given by the expression:

$$Average\ Pulse\ Intensity, I_p\ (\frac{W}{cm^2}) = \frac{Peak\ Power\ (W)}{Focused\ Beam\ Spot\ Size\ (cm^2)} \tag{2.12}$$

The peak power of the laser pulse at $5KHz$ is $28W$ and the diameter of the focused beam spot is $\omega = 12.98\mu m$; therefore, the pulse intensity is $21.2GW/cm^2$. The right y-axis of figure 2-4 shows the variation of pulse intensity I_p with respect to the pulse frequency.

The total power of the laser beam is given by the equation [55][58][59]:

$$P = 2\pi \int_0^\infty rI(r)dr = \frac{\pi\omega_0^2 I_0}{2} \tag{2.13}$$

$$\implies I_0 = \frac{2P}{\pi\omega_0^2} \tag{2.14}$$

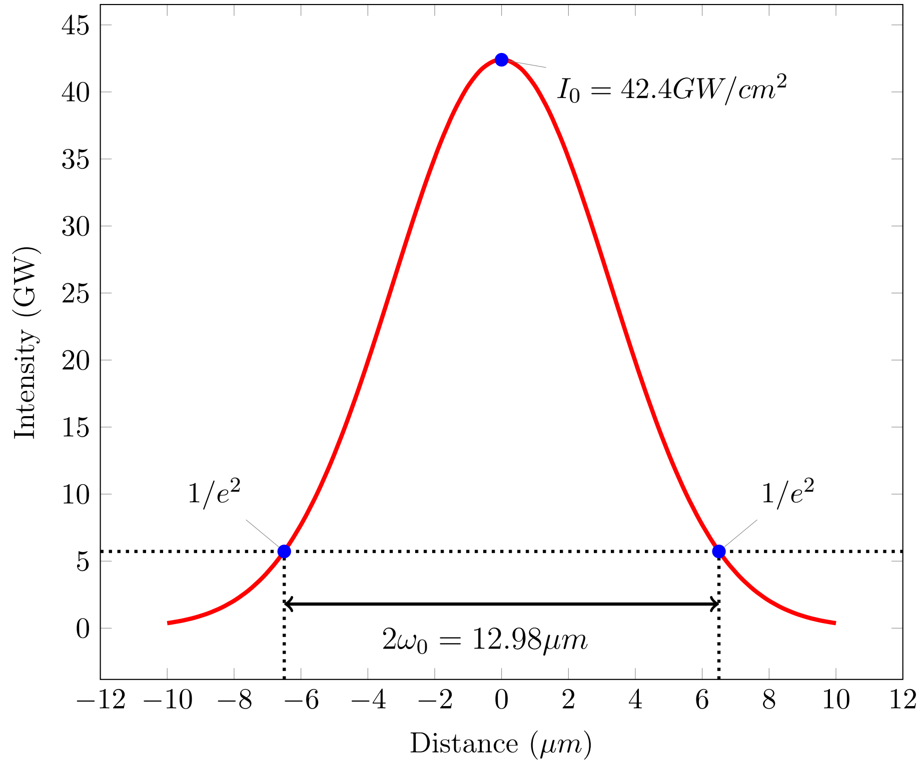

Figure 2-5: Intensity profile of focused laser beam. The beam spot diameter is $I_0 = 21.2MW/cm^2$ and the maximum intensity $I_0 = 21.2MW/cm^2$.

As can be seen, the intensity of the central peak of a Gaussian beam is twice the average intensity of the laser pulse. The peak power of the laser at $5KHz$ pulse frequency is $P = 28KW$ (Table 2.1). Substituting this value in equation 2.14 along with $2\omega_0 = 12.98\mu m$ (2.2.2), we get $I_0 = 2I_p = 42.4GW/cm^2$. Figure 2-5 shows the intensity profile of the laser beam.

Rayleigh length

The radius of the laser beam at a distance z from the focal plane is given by the equation:

$$\omega(z) = \omega_0 \sqrt{1 + \left(\frac{z}{z_R}\right)^2} \tag{2.15}$$

where z_R is the Rayleigh length and defined as the distance at which the radius of the beam

is $\omega_0\sqrt{2}$, and given by the expression:

$$z_R = \frac{\pi\omega_0^2}{\lambda} \tag{2.16}$$

For the laser used in this work, the Rayleigh length, $Z_R = 850\mu m$. The region $|z| \leq z_R$ is known as the Rayleigh range.

2.2.3 Motion System

A 2-axis stage is used to move the target with respect to the laser to perform laser micromachining. For each axis, the resolution is $0.250\mu m$, repeatability is $0.750\mu m$, and accuracy is $+/-2\mu m$. The maximum attainable speed is $250mm/s$, and the maximum attainable acceleration/deceleration is $10,000mm/sec^2$. It must be noted that the practical limit on maximum attainable speed for micromachining MEMS parts is restricted to $1mm/s$ or less due to their small size and limited acceleration/deceleration of the stage.

The feature size in laser micromachining process depends upon the laser energy dumped into the target. This dumped energy is controlled by changing the pulse energy and the overlap between the successive laser pulse exposure. For the system used in this work, the focused beam spot size is $12\mu m$, and the minimum pulse repetition rate is $5KHz$, as a result, the target is set to $1mm/s$ speed to ensure a pulse overlap of 20%. However, it must be noted that due to the small size of the MEM systems and limitation on the maximum attainable acceleration, the actual speed while machining sub-millimeter part is less than $1mm/sec$, resulting in more energy dumped into the target than desired.

Using a galvanometer scanner is desirable instead of using a 2-axis stage. The galvanometer can provide much higher feed rate, thereby enabling fabricating small features by allowing fine control over the energy dumped into the target. Moreover, the high feed rate can increase the micromachining rate. A typical 2-axis galvanometer mirror can operate at $100Hz$ frequency [60]. Assuming, the scan distance of $1mm$, a feed rate of $100mm/s$ can be easily achieved.

2.3 Summary

In summary, this chapter lays the foundation for the theory of laser micromachining, which is used in next chapter to estimate the theoretical limit on the feature size of LAMPE micromachining process. The value of laser parameters such as focused beam spot size, pulse energy, and peak power determines the mode of laser micromachining, and must be determined. The laser pulse energy above a threshold value results in pulsed laser ablation, while the pulse energy below this threshold results in LAMPE micromachining. The threshold value depends upon the material property, beam spot size, and laser pulse duration. This chapter describes the experimental procedure and calculations used to measure and derive these laser parameters for the system used in this thesis. This parameters are summarized in table 2.1.

Chapter 3

Laser-assisted Material Phase-change & Expulsion

3.1 Introduction

One motivation of this thesis is to expand the material library for fabricating MEMS, especially enabling fabrication using metals because they offer a wide range of mechanical and electrical properties. Moreover, these properties can be tuned by the alloying process. The ability to fabricate MEM systems using metals will empower new paradigms in MEMS design. Moreover, the metal foils used for MEMS fabrication are low-cost and easy to fabricate using roll forming process [61]. Unfortunately, the existing wet and dry etching processes are isotropic and not suitable for fabricating high aspect ratio microstructures required for making MEMS.

At a macro-scale, lasers are widely used for cutting metal sheets. In this process, laser is used to melt the metal, and a high-pressure air jet is used to expel the melted material. However, high-pressure jets cannot be employed at a micro-scale due to the delicate nature of the laser micromachined structures. Due to this reason, laser micromachining utilizes vaporization to remove the material. However, the vaporization process results in low aspect ratio micromachining.

The low aspect ratio in pulsed laser ablation micromachining utilizing vaporization is due to several reasons. First, during the ablation process, the vaporized material creates a plasma above the ablated region (figure 2-1). This plasma absorbs the laser, thereby reducing the energy available for ablation. As the depth of ablation crater increases, the laser absorption by plasma becomes significant, and laser energy available to the target is no longer sufficient to process the material. This phenomenon limits the maximum depth of micromachining achievable using the PLA laser-micromachining process.

Second, the aspect ratio depends upon the optical penetration depth of the material. For metals, the absorption coefficient $\alpha > 10^5 cm^{-1}$ [55], and the optical penetration depth, $1/\alpha$ is in the order of a few nanometer. Therefore, the laser energy is confined to a very thin layer on the surface, and the laser acts as a surface heat source. Due to isotropic heat conduction, the surface heating of the metal results in an equal temperature gradient in all directions, thereby resulting in approximately 1:1 aspect ratio of ablation profile. However, it must be noted that for laser with Gaussian intensity distribution, the depth of the ablation profile is larger than the width due to high intensity at the center of the Gaussian beam.

Third, the material vaporization also results in large melt-pool around the ablated region (figure 2-1). This melted material is shifted by the high pressure escaping vapors, thereby increasing the width of the ablation region.

This thesis presents a novel approach to laser micromachine material sheets to create high aspect ratio structures significantly exceeding the optical penetration depth and thermal diffusion length of the material. In the proposed approach, instead of using the vaporization to remove the material, the metal is melted, and the liquid-metal is expelled through the rear of the sheet utilizing pressure generated by vapor baubles formed at the laser-material interface due to the partial vaporization of the material. The expelled material resolidifies at the periphery of the micromachined part. This resolidified material is removed using the developed electro-deburring process. The proposed approach, referred to as laser-assisted material phase-change and expulsion micromachining or LAMPE micromachining can be used to fabricate high aspect ratio structures with small lateral features.

3.2 LAMPE

Figure 3-1 shows the schematic diagram of the LAMPE micromachining process. This process is similar to laser cutting of thick sheets of metals. In the laser cutting of metals, the laser is used to melt the metal (not vaporize) and a high-pressure air jet is used to expel the melted material. However, in the LAMPE micromachining process, the metal is ejected by the pressure generated from the vapor bubbles formed at the laser-metal junction.

A careful setting of laser power is required to achieve laser-assisted material-phase change and expulsion process. The laser power below it would not result in partial vaporization of the material, and no expulsion will occur. The laser power above it will result in the creation of large melt-pool and complete vaporization, thereby increasing the feature size. The value of laser power required for LAMPE micromachining can be estimated using Eq. (3.6). It is empirically shown that the LAMPE micromachining process can result in lateral feature size as small as the diffraction-limited spot size of the beam and the aspect ratio as long as the Rayleigh length. It must be noted that the LAMPE micromachining process is limited to fabricating high aspect ratio structure only in sheets.

The LAMPE micromachining process has several advantages over laser ablation micromachining. First, the laser power required for LAMPE micromachining is significantly lower than the power required for laser micromachining using vaporization. The low power requirement is because the enthalpy of melting is less than the enthalpy of vaporization. Moreover, the absence of vapor plasma (figure 3-1) results in no laser absorption and the entire laser power is available for material processing. Second, the thermal and mechanical shock exerted on the material during melting is less the thermal and mechanical shock exerted on the material during vaporization. As a result, the heat-affected zone (HAZ) in LAMPE micromachining is smaller than HAZ resulting in vaporization.

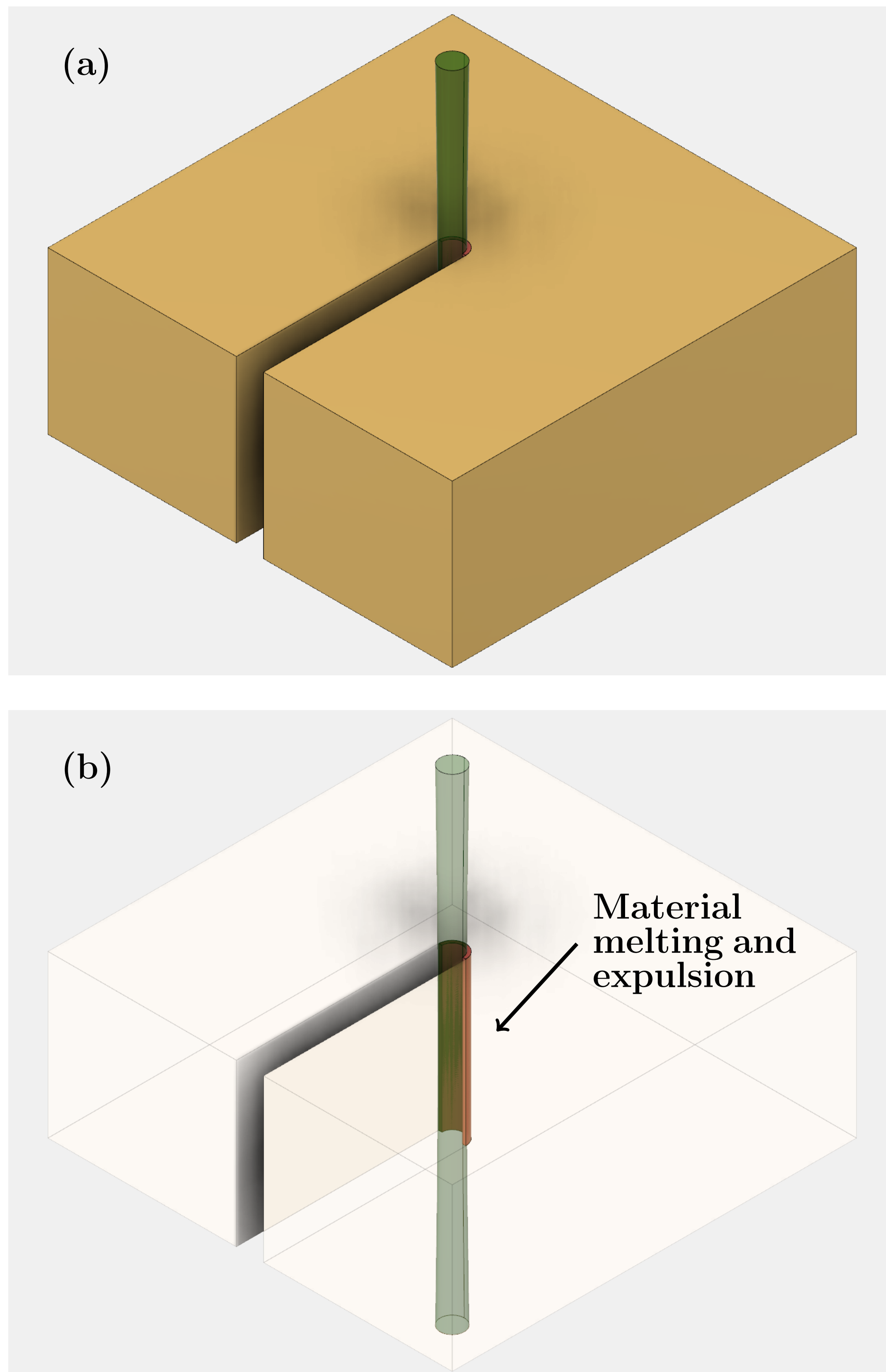

Figure 3-1: (a) Schematic diagram of LAMPE micromachining process illustrating fabrication of high aspect ratio structures. (b) Image highlighting the melt region of the sheet. The melted material is expelled downwards.

3.2.1 Difference between PLA and LAMPE Micromachining

The differences between conventional laser micromachining utilizing pulsed laser ablation and LAMPE micromachining process are as follows:

1. In conventional pulsed laser ablation (PLA) micromachining, the material is removed using vaporization, and the mass of the target is reduced after laser micromachining process. However, in the LAMPE micromachining process, the metal is melted, and the liquid-metal is expelled through the rear of the sheet using the pressure generated by vapor baubles formed at the laser-material interface. This expelled liquid-metal resolidifies at the edges of the micromachined part. Thus, the mass of the target remains unchanged. In LAMPE micromachining, the material is removed using the electro-deburring process.

2. The laser fluence required in PLA micromachining is higher than the laser fluence required in LAMPE micromachining process because the enthalpy of vaporization is higher than the enthalpy of melting. The low fluence requirement for LAMPE micromachining considerably reduces the cost of a laser source.

3. The conventional PLA laser micromachining process can be used to fabricate 2.5D structures by raster scanning overlapping pulse irradiation spots [62][63]. However, the LAMPE micromachining process is limited to micromachining material sheets.

4. The PLA micromachining produces lateral features larger than diffraction-limited spot size because of the formation of large melt-pool around the ablation region. However, as shown in section 3.4, the LAMPE micromachining can produce lateral features as small as the diffraction-limited spot size. Figure 3-2 shows the lateral feature size created using PLA and LAMPE micromachining process. As can be seen, the minimum feature size produced in PLA micromachining is $28\mu m$ and in LAMPE micromachining is $8\mu m$.

5. In the conventional laser micromachining, the vaporized material creates a plasma

above the ablation region. This plasma absorbs the laser beam, thereby reducing the energy available for vaporization and limits the achievable depth of micromachining. In contrast, no vapor plasma is formed in LAMPE micromachining, and the aspect ratio is only limited by the Rayleigh length of the laser beam.

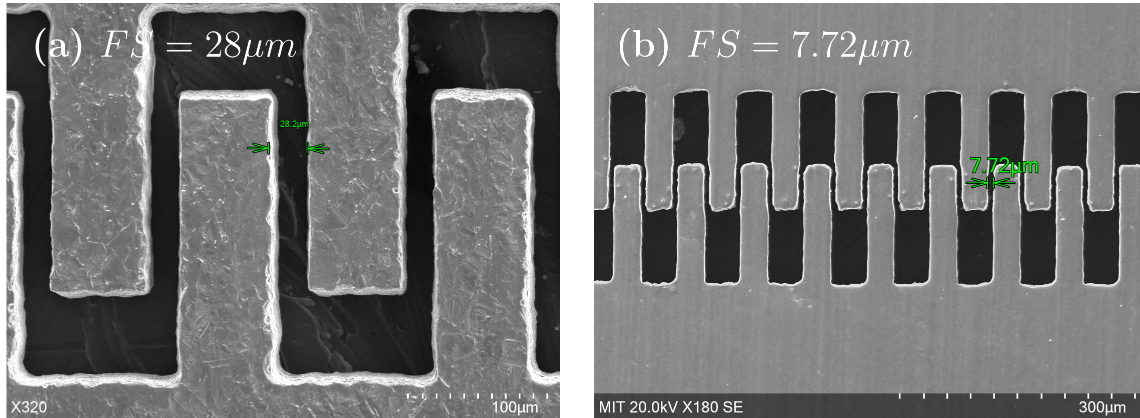

Figure 3-2: Comparison of lateral feature size (FS) produced in PLA and LAMPE micromachining. Note that these parts are cleaned using the electro-deburring process, which is discussed in section 3.5. (a) Lateral features produced in pulsed laser ablation (PLA) micromachining. (b) Lateral features produced in LAMPE micromachining.

3.3 Feature Size in LAMPE Micromachining

The minimum achievable feature size depends upon the focused beam spot size and laser pulse duration. In a conventional pulsed ablation process, the material is removed through vaporization, resulting in large melt-pool, plasma plum, and thermal shock on the material lattice. As a result, the minimum feature size is much larger than the theoretical limit [64][65][66][62]. However, using the laser-assisted material phase-change and expulsion (LAMPE) micromachining, feature size comparable to the theoretical limit can be achieved. Moreover, using LAMPE micromachining, much higher aspect ratio can be achieved than previously possible.

Laser Parameter	**Value**
Wavelength, λ	$532nm$
Average Power, P_{avg}	$28mW$
Pulse Frequency, F_p	$5KHz$
Pulse Duration, τ_l	$\approx 20ns$
Reflectivity of Copper, R	0.43
Pulse Energy, E_p	$3.2\mu J$
Peak Power, P_{pk}	$280W$
Beam Spot size, $2\omega_0$	$1\mu m$
Rayleigh Length, Z_R	$1.5\mu m$
Maximum Intensity, I_0 of Focused Beam	$71.5GW/cm^2$

Table 3.1: Laser parameters for LAMPE micromachining.

3.3.1 Experiment & Results

Figure 3-3 shows the minimum achievable feature size of $5\mu m$ using LAMPE micromachining process. This feature is created by irradiating a single pulse of laser with wavelength $532nm$ and pulse duration $20ns$ on a copper target. The pulse energy is $5.6\mu J$, which is set by reducing the original pulse energy of $561\mu J$ to its 1 % value using an external attenuator. The reflectivity of the copper target, $R = 0.47$; therefore, the effective energy available for material processing is $3.2\mu J$. The laser beam is focused using a microscope objective with numerical aperture $NA = 0.65$. The focused beam spot diameter is $1\mu m$, giving the maximum intensity at the center of Gaussian distribution as $I_0 = 71.5GW/cm^2$. Table 3.1 summarizes the laser conditions used for LAMPE micromachining process.

The small feature size is possible in the LAMPE micromachining because the laser is used to melt and expel the material, thereby eliminating the drawbacks of vaporization present in the pulsed ablation process. The expelled liquid metal resolidifies at the rim of the hole and can be removed using an electro-deburring process developed in this work (section 3.5). Figure 3-4 shows the LAMPE fabricated hole before and after removing the resolidified metal.

The next section describes the analytical model for the LAMPE micromachining process. This model is similar to the pulse ablation model described in reference [55], with

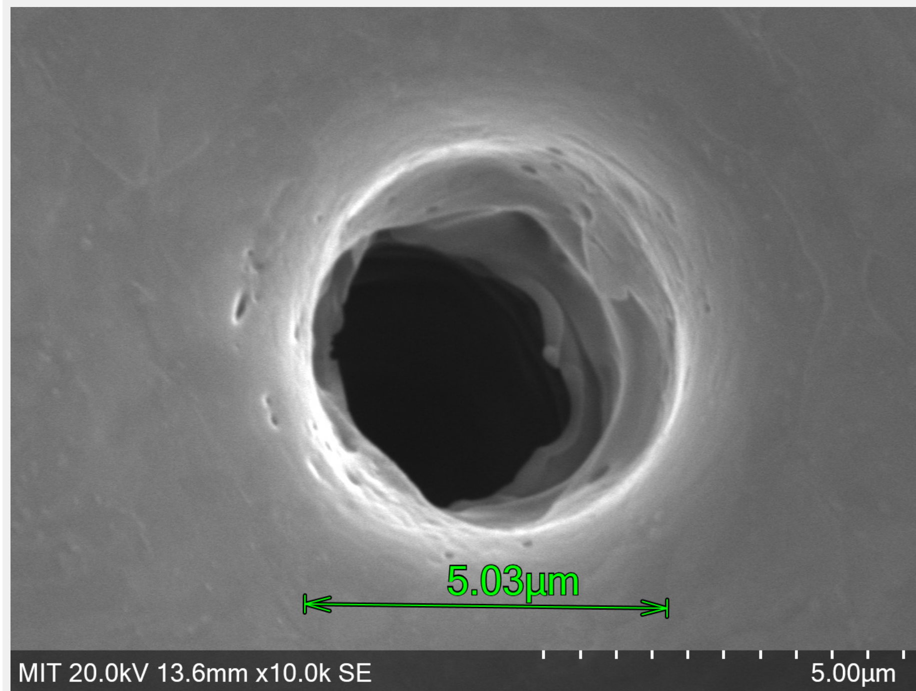

Figure 3-3: A crater fabricated using LAMPE micromachining to demonstrate the minimum achievable feature size. The diameter of the hole is $5\mu m$.

two major distinctions. First, the enthalpy of melting is used instead of enthalpy of vaporization. Second, as there is no vaporization, the model excludes plasma formation, laser absorption due to plasma, expansion of liquid and vapor, and hydrodynamic expulsion of melted material.

3.3.2 Analytical Model

This section describes the theoretical model to estimate the minimum achievable feature size in LAMPE micromachining and compares it with experiment results. As discussed earlier, the LAMPE micromachining is performed on a copper target using a single pulse of laser with pulse duration 20 nanosecond and wavelength $532nm$.

The optical penetration of the laser beam inside material is given by the Beer-Lambert law (eq: 3.1). Here, we can define a characteristic length, the optical penetration depth

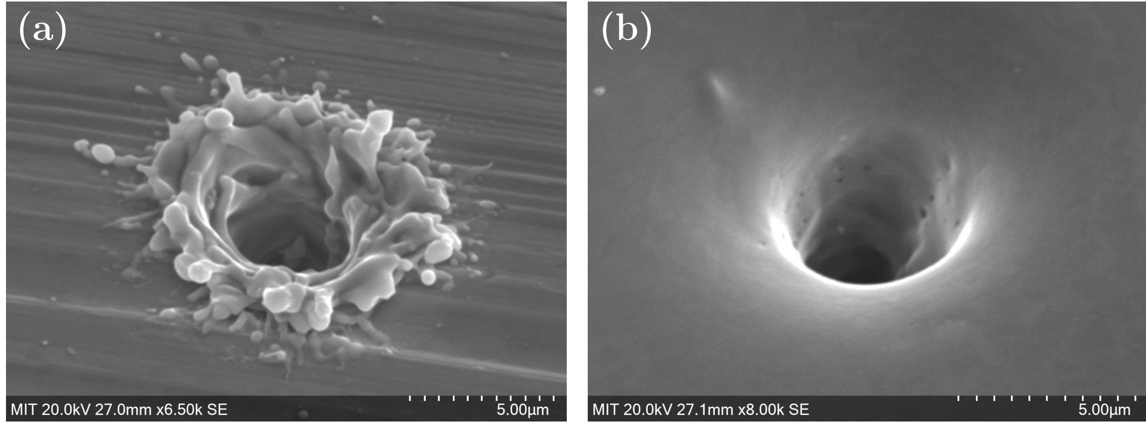

Figure 3-4: Electro-deburring of LAMPE micromachined crater. (a) Before electro-deburring. (b) After electro-deburring.

$l_\alpha = 1/\alpha$, which is a measure of how deep the laser penetrates inside the material.

$$I(z) = I_0 e^{-\alpha z} \tag{3.1}$$

where I_0 is the laser intensity at the surface, and α is the absorption coefficient of the material.

For copper, the absorption coefficient at $532nm$ is $\alpha_{Cu} = 7.14 \times 10^5 cm^{-1}$ [55], and the optical penetration depth is $14nm$. As a result, the laser is absorbed only at the surface and acts as a surface heat source. The absorbed heat further propagates to the bulk of the material through thermal conduction and can be modeled using the heat diffusion equation:

$$\rho c_p \frac{\partial T}{\partial t} + \rho c_p D \nabla^2 T = 0 \tag{3.2}$$

where ρ is the mass density of the material, c_p is the heat capacity of the material, T is the temperature, and D is the thermal diffusivity of the material.

For the experiment described in section 3.3, the diameter of the focused spot, $\omega_0 = 1\mu m$ and the optical penetration depth $l_\alpha = 14nm$ is much smaller than the dimensions of the target (for the copper target, $length, a = 10mm$, $width, b = 10mm$, and $thickness, t = 100\mu m$) i.e.

$$\omega_0, l_\alpha \ll a, b, t$$

As a result, the laser surface source can be modeled as a *point source in space* and the fundamental solution of (3.2), describing the evolution of temperature distribution with time, is given by expression [55]:

$$T(\vec{x}, t) \approx \frac{Q}{\rho c_p (4\pi D t)^{\frac{3}{2}}} exp\left(- \frac{|\vec{x}|^2}{4Dt} \right) \tag{3.3}$$

The solution above depicts 1/e decay of the temperature in space. For laser irradiation with pulse duration τ_l, we can define a thermal diffusivity length l_T, at which the temperature reaches 1/e times the maximum value. Therefore, at $|\vec{x}| = l_T$

$$-\frac{l_T^2}{4D\tau_l} = 1 \tag{3.4}$$

which gives the expression for thermal diffusion length as:

$$l_T = 2\sqrt{D\tau_l} \tag{3.5}$$

The thermal diffusion length is a measure of minimum feature size achievable using the LAMPE process. The thermal diffusivity D for copper is $1.14 cm^2/s$. When the copper target is processed with a single laser pulse of duration $\tau_l = 20ns$, the thermal diffusivity length is $3.02\mu m$. Since the heat dissipates isotropically in all directions, the achievable feature size is $2 \times l_T + Beam\ Diameter = 7\mu m$. As shown in 3-3, the feature size is less than the theoretical value. This discrepancy could be due to ignoring the Gaussian intensity distribution of the focused laser beam.

It must be noted that the expression for thermal diffusion length l_T given by (3.5) is applicable only for a point source in space. For all other cases, the thermal diffusion length l'_T, defined as $l'_T = T(0)(1/e)$, depends upon the particular boundary conditions of the problem and may differ significantly from equation (3.5).

Threshold Fluence for LAMPE

The threshold fluence can be estimated by calculating the energy required to melt the volume of the material covered by the thermal diffusion length. This volume, V_{l_T} can be approximated as a hemisphere of radius l_T. If we ignore the heat loss due to surface reflection, convention, radiation, and hydrodynamic material expulsion, the threshold pulse energy is given by the expression:

$$E_{th_m} = \rho V_{l_T} c_p (T_m - T_{amb}) + \rho V_{l_T} \Delta H_m \tag{3.6}$$

where ρ is mass density, V_{l_T} is LAMPE micromachined volume, c_p is specific heat capacity, T_m is melting temperature, T_{amb} is ambient temperature, and ΔH_m is latent heat of fusion (melting).

For copper, $\rho = 8.94 g/cm^3$, $c_p = 0.47 J/gK$ at $1000K$, $T_m = 1357K$, and $\Delta H_m = 200J/g$. The ambient temperature is set to $T_{amb} = 298K$ and the volume $V_{l_T} = 5.76 \times 10^{-11} cm^3$. Substituting these values in equation 3.6, we get:

$$E_{th_m} = 0.36 \mu J \tag{3.7}$$

The laser beam is focused using a microscope objective with numerical aperture $NA = 0.65$ giving the focused beam spot diameter of $1 \mu m$. By diving the pulse energy E_{th_m} by beam spot area, we get the threshold fluence $F_{th_m} = 4.6 \mu J/\mu m^2$. For comparison, an approximate estimation of pulse energy required for vaporization can be calculated by substituting ΔH_m with $\Delta H_v = 4700 J/g$, which gives $E_{th_v} = 3.04 \mu J$. Note that the actual pulse energy required for vaporization is much higher than this estimate due to the absorption of the laser by plasma plume [55].

The pulse energy for LAMPE micromachining, E_{LAMPE} is greater than E_{th_m} and less than E_{th_v}, but closer to E_{th_v}. The exact value can be determined empirically by performing a series of experiments of varying pulse energy between E_{th_m} and E_{th_v}. As described in section 3.3 for LAMPE micromachining, the pulse energy $E_p = 3.2 \mu J$ is selected such

that it is greater than $E_{th_m} = 0.36\mu J$ to ensure melting of the metal, and comparable to $E_{th_v} = 3.04\mu J$ to ensure partial vaporization to generate recoil force to expel the melted material. It must be noted that the actual value E_{th_v} is higher than $3.04\mu J$ because of heat loss due to convection, radiation, laser absorption by plasma, hydrodynamic material expulsion.

When processing new materials, I suggest using the calculations shown above to estimate the required pulse energy E_{LAMPE} and fluence F_{LAMPE} for LAMPE micromachining and use that as a starting point for further process development.

It must be noted that the material is largely melted (and only partially vaporized). This hypothesis can be validated empirically by performing a series of dot array machining with varying pitch distance. Figure 3-5 shows the micromachined dot array at pitch distance of $20\mu m$, $10\mu m$, and $5\mu m$. In figure 3-5(a), the machined dots are far apart, and the melted metal is forced to expel upward, creating a crater. As the dot patterns overlap, the pulsed laser ablation process involving vaporization to remove material results in a recess or $2.5D$ micromachining [63]. However, the LAMPE micromachining process results in resolidified slag as shown in figure 3-5(c). The slag is formed due to the mere shifting of the melted material and resolidification when dots overlap. These findings confirm that in the LAMPE micromachining process, there is minimal vaporization, and the micromachining process is dominated by liquid-metal expulsion.

3.3.3 Numerical Simulation

This section describes finite elements analysis (FEA) of LAMPE micromachining to estimate the minimum achievable feature size and compares it with the analytical model (section 3.3.2) and experiment results (section 3.3.1).

For finite element analysis, COMSOL multiphysics software is used [67]. The three-dimensional heat diffusion equation is solved to determine the temperature distribution in the material. Since the optical penetration depth of the laser is small ($14nm$), the source term Q of the heat diffusion equation is set to $Q = 0$, and the laser heating is modeled as a

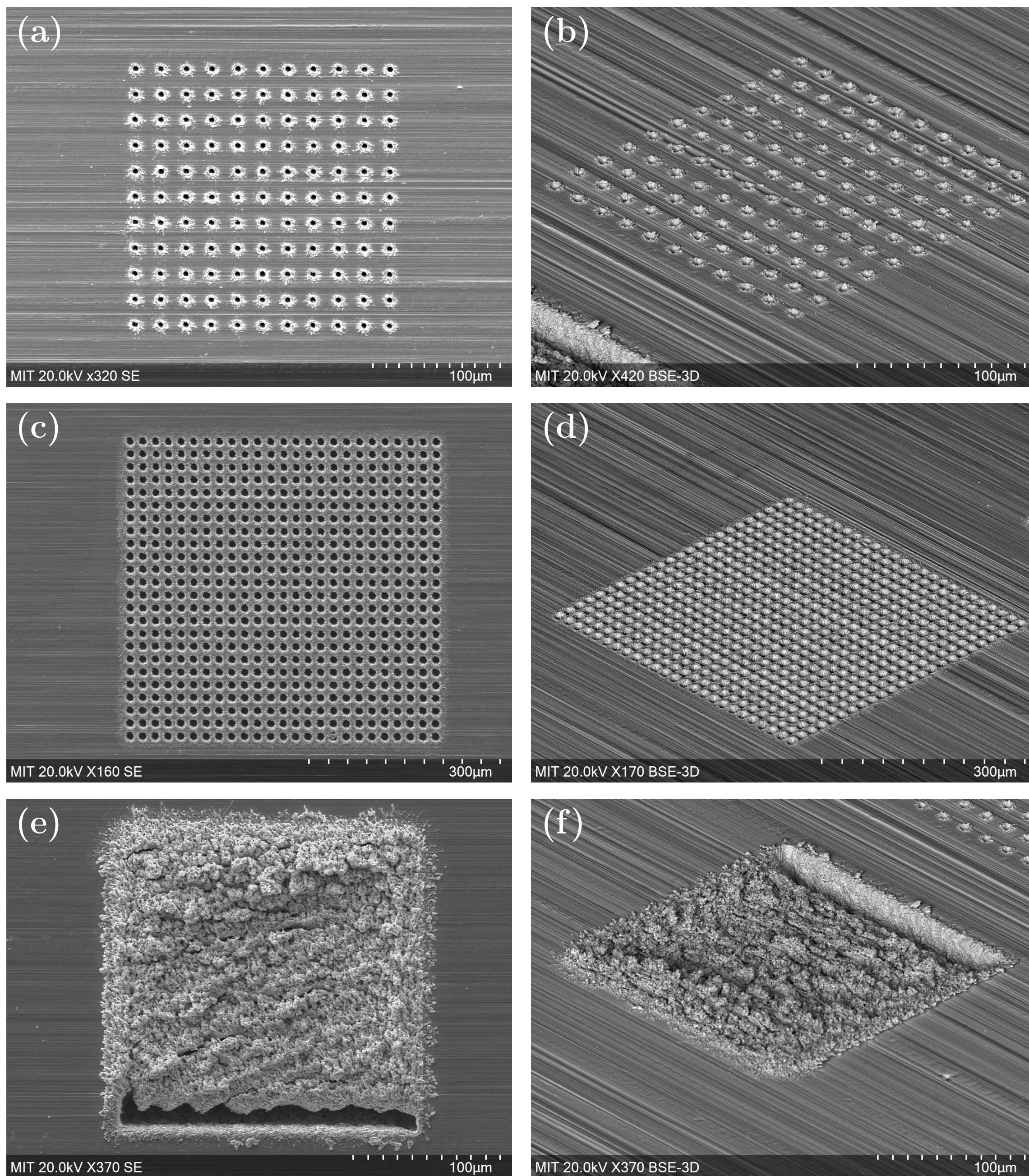

Figure 3-5: Pulse exposure with varying pitch distance to confirm material melting & expulsion. (a) & (b) Pitch = $20\mu m$, (c) & (d) Pitch = $10\mu m$, and (e) & (f) Pitch = $5\mu m$.

surface heat source with Gaussian intensity distribution. Thus the intensity distribution is given by the expression:

$$I(r) = I_0 exp\bigg(-\frac{r^2}{\omega_0^2}\bigg) \tag{3.8}$$

where maximum intensity, $I_0 = 71.5GW/cm^2$ and the radius of the focused beam, $\omega_0 = 0.5\mu m$ (Table 3.1)

The laser-assisted material phase-change and expulsion (LAMPE) is modeled by adding a phase-change (i.e., melting) heat flux thermal boundary condition to the heat diffusion equation and removing the melted material from the modeling domain. The heat flux due to melting can be modeled using the expression [68]:

$$q_m = h_m(T - T_m) \tag{3.9}$$

where q_m is heat flux due to material melting, T_m is the melting temperature and h_m is the temperature-dependent heat transfer coefficient.

The value of h_m is zero below the melting temperature, and increases linearly above the melting temperature. In COMSOL, h_m is modeled as a ramp-function and the slope is set such that the temperature of the material does not significantly increase above the melting temperature. Finally, the material expulsion is modeled by assigning a velocity to the solid boundary. This velocity is given by the expression:

$$v_m = \frac{q_a}{\rho \Delta H_m} \tag{3.10}$$

where v_m is the material melting velocity, ρ is the material density, and ΔH_m is enthalpy of fusion.

The heat diffusion equation is solved for the duration of the laser pulse ($20ns$). Figure

3-6 shows the LAMPE micromachining profile of copper using a single pulse of laser. The LAMPE process is isotropic, and the minimum achievable feature size is of the order of $5\mu m$. This results agree with the analytical estimates (3.3.2) and the experimental findings (3.3.1). The next section describes fabricating high aspect ratio (HAR) microstructures using the LAMPE micromachining process.

3.4 LAMPE High-Aspect-Ratio Micromachining

We saw in the previous section that short laser pulses can be utilized to melt, partially evaporate, and expel the material. The analytical model, along with process development, can be used to empirically estimate the pulse duration and threshold pulse energy E_{LAMPE} required for achieving laser-assisted melting and expulsion.

The high aspect ratio machining is achieved by setting the pulse energy to E_{th} to ensure melting and expulsion, and using the laser to gradually melt the vertical face of the laminate (shown in figure 3-1(b), and expel it downwards. The expelled material resolidifies at the rear of the sheet, as shown in figure 3-8. This process is similar to laser-cutting at macro-scale where metal is melted and expelled using the high-pressure air jet. However, in the LAMPE process, the material is expelled using the pressure generated by vapor baubles formed at the laser-material interface due to the partial vaporization of the material.

Figure 3-7 shows the $10\mu m$ wide micro-slights fabricated using LAMPE micromachining on a $100\mu m$ thick copper sheet. The high aspect ratio (HAR) structure is fabricated using the pulse energy of $56\mu J$, which is set by reducing the original pulse energy of $561\mu J$ to its 10% value using an external attenuator. The reflectivity of the copper target, $R = 0.47$; therefore, the effective energy available for material processing is $32\mu J$. The laser beam is focused using a $100mm$ focal length lens and the focused beam spot diameter is $12.98\mu m$. Table 3.2 summarizes the laser conditions used for the LAMPE micromachining process.

In the LAMPE micromachining process, the expelled metal resolidifies at the edges of the micromachined part creating micro-burrs. Figure 3-8 shows the SEM image of the backside

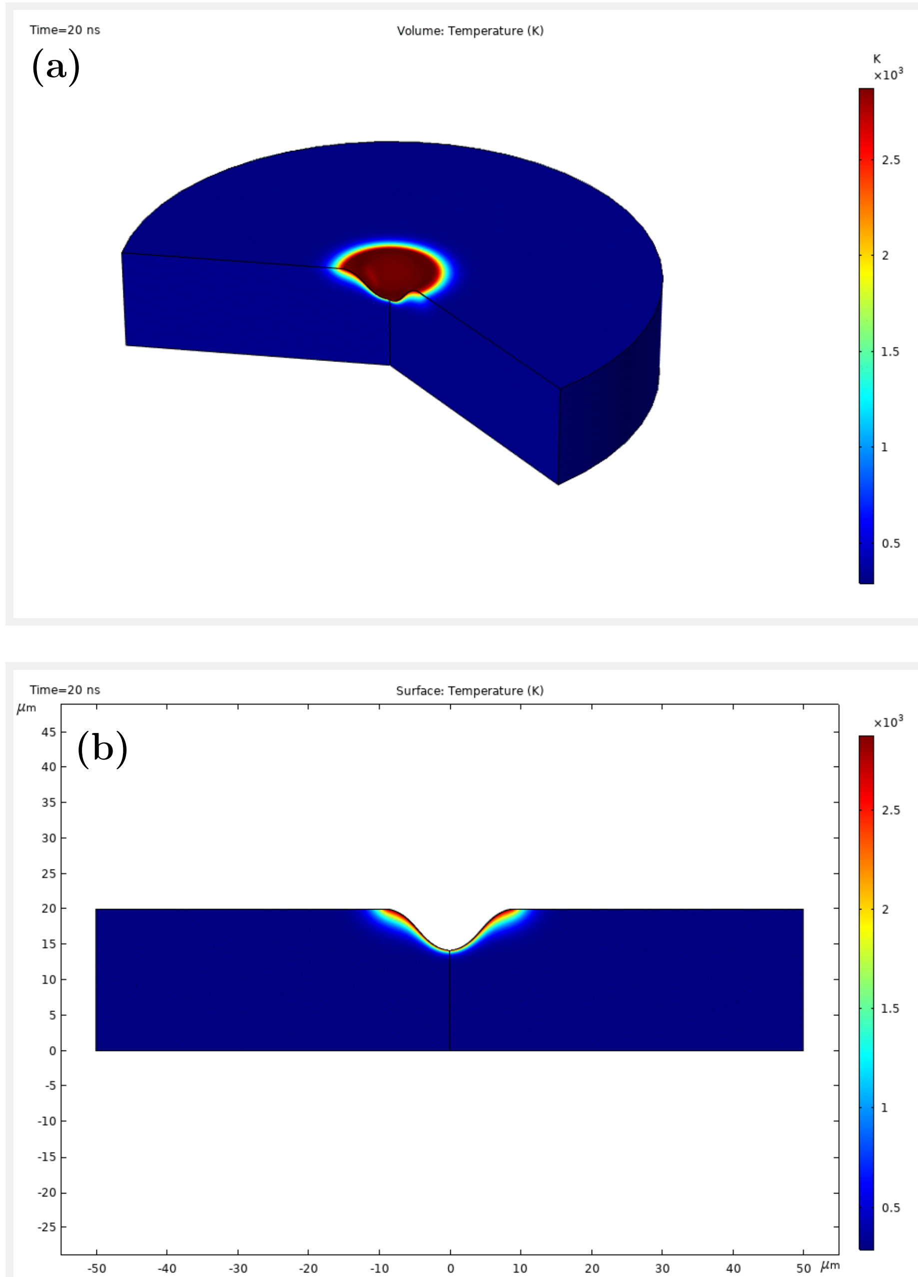

Figure 3-6: Simulation of LAMPE micromachining of copper. (a) Isometric view of ablated profile, and (b) Side view of the ablated profile showing crater width and depth.

Laser Parameter	**Value**
Wavelength, λ	$532nm$
Average Power, P_{avg}	$280mW$
Pulse Frequency, F_p	$5KHz$
Pulse Duration, τ_l	$\approx 20ns$
Reflectivity of Copper, R	0.43
Pulse Energy, E_p	$32\mu J$
Peak Power, P_{pk}	$2.8kW$
Beam Spot size, $2\omega_0$	$12.98\mu m$
Rayleigh Length, Z_R	$850\mu m$

Table 3.2: Laser parameters for LAMPE micromachining high aspect ratio (HAR) features.

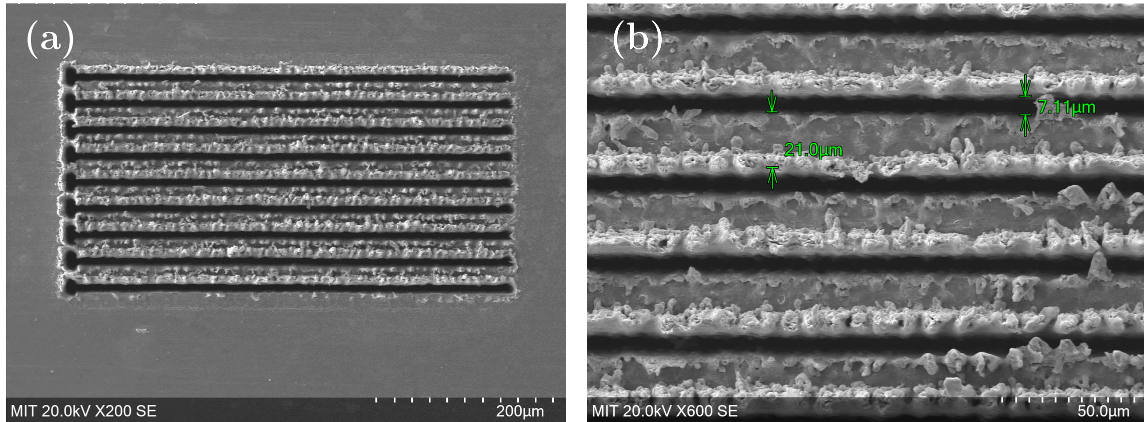

Figure 3-7: High-aspect-ratio microfabrication using LAMPE micromachining. (a) $10\mu m$ wide micro-slits fabricated on $100\mu m$ thick copper sheet using LAMPE micromachining. (b) Magnified image showing the dimension of the micro-slit.

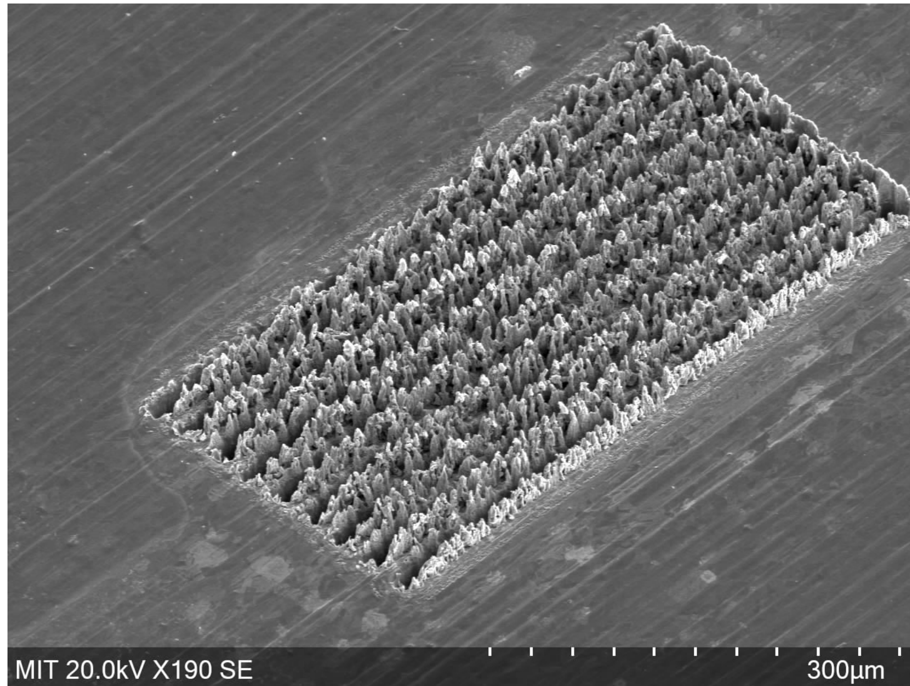

Figure 3-8: SEM image of the backside of the LAMPE micromachined copper sheet showing resolidified melt ejects.

of the LAMPE micromachined copper sheet, displaying the micro-burrs. These micro-burrs must be removed from the laser micromachined part to make them suitable for MEMS fabrication. The next section describes the developed electro-deburring process to remove these micro-burrs.

3.5 Electro-deburring of LAMPE Micromachined Parts

The LAMPE micromachining process can create small lateral features with high aspect ratio. However, the micromachined parts suffer from resolidified micro-burrs. These burrs pose two difficulties in making MEMS. First, in a typical MEM system, microstructure parts are very close to each other (typically as close as $5\mu m - 10\mu m$), and often held at a different electric potential. For example, in an electrostatic comb-drive actuator, the comb fingers are kept close to each other to increase the electrostatic force of attraction and a bias voltage is applied between the fingers. The protruding burrs can create electric contact between these

fingers. Second, the sharp metal protrusion can generate field-emitted electrons resulting in the dielectric breakdown of air, thereby causing damage to the MEM system [69].

Removing the burrs in MEMS microstructures is challenging due to two reasons. First, macro-scale deburring processes such as physical scrub and abrasive jet can not be utilized for MEMS structures due to their small size and delicate nature. Second, at macro-scale, etching process can etch the burrs without significantly affecting the dimensions of the parts. However, in MEMS parts, the burrs and the features are of the same order, and these methods result in significant etching of the parts.

This thesis develops a procedure to remove micro-burrs without affecting the MEMS microstructures. The process setup is similar to electropolishing process and utilizes the high-voltage regime. Figure 3-9 shows the polarization curve for copper electropolishing in phosphoric acid. As can be seen in figure 3-9, the current first increases linearly followed by a plateau and then increase linearly again. In the plateau region and beyond, the current density is uniform across the surface of the part due to the saturation of mass transport species [70], resulting in saturation of etch rate.

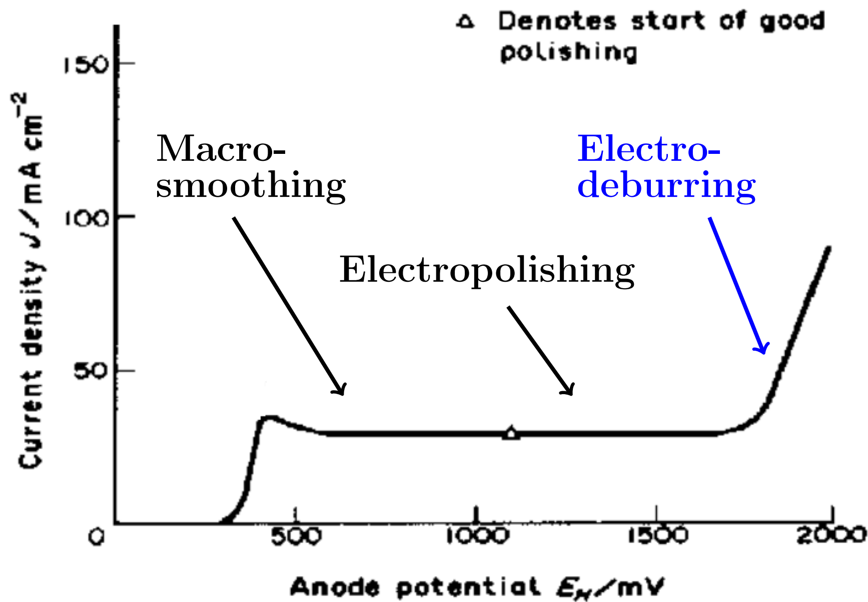

Figure 3-9: Polarization curve of copper in phosphoric acid [70]

The burrs produced in LAMPE micromachining process have two interesting properties; first, these burrs have sharp features and large surface area, and second, they are located at the edges of the micromachined parts. The current density is higher near the burrs due to two reasons: first, the burrs have sharp features, and second, they are located at the edges where the current density is higher. As a result, the electric field and the available mass transport spices are high at the burrs, resulting in a high etch rate. When the cell voltage is increased beyond the electropolishing voltage, the etch rate at the burr increases significantly; however, the etch rate at the other area remains the same due to saturation in the etch rate. Using this phenomenon, the burrs can be selectively etched without significantly affecting the dimensions of the micro-parts.

Figure 3-10 shows performing electro-deburring of copper in $14M$ phosphoric acid at $5V$ for 30 seconds. For certain application, electro-deburring can be followed by electroplating of gold to avoid surface oxidation.

Figure 3-11 shows the high aspect ratio interdigitated fingers fabricated using the LAMPE micromachining. Such small features and high aspect ratio were previously achievable only using deep reactive ion etching (DRIE).

It must be noted that for MEMS that does not require small lateral-features and high aspect ratio, traditional pulsed laser ablation (PLA) micromachining in conjunction with the electro-deburring process can be used for MALL MEMS fabrication.

3.6 LAMPE Micromachining of Silicon

3.6.1 Introduction

Silicon is widely used as a mechanical material for fabricating MEM systems [71]. Conventionally deep reactive ion etching (DRIE) of silicon is used to fabricate MEMS [72]. However, DRIE tools are expensive and require expensive etching gases. The LAMPE micromachining is an attractive alternative for manufacturing high aspect ratio (HAR) microstructure silicon laminates. Moreover, these LAMPE micromachined silicon

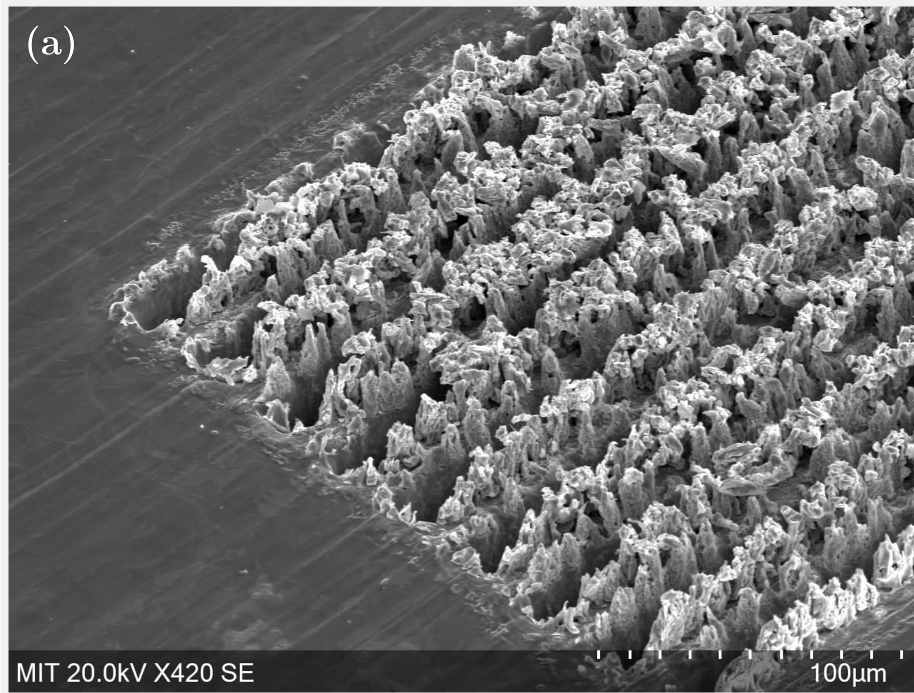

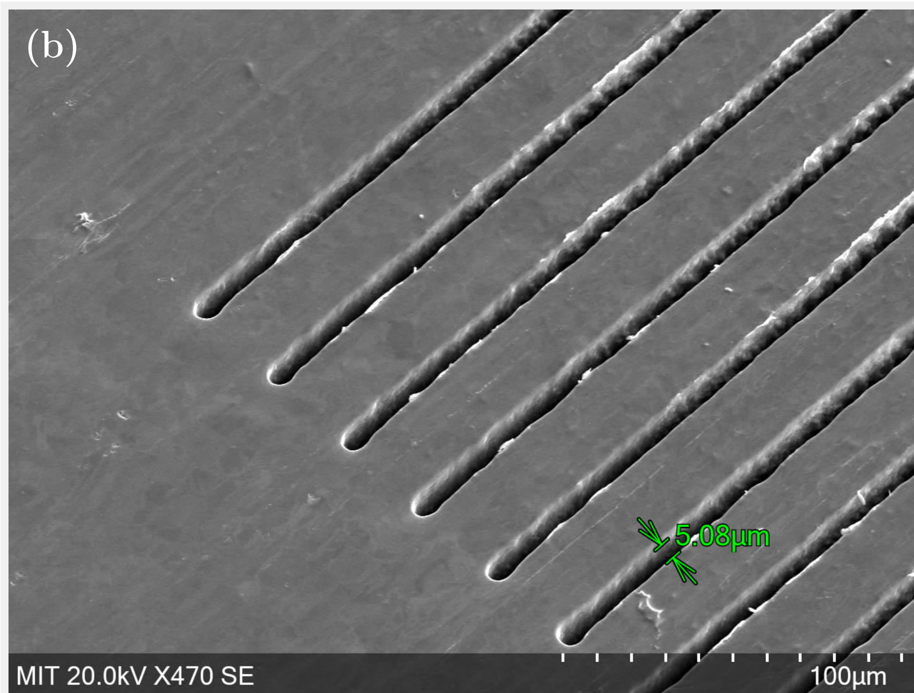

Figure 3-10: Electro-deburring of LAMPE micromachined parts to remove micro burrs. (a) Before electro-deburring. (b) After electro-deburring.

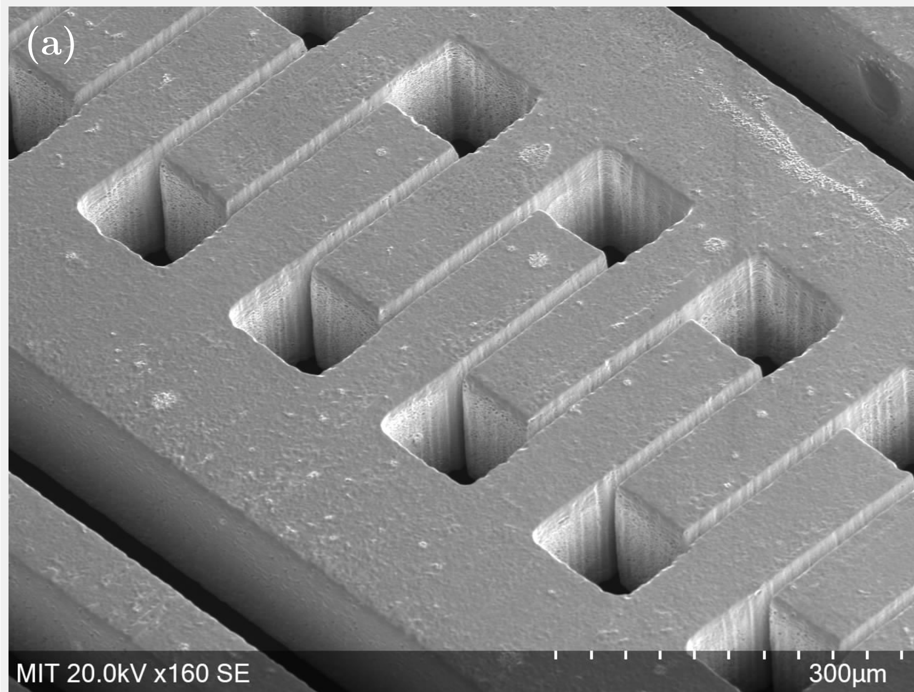

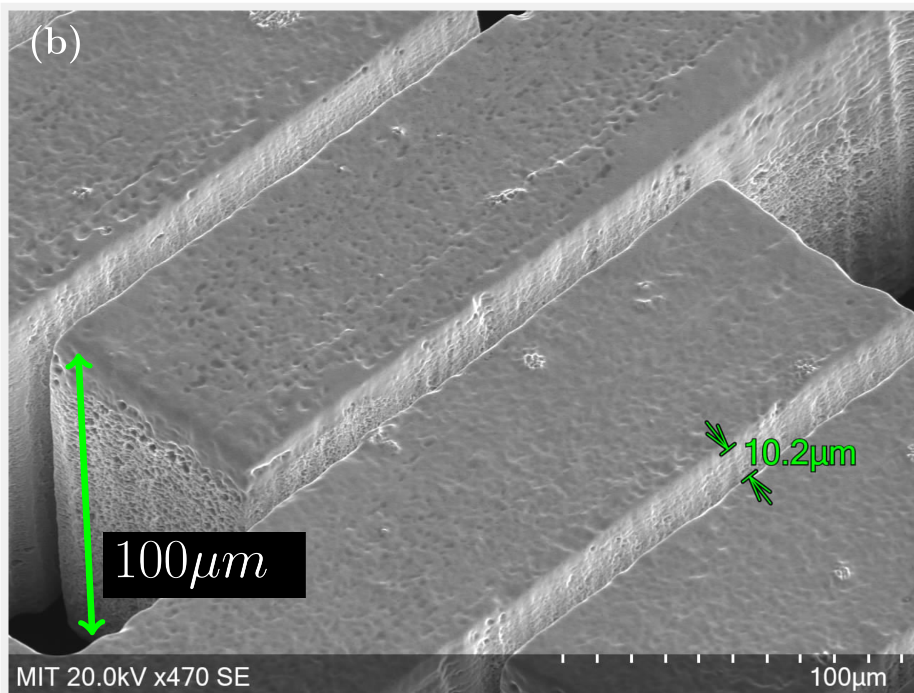

Figure 3-11: High aspect ratio interdigitated fingers fabricated using the LAMPE micromachining. (a) Low-magnification image showing the interdigitated fingers. (b) Magnified image of the fingers showing 10:1 aspect ratio. The lateral feature size is $10\mu m$.

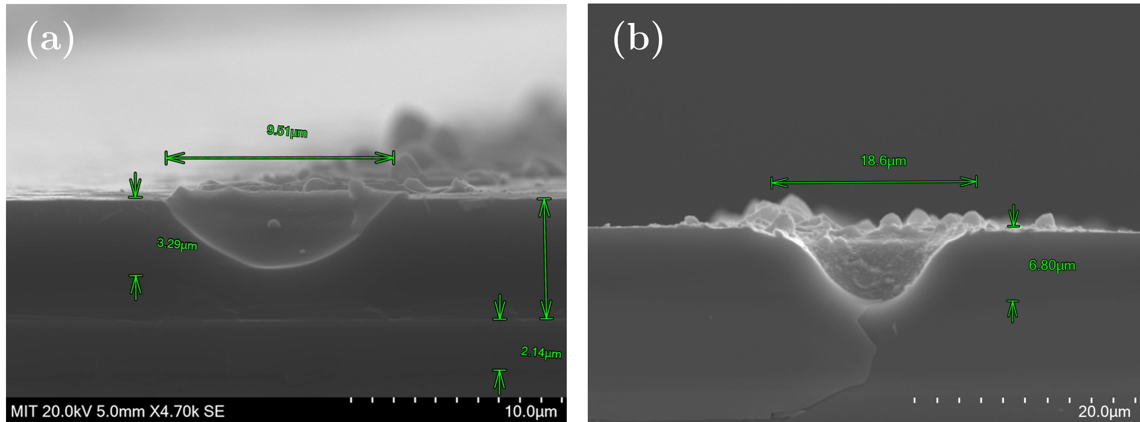

Figure 3-12: Pulsed laser ablation (PLA) of silicon using $20ns$ long laser pulses. (a) Ablation profile created by a $5.6\mu J$ pulse. The diameter of the crater is $9.51\mu m$ and it is $3.29\mu m$ deep. (b) Ablation profile created by a $56\mu J$ pulse. The diameter of the crater is $18.6\mu m$ and the depth is $6.8\mu m$.

laminates in conjunction with the MALL process, can be used to make MEM systems.

The absorption coefficient of silicon at $532nm$ is $\alpha_{Si} = 9 \times 10^3 cm^{-1}$ [55]; therefore, the optical penetration depth is $l_\alpha = 1\mu m$. Due to the shallow penetration depth, the laser can be modeled as a surface heat source, and the temperature distribution can be determined by solving the heat diffusion equation. Figure 3-12 shows the finite element analysis (FEA) of heat distribution in the pulsed laser ablation process.

When the temperature reaches the boiling point of the silicon, the material is vaporized, forming an ablation creator. Figure 3-12 (a) & (b) show the ablation profile created by a single laser pulse of energy, $5.6\mu J$ and $56\mu J$, respectively. The ablation profile shown in figure 3-12 agrees with the features reported in literature [73][74][75][76][77][78][79]. The aspect ratio is limited due to small optical penetration depth and small heat diffusion length. Although multi-pulse ablation can be used to increase the aspect ratio, the saturation depth is quickly reached because of the inefficient removal of material due to narrow space and the absorption of the laser by vapor plasma. Due to the large lateral features and low aspect ratio, the application of laser-micromachining silicon has been largely limited to drilling holes and wafer dicing.

Karnakis et. al. [80] reported micromachining silicon with small lateral features in the

order of $10 - 20\mu m$ and high aspect ratio exceeding the optical penetration depth. The high aspect ratio has been attributed to a homogeneous bubble nucleation phase explosion mechanism [80][81]. This thesis shows further reducing the lateral features down to diffraction-limited spot size and increase in aspect ratio using the LAMPE micromachining process. In the LAMPE process, first, the silicon is converted into silicon oxide using laser (i.e. induce phase-change), and next, the silicon oxide is expelled from the rear of the wafer using the pressure generated from vapor baubles formed at the laser-silicon interface due to partial vaporization of silicon.

When silicon is irradiated with low power laser in the oxygen environment, it converts to silicon oxide without resulting in any ablation. The absorption coefficient of SiO_2 is $\alpha < 1cm^{-1}$ [55]; therefore, the optical penetration depth is $l_\alpha > 1cm$. Since the absorption coefficient of silicon oxide is low, the newly formed silicon oxide transmits the large percentage of the laser energy, which further oxidizes the silicon beneath. In this manner, a high aspect ratio structure much longer than the optical penetration depth of silicon can be oxidized. Figure 3-13 shows the laser-assisted oxidation of silicon. As can be seen, the oxidation length far exceeds the optical penetration depth. The oxidation of the silicon can be verified by using an optical microscope and energy-dispersive x-ray spectroscopy (EDS) image as shown in figure 3-14

The successive oxidation of silicon takes place until the bottom of the wafer is reached. The oxidized silicon is in granular form and loosely bound to the silicon wafer. As a result, the small recoil pressure generated by partially vaporized silicon is sufficient to expel the granular silicon oxide from the bottom of the wafer, resulting in micromachining.

The maximum achievable aspect ratio is limited by two factors. First, the oxidized silicon exists in granular form and the effective absorption coefficient of granular oxide is larger than bulk silicon oxide due to light scattering. Second, the silicon oxide is expelled only when the oxidation is reached to the bottom of the wafer. As a result, for thick wafers, the attenuation could be significant to stop oxidation before the rear of the wafer is reached, thereby resulting in no micromachining. The aspect ratio in LAMPE micromachining could

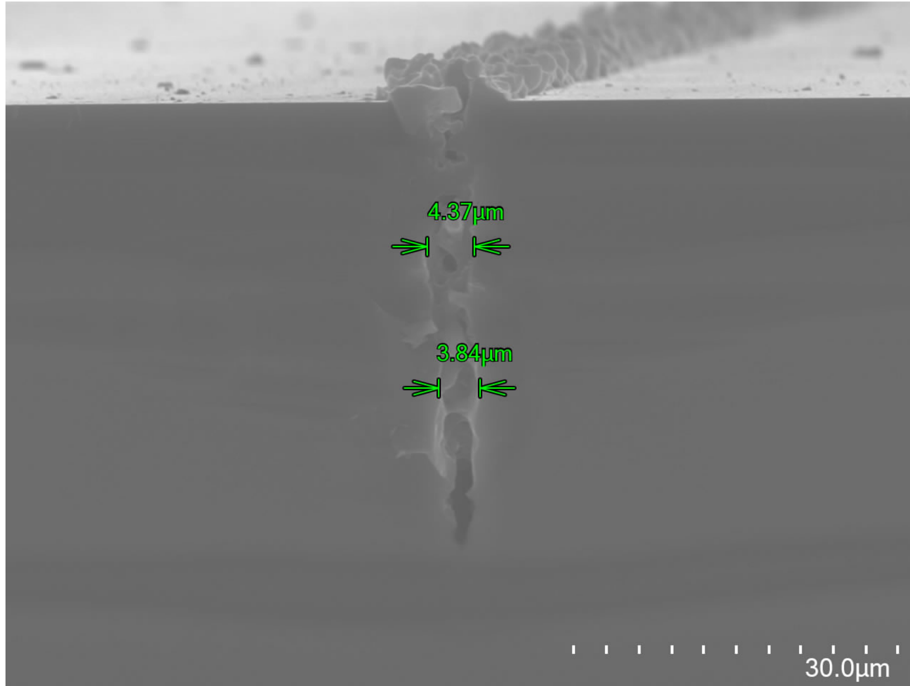

Figure 3-13: The cross-section image showing laser assisted oxidation of silicon. As can be seen, the laser assisted oxidation can significantly increase the "effective optical penetration depth".

be further increased by performing the micromachining in HF vapor. The HF vapor can facilitate the selective removal of silicon oxide by forming gaseous SiF_4.

3.6.2 Numerical Simulation

The time evolution of the increase in "effective optical penetration depth" due to oxidation of silicon can be simulated using finite element analysis. The intensity of the laser beam is reduced to 10% of the intensity using an external attenuator, and the reduced peak intensity is $I_0 = 4.2GW$ (see figure 2-5). The radius of the focused beam is $\omega_0 = 6.48\mu m$. The Gaussian intensity profile of the beam is given by the equation:

$$I(r) = (1 - R)4.2GWexp\left(- \frac{2r^2}{6.48\mu m^2} \right) \tag{3.11}$$

Beer-Lambert law is used to model the absorption of the laser. The phase-change from silicon to silicon oxide is modeled by changing the absorption coefficient of the material

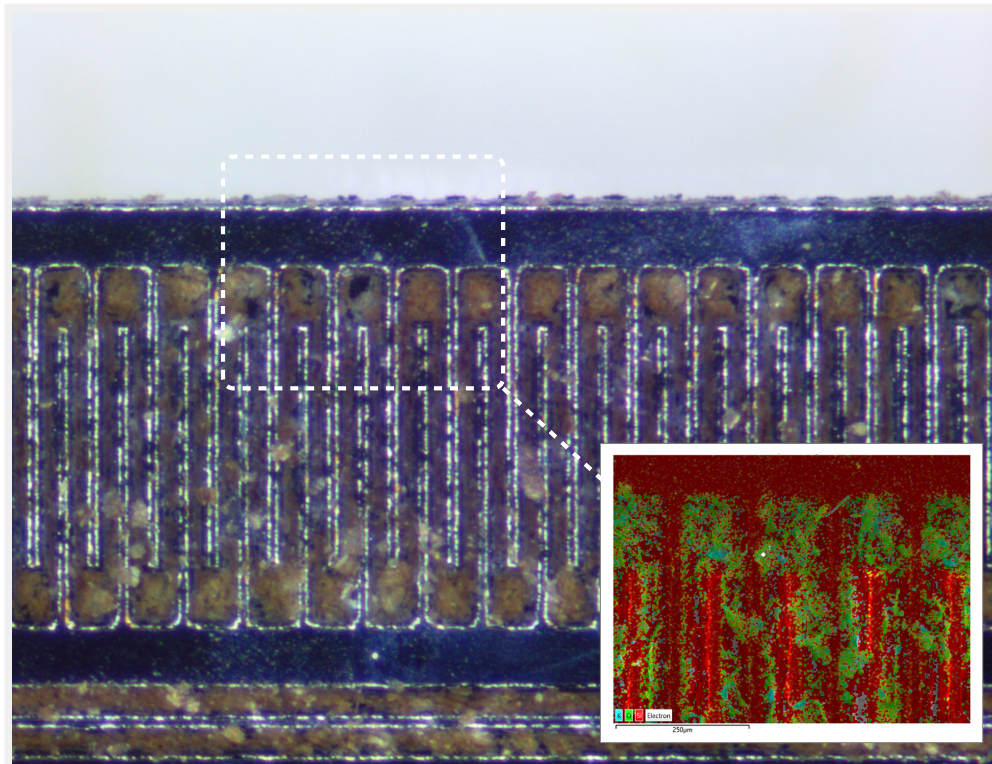

Figure 3-14: The optical microscope image confirming the oxidized silicon. The energy dispersive x-ray spectroscopy (EDS) image shown in the inset further confirms the present of silicon oxide.

after phase-change and by introducing a heat flux due to oxidation. Figure 3-15(a) shows the temperature profile in silicon during conventional pulse ablation. Figure 3-15(b) shows the distribution of the temperature in silicon when silicon oxidation and change in absorption coefficient is taken into account. It can be seen in figure 3-15(b) that the oxidation of silicon significantly increases the "effective optical penetration depth". Note that the expulsion of the material is not simulated due limitation of the FEA package.

3.6.3 Results & Discussion

Figure 3-16 shows the comb micro-structure fabricated using LAMPE micromachining of silicon. The LAMPE micromachined silicon structures reported in this thesis are comparable to the structures fabricated using deep reactive ion etching (DRIE) [82].

The laser fluence required for the LAMPE micromachining process is much lower than the pulse ablation micromachining. As a result, the described process significantly reduces the power requirement of laser source and could be an attractive method to prototype silicon MEM systems. It must be noted that since the material is expelled from the rear of the substrate, the LAMPE micromachining is limited to fabricating lamina microstructures.

LAMPE Micromachining Rate

The machining rate in LAMPE micromachining process is given by the expression:

$$LAMPE\ Micromachining\ Rate = \frac{\eta \omega_0 t f}{N} \tag{3.12}$$

where $\eta = distance\ between\ the\ neighboring\ irradiation\ spot/laser\ beam\ diamter$ and generally set to $\eta = 0.25$, ω_0 is the diameter of focused laser beam, t is the thickness of the wafer, f is the micromachining feed rate, and N is the number of passes required to completely remove the material. For the LAMPE micromachining of silicon described above, the wafer thickness is $t = 50\mu m$, and the laser beam spot diameter is $\omega_0 = 10\mu m$, and it is empirically determined that $\eta = 0.25$, $f = 60\ mm/min$, and $N = 10$. Substituting these

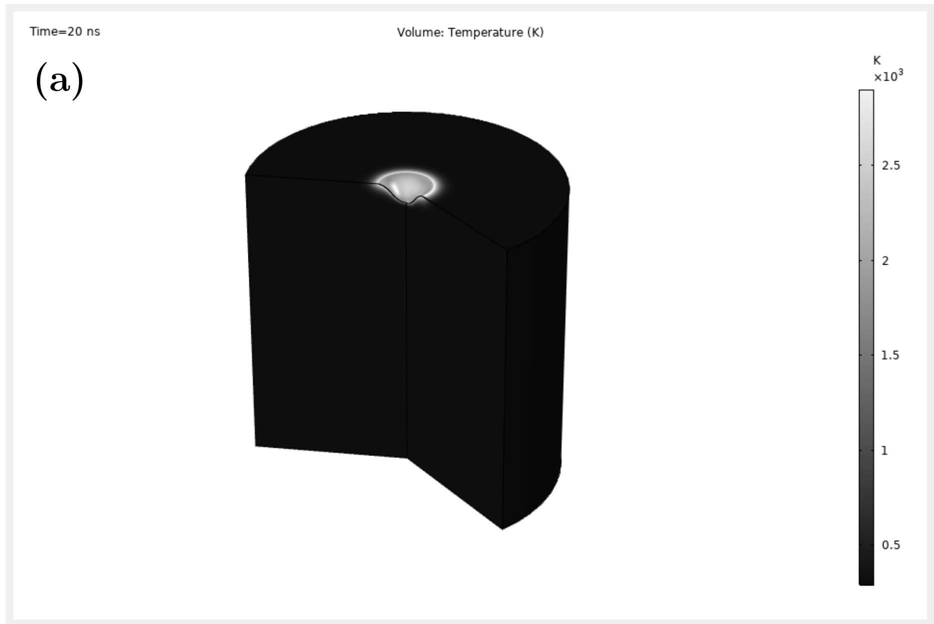

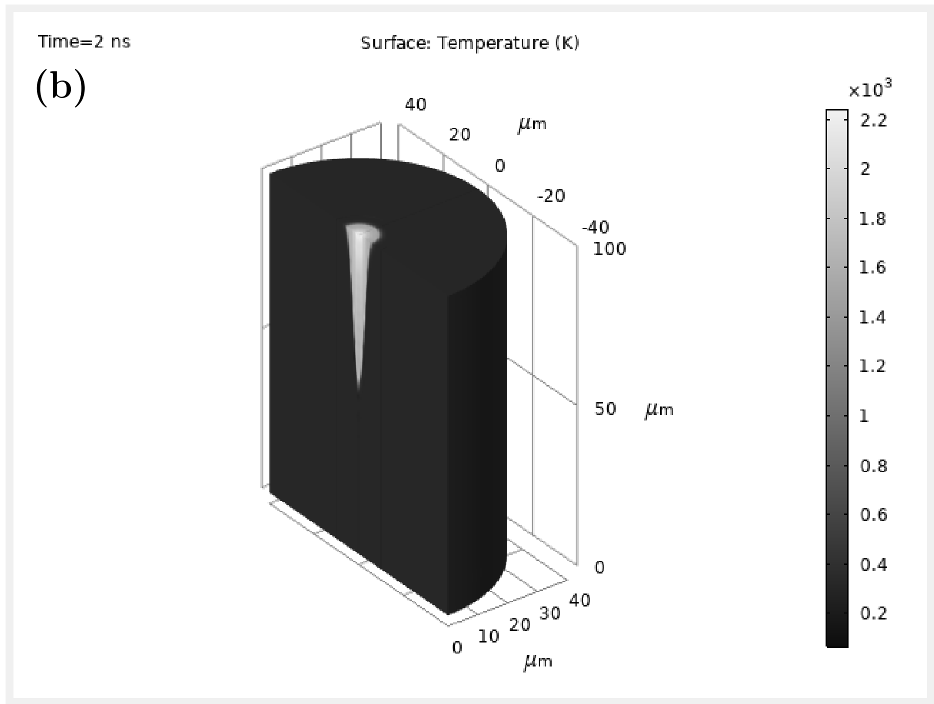

Figure 3-15: (a) Simulation of pulsed laser ablation of silicon, and (b) Simulation of LAMPE micromachining of silicon.

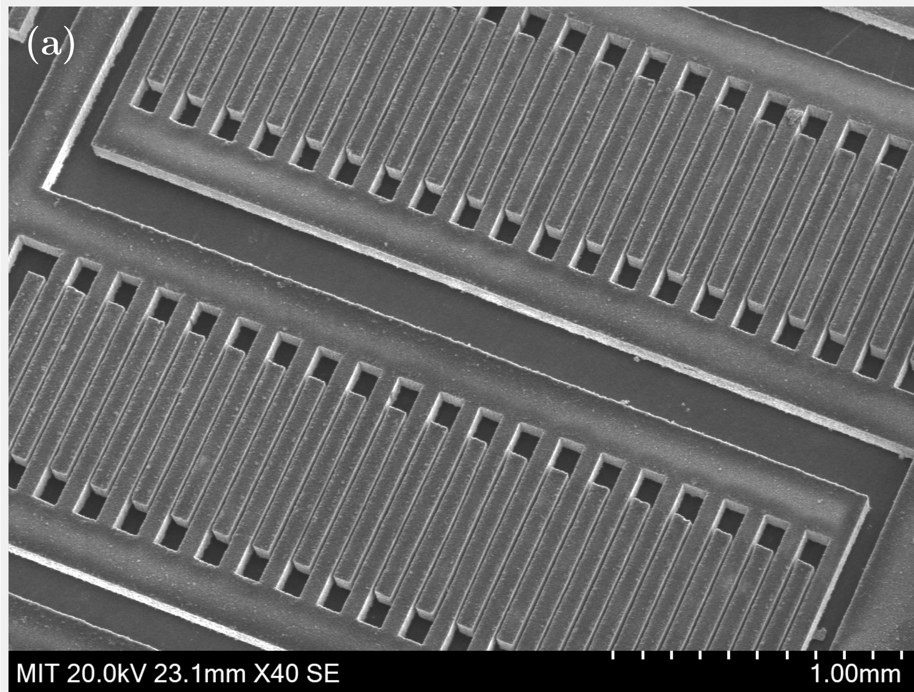

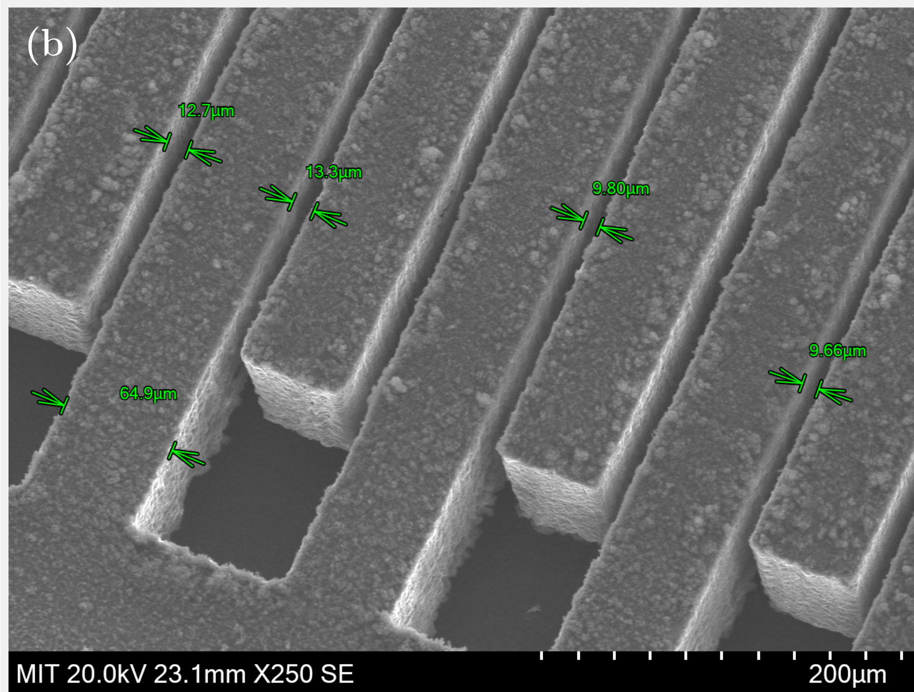

Figure 3-16: Examples of high-aspect-ratio microstructures fabricated using LAMPE micromachining of silicon. (a) Low-magnification image showing fabricated interdigitated finger structures. (b) High-magnification image showing the distance between the fingers.

values in (3.12), we get $LAMPE\ Micromachining\ Rate = 7.5 \times 10^5 \mu m^3/min$.

3.7 Conclusions

This chapter concludes that laser micromachining, utilizing the LAMPE process, can fabricate high aspect ratio structures with lateral features as small as the diffraction-limited spot size of the laser. Previously, fabricating such high aspect ratio structures with small lateral features was not possible using any fabrication process (including the pulse laser ablation micromachining).

In the LAMPE process, the laser is used to melt and shift the material, and then the shifted material is removed utilizing the electro-deburring process. Using this process, high aspect ratio structures are fabricated by utilizing the laser to melt the vertical face of the sheet and expelling it downward (shown in figure 3-1(b)), and then removing the expelled material using electro-deburring. Using the LAMPE process, I have shown fabricating 10:1 aspect ratio structures with lateral feature size of $10\mu m$.

The LAMPE micromachining process can also be used to fabricate high aspect ratio (10:1) structure in silicon with lateral features as small as $10\mu m$. In the LAMPE micromachining of silicon, the laser is used to turn silicon into granular silicon oxide. The silicon oxide is then removed by the pressure generated by vapor bubbles formed at the laser-silicon interface. It must be noted that no deburring is required for silicon as the oxide is in the powder phase and gets expelled from the silicon substrate. Although similar features can be produced using deep reactive ion etching (DRIE), the LAMPE micromachining of silicon enables low-cost fabrication and rapid prototyping.

The LAMPE process can be implemented by using the appropriate laser power and pulse duration. The appropriate laser power required for LAMPE micromachining can be calculated using the procedure described in section 3.3.2. Similarly, the laser pulse duration can be estimated using the eq. (3.5), for a desired lateral-feature size. However, it must be noted that some degree of process development is required to achieve the minimum feature

for a given aspect ratio.

The main advantage of the LAMPE process is that it enables high aspect ratio machining that was not achievable previously. Moreover, the laser power required for LAMPE micromachining is less than the laser power required for pulsed laser ablation micromachining. The main disadvantage of the LAMPE process is that it only allows micromachining material laminates. In other words, the LAMPE process can not be used to fabricate 2.5D structures.

Chapter 4

MALL MEMS Fabrication

The MALL MEMS fabrication process consists of two steps. First, the individual layers of the MEMS are fabricated using laser micromachining. Second, these layers are stack assembled and bonded to construct the MEM systems. In the previous chapter, I showed fabricating microstructure laminates using the LAMPE micromachining process. In this chapter, I will show assembling these microstructure layers to fabricate the MEM systems. Further, I will demonstrate fabricating a comb-drive actuator and a MEM relay using the MALL fabrication method. Section 4.1 describes the multi-lamina assembly process used to align and bond the laminate layers.

Section 4.2 describes fabricating a comb-drive actuator using copper as a structural material. The comb-drive actuator is selected because the interdigitated comb finger structure is an essential building block in many MEM systems such as optical shutters [21], micro-grippers [83], microengines [84], accelerometer [22], resonators [23], and electromechanical filters [24]. The ability to fabricate interdigitated comb finger structures using copper can significantly reduce the cost of these MEM systems. Moreover, fabricating comb fingers is challenging because it requires high aspect ratio structures with small lateral features. Previously, comb fingers with comparable features and aspect ratio could be fabricated from silicon alone using the lithography-based deep reactive ion etching (DRIE) process [28]. However, in this thesis, I will demonstrate fabricating these

structures using the LAMPE micromachining process.

Section 4.3 describes fabricating a MEM relay using the MALL fabrication process. These MEM relays could be used for high-current switching applications. Finally, section 4.4 shows fabricating a high-aspect-ratio diamond rotor for enhancing the resolution of magic-angle spinning nuclear magnetic resonance spectroscopy (MAS-NMR).

4.1 Multi-Lamina Assembly

The second step in the MALL process is to stack assemble the LAMPE micromachined laminates to fabricate MEM systems. For many MEMS, the alignment accuracy better than a few micrometers is desirable. Mechanical alignment of laminates using dowel pins and alignment holes is widely used in precision macro-fabrication. This method is employed to align and bond microstructure laminates. The alignment accuracy exceeding $2.5\mu m$ is demonstrated using the method.

Figure 1-4 shows the schematic diagram of the alignment-pin and alignment-hole assembly process. The precise hand-assembly is carried out under an eyepiece-less stereo microscope with long working distance and large depth of focus [85]. The microscope uses multi-lenticular technology to provide true depth perception, which aids in hand-to-eye coordination; as a result, facilitating the micro-assembly process.

Four precision-ground alignment pins with $508\mu m$ diameter are used for alignment. The clearance between the alignment pin and alignment hole determines the alignment accuracy and must be minimized. For a given alignment pin, first, a series of holes is micromachined (figure 4-1(a)). Subsequently, the alignment pins are inserted and the clearance between the pin and the hole is measured (figure 4-1(b)). Finally, laser micromachining setting for the hole that gave the minimum clearance (figure 4-1(c)) is used to micromachine alignment holes.

To characterize the alignment accuracy, two layers with alignment marks are assembled and bonded. The bonded layers are illuminated from the rear, and the alignment marks

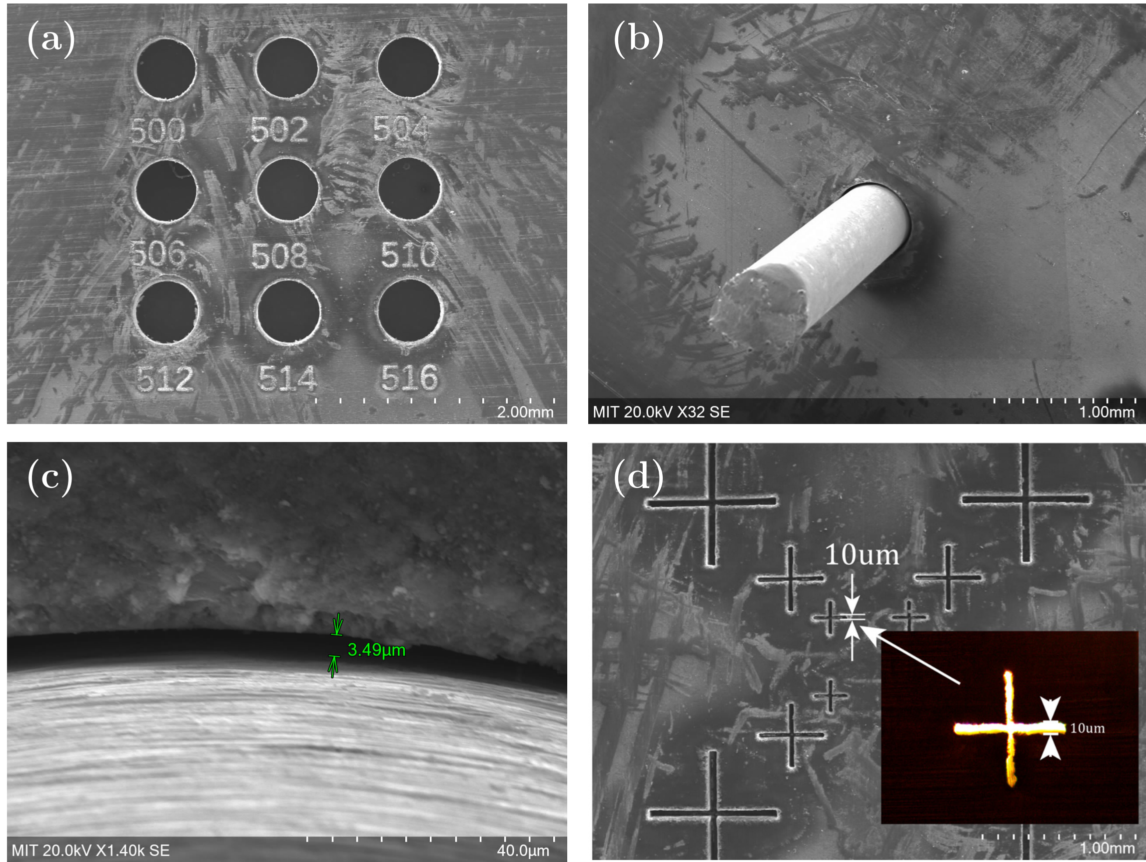

Figure 4-1: (a) Micro-assembly of discrete lamina sheets using alignment pins. (b) Alignment pin inserted inside the alignment hole. (c) The clearance between the alignment pin and the alignment-hole. (d) SEM image of aligned alignment marks, showing alignment accuracy down to $2\mu m$. The inset shows the black-lit optical image of an alignment of marks.

are studied using an optical microscope. The inset of figure 4-1(d) shows back-illuminated light transmitting through the two aligned marks. The width of the slit is $10\mu m$, and the overlap between the two aligned markers is better than 75%. As a result, it can be concluded that the alignment accuracy is better than $2.5\mu m$. The alignment accuracy can be further improved by creating passive alignment features in laminates [86][87][88].

The aligned layers are bonded using Dupont FR1500 and 3M thermal bonding film 583 adhesive sheets. For adhesion, the Dupont FR1500 is cured at $185°C$ for 5-20 minutes, depending upon the device design. Similarly, the 3M thermal bonding film 583 can be bonded by using pressure, applying solvent or heating at $120°C$. In some devices, it is desirable to first tack bond the adhesive sheet to one layer, and then attach another layer and perform complete cure for lamination. For tack bonding, the FR1500 sheet is cured at $120°C$ for 10 minutes, and 3M thermal bonding film 583 is pressure or solvent activated.

4.2 Comb-Drive Actuator

4.2.1 Design

Figure 4-2 shows the design of a comb-drive actuator. It consists of two sets of comb fingers. The width of each finger is $30\mu m$, and the length is $150\mu m$. The distance between the two sets of fingers is $10\mu m$. One of the finger structure is fixed while the other finger structure is connected to a compliant suspension spring. The suspension spring uses a folder-flexure design to minimize the side-pull between the fingers and maximize the lateral displacement [89]. The length of the beam is $1.66mm$, and the width is $20\mu m$. The thickness of the fingers and suspension spring is $100\mu m$. Lastly, the device is made of copper, and a $100\mu m$ thick aluminum oxide ceramic sheet is used as the insulating substrate. Table 4.1 lists the design parameters of the comb-drive actuator.

The spring constant of the folded-flexure design in the lateral direction is given by the

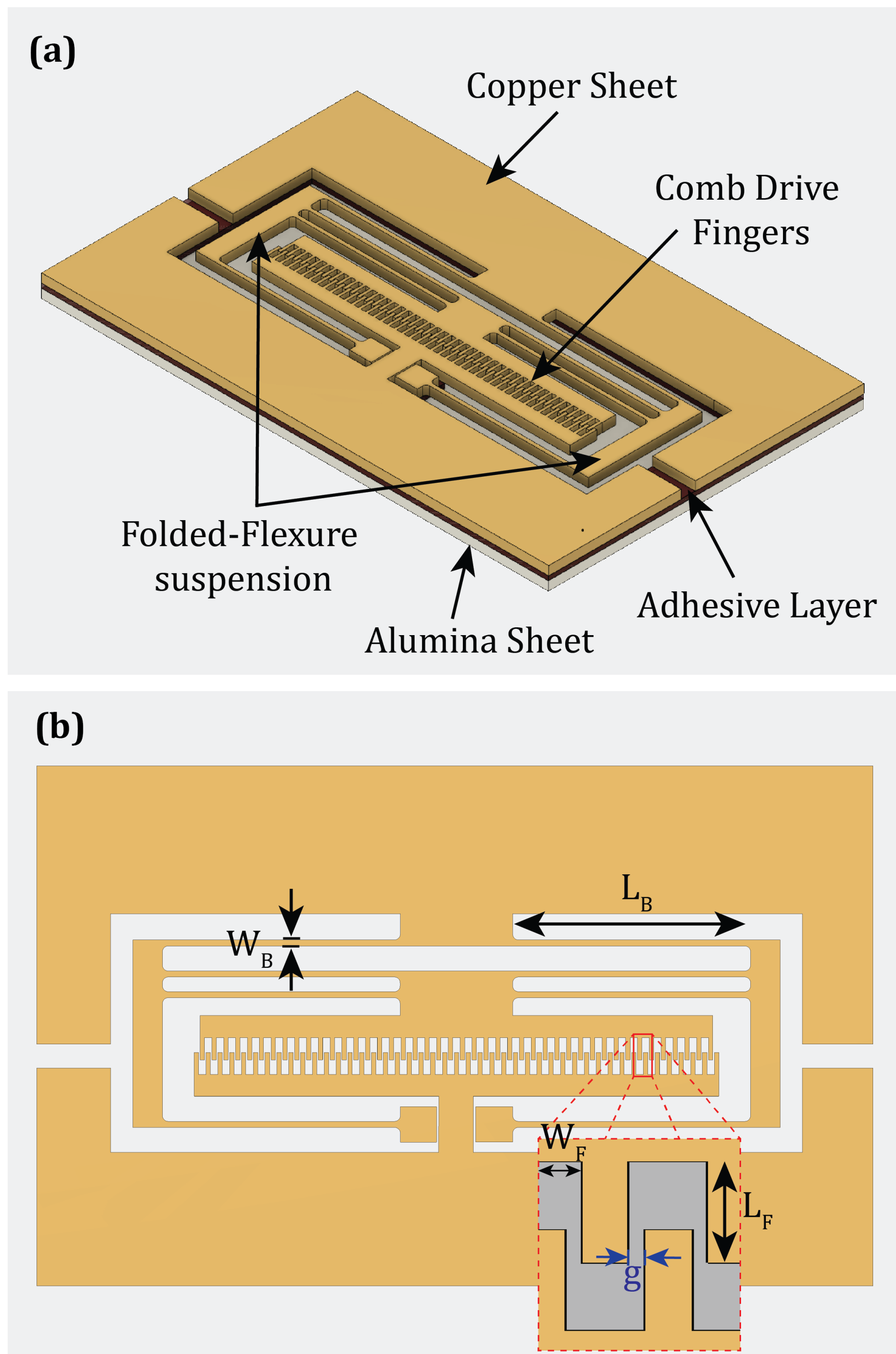

Figure 4-2: (a) Schematic diagram of the comb-drive actuator. (b) Diagram showing design parameters . These parameters are listed in Table 4.1.

Design Parameters	**Value**
Young's Modulus, E	$128GPa$ (Copper)
Beam Thickness, h	$100\mu m$
Beam Length, L	$1.66mm$
Beam Width, b	$20\mu m$
Spring Constant, k	$44.8N/m$
Comb Finger Length, L_F	$150\mu m$
Comb Finger Width, W_F	$30\mu m$
Comb Finger Gap, g	$10\mu m$
Number of Fingers, n	46
Applied voltage and corresponding displacement	@280V, d $= 7\mu m$

Table 4.1: Values of the design parameters for comb-drive actuator design.

expression [89]:

$$k = \frac{2Ehb^3}{L^3} \tag{4.1}$$

where E is Young's modulus, h is the thickness of beam spring, b is the width of the beam spring, and L is the length of the beam spring. Substituting the values of E, h, b and L from table 4.1, we get the spring constant of the folded-flexure spring as $44.8N/m$.

The electrostatic tangential force, F between the fingers is given by the expression [89]:

$$F = \frac{n\epsilon_0 hV^2}{g} \tag{4.2}$$

At equilibrium, the electrostatic force is balanced by the spring force; as a result, the equilibrium displacement at voltage V is given by the expression:

$$y = \frac{n\epsilon_0 hV^2}{kg} \tag{4.3}$$

The calculated value of displacement at $V = 280V$ is $7\mu m$.

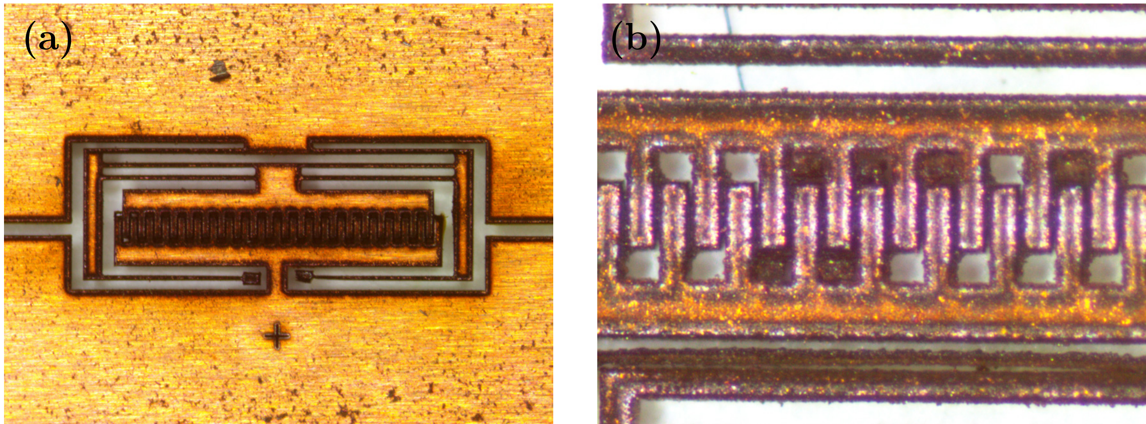

Figure 4-3: Fabrication of comb-drive device layer using LAMPE micromachining of copper: (a) Optical microscope image showing micro-burrs present in LAMPE micromachined part. (b) Magnified image showing micro-burrs present between the fingers. These burrs result in short-circuits between the two sets of fingers.

4.2.2 Fabrication

The fabrication of the comb-drive actuator consists of two steps. The first step is to fabricate the individual layer of the device using the LAMPE micromachining process. Figure 4-3(a) shows the optical microscope image of the LAMPE micromachined copper sheet containing the comb-drive device structure. As can be seen in figure 4-3(a), the micromachined part suffers from carbon deposits and micro-burrs. The micro-burrs result in electrical contact between the two sets of comb fingers (4-3(b)) and must be removed.

The micro-burrs are removed using the electro-deburring process described in section 3.5. The electro-deburring process is carried out in phosphoric acid, and the LAMPE micromachined part is used as the anode while another copper sheet is used as a cathode. The electro-deburring is carried out at $5V$ for 30 seconds. Figure 4-4(b) shows the SEM image of the comb-drive structure after removing the micro-burrs.

A $100\mu m$ thick aluminum oxide sheet is micromachined and used as an insulating substrate. Prior to micromachining the aluminum oxide substrate, a $50\mu m$ thick stage-B epoxy adhesive film is bonded to it. This adhesive layer is later used to bond the copper device layer with the aluminum oxide substrate layer. Figure 4-5 shows fabricated layers of the comb-drive actuator. For every layer,alignment holes are machined, in addition to the

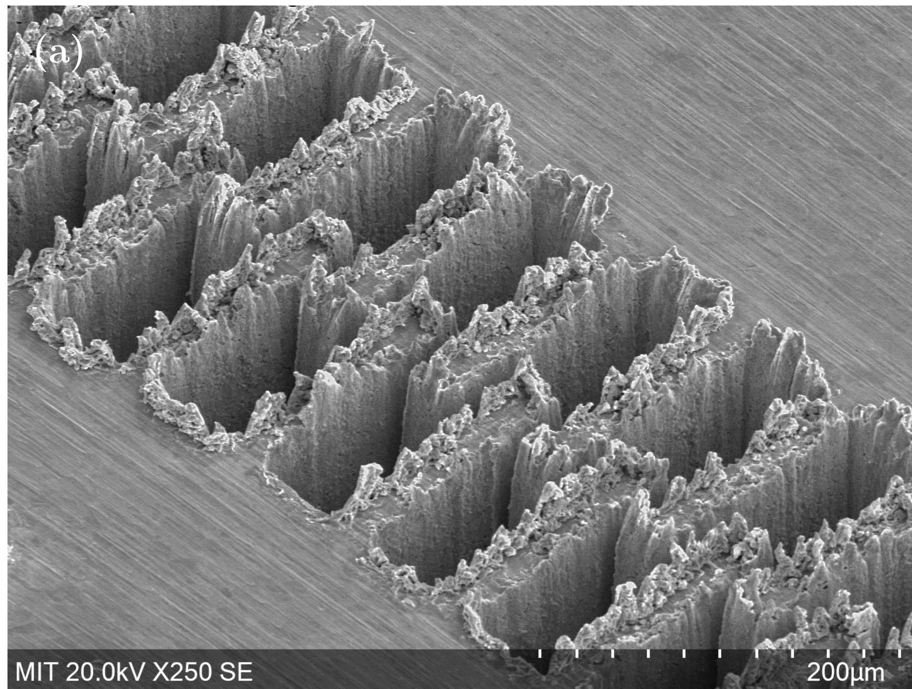

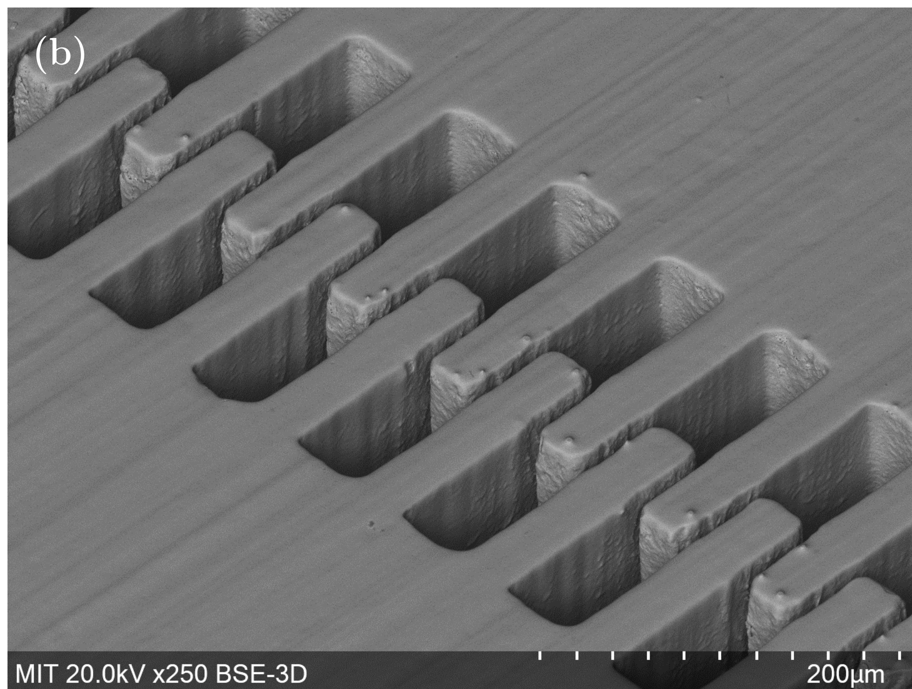

Figure 4-4: Electro-deburring of LAMPE micromachined comb-drive structure to remove the micro-burrs between the fingers. (a) Before electro-deburring. (b) After electro-deburring showing clean comb-drive fingers.

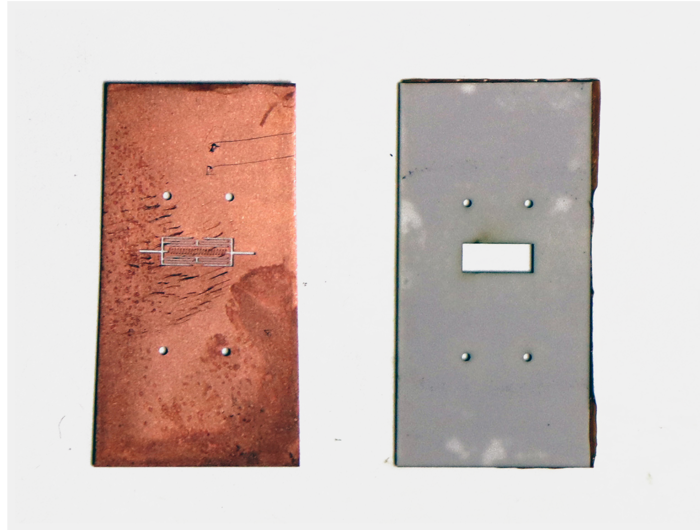

Figure 4-5: Layers of the comb-drive actuator fabricated using LAMPE micromachining. The copper layer is used for the device, and the aluminum oxide layer is used for the substrate layer.

device structure. These alignment holes are subsequently used for multi-lamina assembly.

The second step in the MALL MEMS fabrication method is the multi-lamina assembly of laser-micromachined laminates. This assembly process is described in section 4.1. Once the layers are bonded (figure 4-6(a)), the device is cut out from the laminate structure using laser cutting (figure 4-6(b))

4.2.3 Results & Discussion

Figure 4-7 shows the fabricated comb-drive actuator. The gap between the comb-drive fingers is $10\mu m$, and the thickness of the beam spring is $20\mu m$ (figure 4-8). The gap between the fingers can be further reduced by reducing the thickness of the copper layer.

For measuring the displacement of the comb-drive actuator, a bias voltage is applied between the two sets of comb-drive fingers and the displacement is observed with an optical microscope. As the bias voltage is gradually increased, small movement in the fingers is observed. At approximately $280V$, the two sets of fingers make electrical connections, resulting in oscillation (the oscillation is observed because when the fingers make electrical contact, the electrostatic force is inactive and fingers are pulled apart by

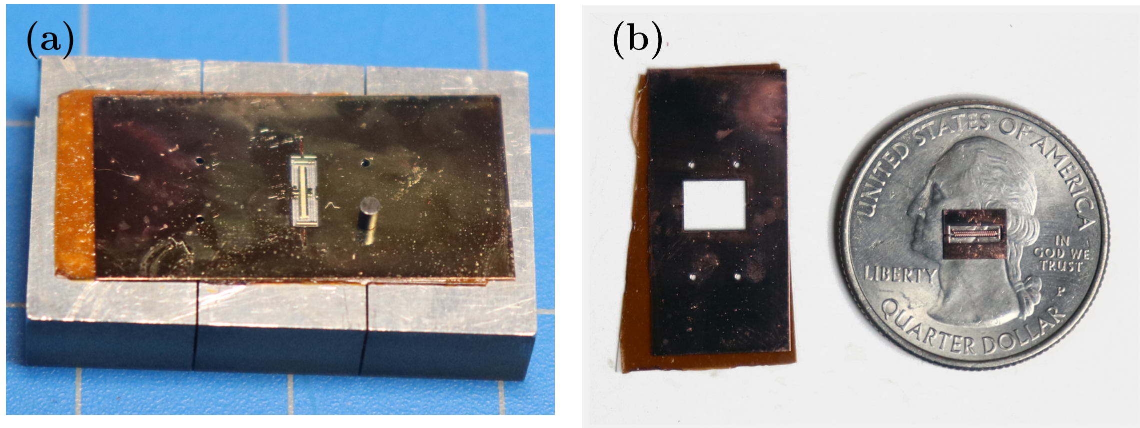

Figure 4-6: (a) Assembled and bonded layers of comb-drive actuator. (b) The device cut-out from the laminated layers using laser cutting.

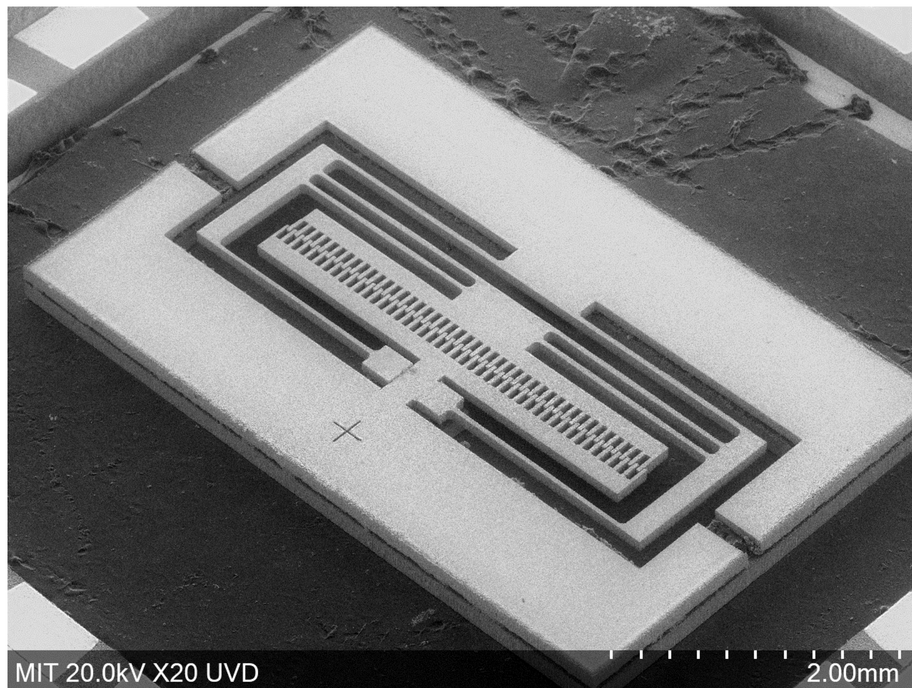

Figure 4-7: SEM image of the fabricated comb-drive actuator.

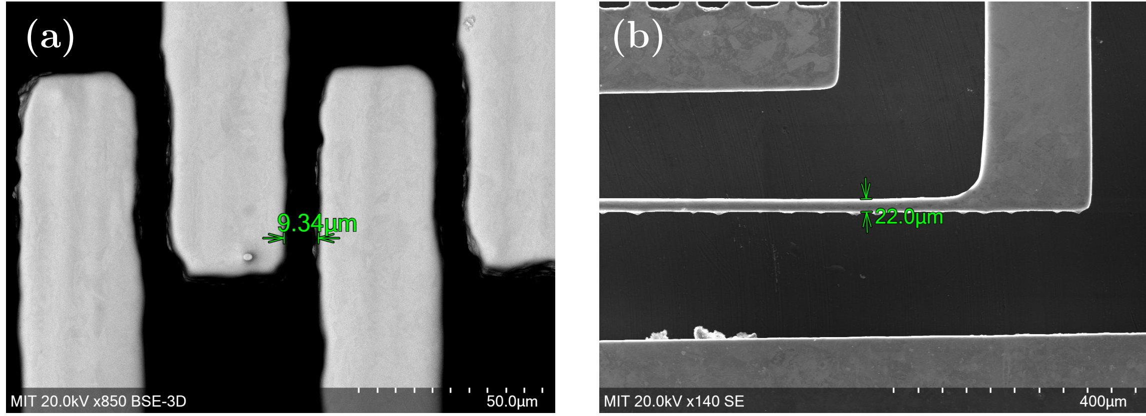

Figure 4-8: Features of the fabricated comb-drive actuator. (a) The distance between the electrostatic-comb fingers is $10\mu m$. (b) The width of the micro-beam is $20\mu m$.

the beam spring. However, immediately after the fingers are disconnected, the electrostatic force gets activated, pulling back the fingers together).

Figure 4-9(a) shows a small displacement of the comb-drive finger just before the oscillation begins, and the bias voltage is $280 \pm 10V$. As can be seen, this small distance is difficult to measure. Figure 4-9(b) shows the digitally magnified image of the fingers. The distance between the fingers is $10\mu m$ (figure 4-8), using this distance as the reference, it can be estimated that the displacement of the finger is approximately $4 - 6\mu m$. However, precise measurement inside a scanning electron microscope is required to accurately measure the displacement of fingers.

As can be seen in figure 4-8(a), the surface of the comb-drive fingers is not smooth and small protrusions, and recess exist at the surface. These protrusion and recess can increase or decrease the distance between the fingers, thereby changing the finger displacement, d. The size of these protrusion or recess are on average $1\mu m$, resulting in the error bounds in the gap, $g = 9.34 \pm 2\mu m$. This error bound in the gap results in the error bound in displacement equal to $d = 6.7 - 8.8\mu m$. These estimates are close to the measured value of $4 - 6\mu m$. The small discrepancy could be due to incorrect measurement of displacement derived from figure 4-9.

The displacement of the comb-drive fingers can be increased by increasing the length of

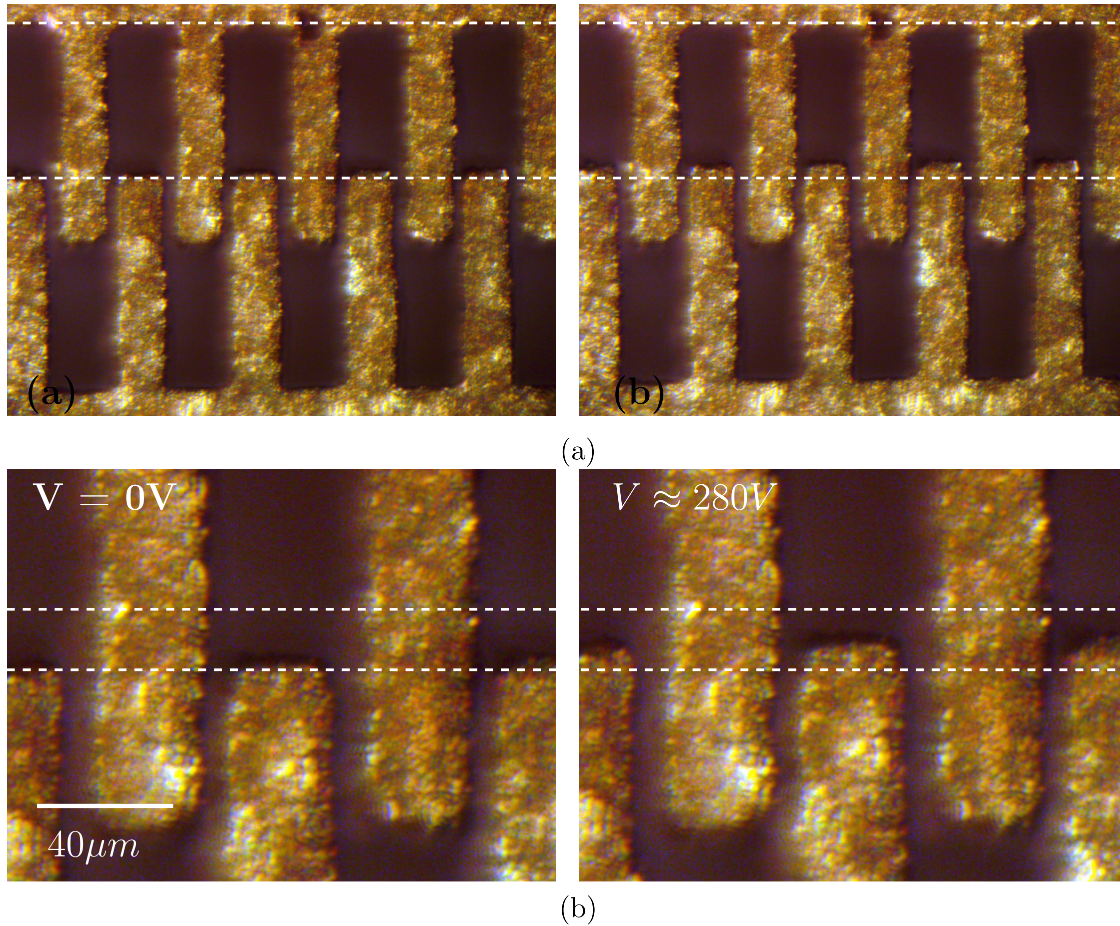

Figure 4-9: Displacement measurement of comb-drive actuator fingers. (a) Small displacement of bottom comb-drive fingers observed at $280 \pm 10V$. (b) Digitally magnified image showing the displacement of fingers. The displacement is approximately $4m - 6\mu m$

the beam springs (or reducing the spring constant). Moreover, a vapor-deposited parylene coating could be used to avoid the electrical connection between the fingers.

4.2.4 Time Required for First Prototype

The MALL MEMS fabrication process significantly shortens the time require for fabricating the first prototype. This fact is illustrated by using the example of the comb-drive actuator fabricated in this section. The first step in the concept to creation cycle is to design the device and select the desired fabrication material. Once the design and the material is finalized, the next step is to determine the laser micromachining parameters required to

micromachine the material sheet of a given thickness.

For determining process parameters, a micromachining pattern containing horizontal and vertical lines of varying width is used as a test pattern. Multiple instances of this test pattern are micromachined at various laser power, laser frequency, feed rate, and pulse duration (in this work, the pulse duration is fixed to 20 ns). These micromachined patterns are inspected in a scanning electron microscope, and the pattern with smallest feature is determined and the laser micromachining setting corresponding to this pattern is used for device micromachining. The laser micromachining process development time for a new material or sheet thickness is about 6 hours. The determined laser micromachining parameter is used fabricate the comb-drive structure. Depending upon the design, this process can take anywhere between few minutes to one hour. For this estimate, it is assumed that it will take one hour to micromachine the whole device.

The next step is to perform electro-deburring. For electro-deburring, the information about the required electrolytic solution can be derived from here [90]. The laser micromachined part is used as the anode, and another piece of same metal is used as the cathode. The information about the electropolishing voltage can also be derived from reference [90]. As discussed in section 3.5, the electro-deburring voltage must be greater than the electropolishing voltage to ensure selective etching burrs. Some degree of process development may be required for new material, but any voltage above electropolishing voltage results in electro-deburring. Often the easiest option to increase the voltage until the bubbles start to appear at the anode, and perform electro-deburring at this voltage. Generally 30 seconds are enough to completely remove the burrs. For this estimate, it is assumed that the electropolishing process will take total of one hour.

The final step is to align and laminate the individual device layer. This thesis uses Dupont FR1500 and 3M thermal bonding film 583. These adhesive films are very well studied and do not require any process development. Therefore, the bonding can be performed in a total of one hour (30 minutes of handling and 30 minutes of the adhesive curing cycle).

The total time required in fabricating the first prototype is approximately 10 hours. It

must be noted that if the fabrication material remains the same, testing new MEMS device takes approximately 4 hours.

4.3 Micro-Electromechanical Relay

4.3.1 Design

The design of the MEM relay is shown in figure 4-10(a). It consists of a movable actuator electrode anchored to the substrate with two cantilever beams. Below the actuator electrode, there are three fixed electrodes. These three electrodes are gate, input, and the output contacts (figure 4-10(b)). The square base of the actuator electrode and the square gate electrode below it form an electrostatic parallel-plate actuator. When a voltage is applied between the actuator electrode and the gate electrode, the actuator electrode is pulled-down due to electrostatic attraction.

A moving electrical contact is attached to the actuator electrode via $12\mu m$ thick dielectric layer as shown in the inset of figure 4-10. Figure 4-11 shows the bottom view of the actuator electrode and displays the movable contact as well as the dielectric layer. The dielectric layer acts as an insulator between the actuator electrode and the movable contact (figure 4-10(a)), as well as between the actuator and the gate electrode.

The movable contact, input contact, and output contact are separated by a small air gap, as shown in the inset of figure 4-10(a). The input and output contacts are fixed while the movable contact is free to move. When a voltage is applied between the actuator electrode and the gate electrode, the actuator electrode is pulled-down towards the gate. As a result, the movable contact makes an electrical connection simultaneously with input and output contacts, completing the electrical connection between the input and output electrode and turning ON the relay. When the voltage is removed, the actuator electrode returns to its original position due to the restoring force of the beam springs.

Design Parameters

Figure 4-12 shows the design parameters of the MEM relay. The length of the beam spring is $L_B = 1mm$, and the width is $W_B = 20\mu m$. The length, L_A and width, W_A of the square base of the actuator electrode is $1mm$, and width of the movable contact, W_C is $500\mu m$.

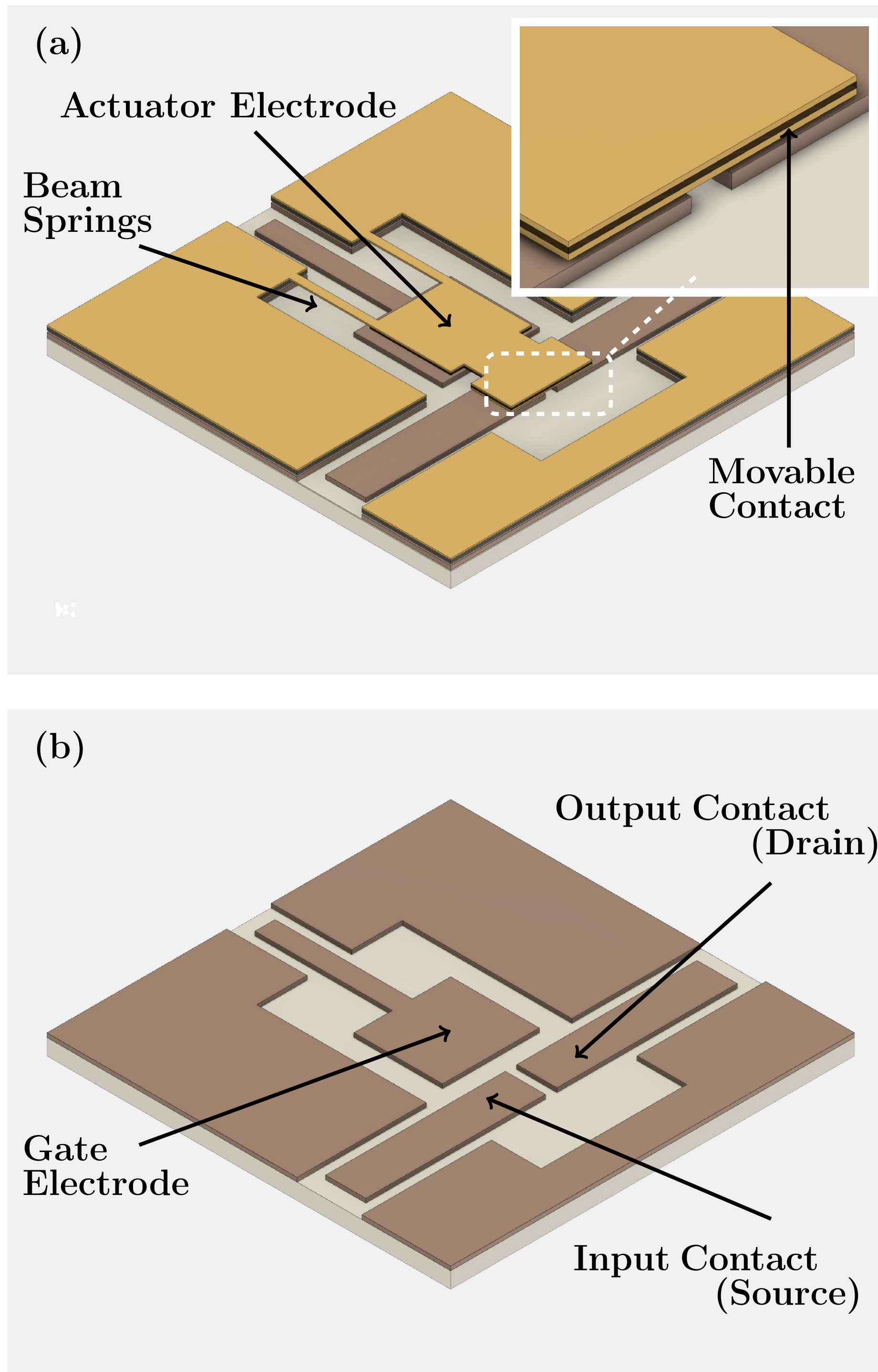

Figure 4-10: Schematic diagram of the micro-electromechanical (MEM) relay. It consists of two layers: (a) Top layer containing actuator electrode, beam springs, and movable contact (inset) (b) Bottom substrate layer containing gate, input, and output electrodes.

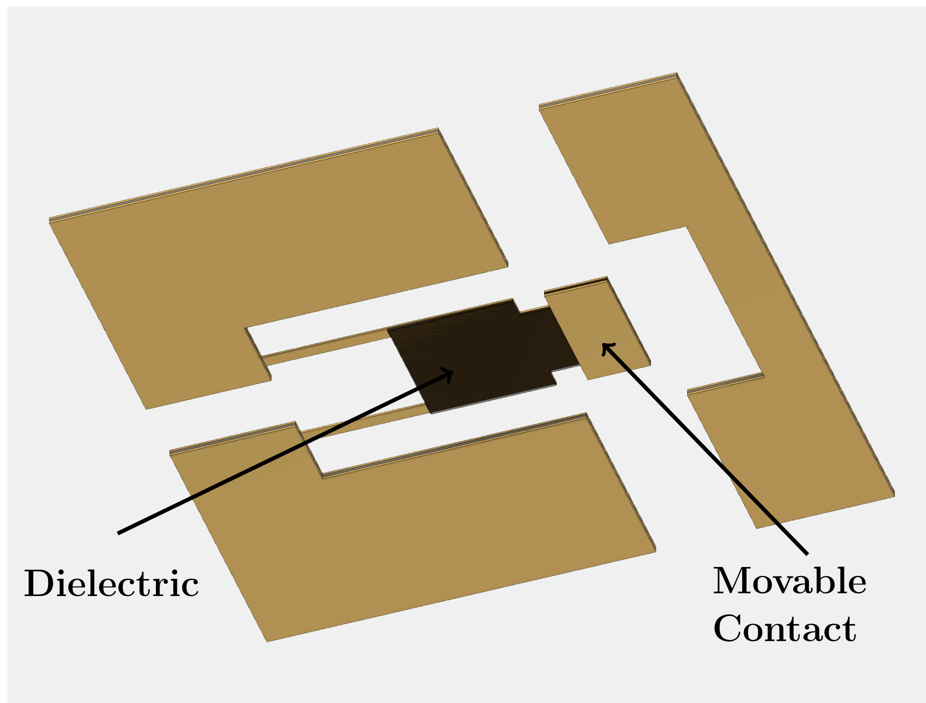

Figure 4-11: The bottom view of the actuator electrode showing movable contact and the insulating polyimide layer. The polyimide layer is used as an insulating layer between the actuator electrode and movable contact, and between the actuator electrode and the gate electrode.

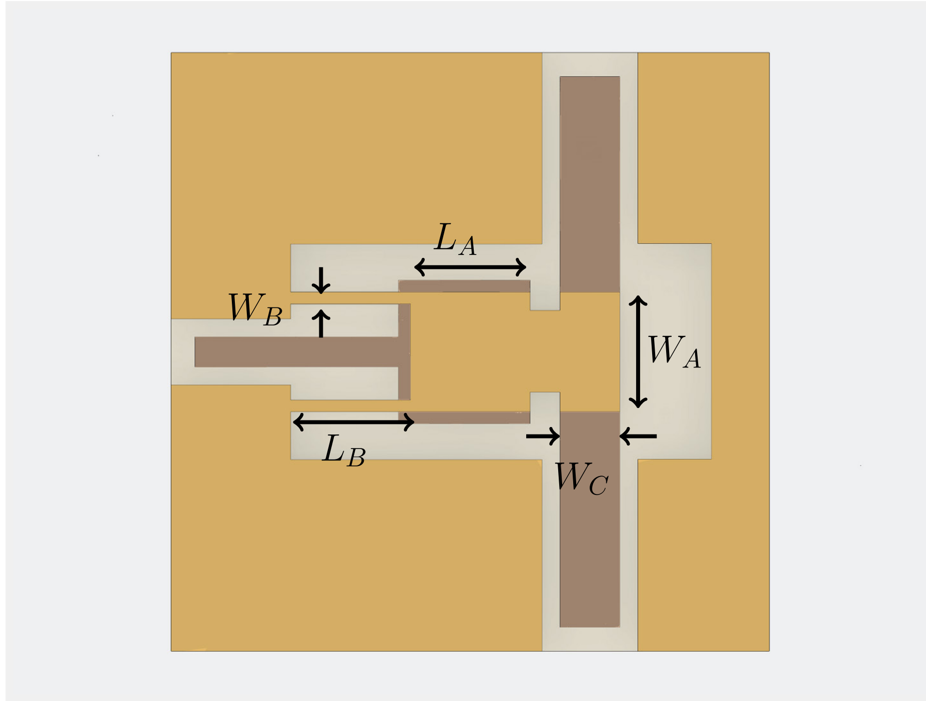

Figure 4-12: Schematic diagram showing design parameters of the the MEM relay. These parameters are listed in Table 4.2

The actuator electrode and movable contact are fabricated by LAMPE micromachining $18\mu m$ copper sheet, and the dielectric layer between the two sheets is $12\mu m$ thick polyimide. The distance between the movable contact and input/output contact is $25\mu m$. The distance between the gate electrode and actuator electrode is $55\mu m$, which is the sum of polyimide thickness ($12\mu m$), movable contact thickness ($18\mu m$), and the distance between movable contact and input/output contacts ($25\mu m$). Table 4.2 summarizes the design parameters of the MEM relay.

Analytical Model

The spring constant of a cantilever beam is given by the equation [91]:

$$k = \frac{3EI}{{L_B}^3} \tag{4.4}$$

where $I = W_B h^3/12$, h is the thickness, a is the width of the beam, l is the length of the

Design Parameters	**Value**
Young's Modulus of Copper, E	$128GPa$
Beam Length, L_B	$1000\mu m$
Beam Width, W_B	$20\mu m$
Beam Thickness, h	$18\mu m$
Actuator Length, L_A	$1000\mu m$
Actuator Width, W_A	$1000\mu m$
Gap between Actuator and Gate, d	$55\mu m$
Pull-in Voltage, V_{PI}	**256V**

Table 4.2: Values of the design parameters for MEM relay.

beam, and E is Young's modulus of the material.

For the given design, two beam springs are connected in parallel, therefore, the effective spring constant

$$k_{eff} = 2k \tag{4.5}$$

Substituting the beam spring design parameters (table 4.2) in equation 4.4 and equation 4.5, we get the effective spring constant $k_{eff} = 7.5\mu N/\mu m$.

The actuator electrode can be modeled as a parallel-plate capacitor actuator with one plate fixed while the other plate connected to a beam spring with spring constant k_{eff}. When a voltage V is applied between the two plates, the attractive force between the plates is balanced by the restoring force of the beam spring. If d is the distance between the plate at zero bias and x is the distance at bias V, then the force on the actuator plate is given by the equation [91]:

$$F_e = \frac{1}{2}\frac{\epsilon_0 A}{(d-x)^2}V^2 \tag{4.6}$$

where ϵ_0 is the permittivity of free space and A is the area of the parallel plates of the capacitor. The electrostatic force F_e is balanced by the restoring force of beam spring, and

the displacement at a particular bias voltage can be calculated by solving the equation:

$$\frac{1}{2}\frac{\epsilon A}{(d-x)^2}V^2 - xk_{eff} = 0 \tag{4.7}$$

The equation 4.7 can be used to derive the expression for pull-in voltage [91] and given by the expression:

$$V_P = \sqrt{\frac{8k_{eff}d^3}{27\epsilon_0 A}} \tag{4.8}$$

By substituting the values of design parameters for the actuator electrode from Table 4.2, we get the pull-in voltage $V_P = 204$

4.3.2 Fabrication

The MALL fabrication of the MEM relay consists of three steps. First, the fabrication of the actuator electrode, which contains one electrode of the parallel-plate actuator and movable contact. Second, fabrication of the substrate layer, which contains the gate, input, and the output electrode. Third, stack-assembly of actuator electrode and substrate layer to make the MEM relay.

The actuator electrode itself consists of three layers. The top layer is a $18\mu m$ thick copper sheet patterned to form two beam springs, an actuator-plate, and a post for movable contact. The middle layer is a $12\mu m$ thick polyimide layer and covers the actuator-plate and post for movable contact. The middle layer is used to isolate the actuator electrode from the gate electrode and movable contact.

The bottom layer is an $18\mu m$ thick copper layer consisting of a movable contact (figure 4-11). The actuator electrode is fabricated by, first laser micromachining individual layers, and then stack-assembling and bonding them. Figure 4-13 shows the fabricated actuator electrode and the inset shows (actuator electrode)-polyimide-(movable contact) laminate structure.

The substrate layer is fabricated from copper-clad printed circuit board (PCB). The

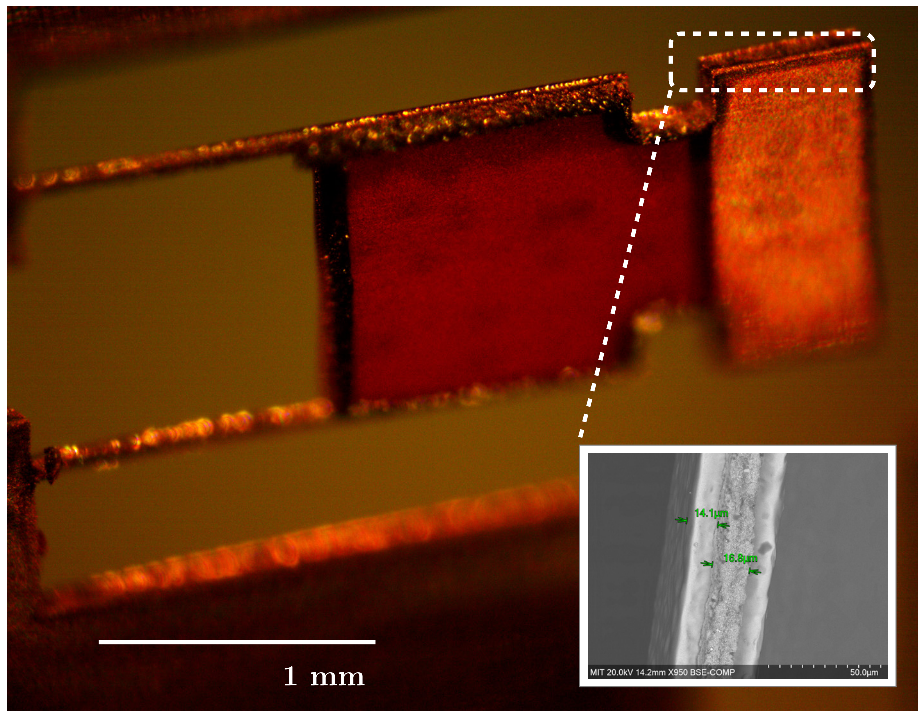

Figure 4-13: Optical microscope image of the fabricated actuator electrode showing the polyimide insulating layer and movable contact. The inset shows the copper-polyimide-copper laminate structure.

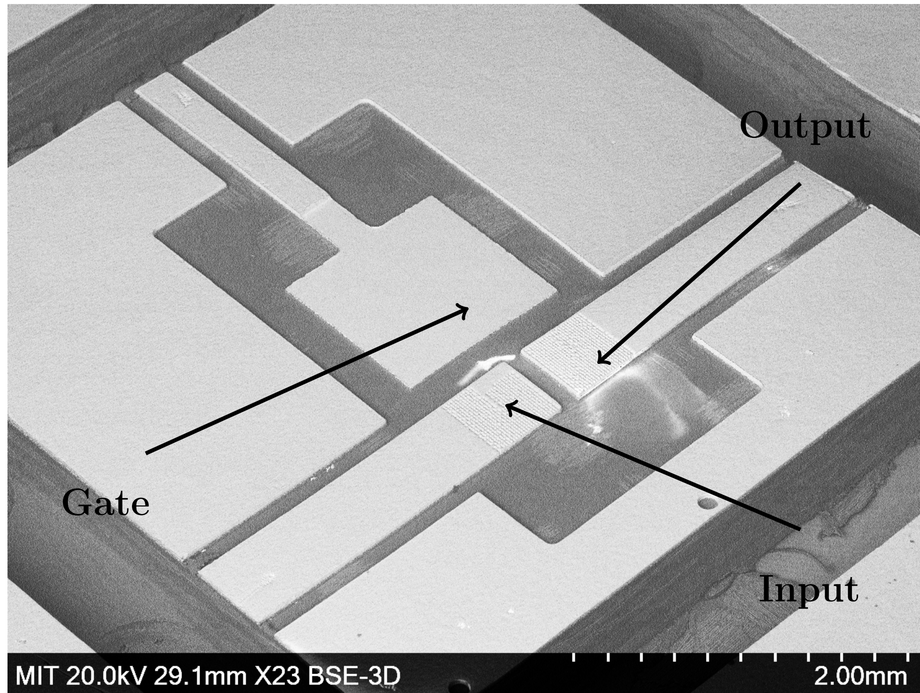

Figure 4-14: SEM image of the fabricated substrate layer showing gate, input, and output electrodes.

copper layer is $35\mu m$ thick, and the FR4 support layer is $0.7mm$ thick. The gate, input, and output electrodes are patterned by micro-milling the top copper layer using a $125\mu m$ diameter end-mill. The minimum achievable feature size is $127\mu m$, which is sufficient for this application. The micro-milling process results in micro-burrs at the edges of the electrode. These burrs are removed using the electro-deburring process described in section 3.5. Lastly, four alignment holes are drilled using $1.55mm$ drill bits. The fabricated substrate layer is shown in figure 4-14.

Finally, the actuator electrode is aligned and bonded over the substrate layer using the multi-lamina assembly process described in section 4.1. For alignment, dowel pins of diameter $1.5mm$ are used, which provides sufficient alignment accuracy required for the MEM relay. A $25\mu m$ thick adhesive layer is used to bond the two layers and create the desired gap between the movable contact and input/output contacts. Figure 4-15 shows the fabricated MEM relay. It can be seen in the inset image of figure 4-15 that the gap between the movable contact and input/output contact is $27\mu m$, which is close to the thickness of

the adhesive layer.

4.3.3 Results & Discussion

The fabricated MEM relay is tested by measuring the current between the input and output electrode (i.e., the source-drain current, I_D) at various gate voltage V_G. An HP4156 semiconductor parameter analyzer equipped with four source-measure units (SMU) is used to take the measurement. The actuator electrode is connected to electrical ground, and voltage V_G is applied to the gate electrode. For measuring the source-drain current I_D, the input electrode (source) is connected to ground, and the voltage V_{DS} is applied to the output (drain) electrode.

Figure 4-16 shows I_D vs. V_{DS} measurement at different gate voltage V_G. The V_{DS} is varied from $0V$ to $10V$, and the corresponding I_D is measured and plotted. For the gate voltage V_G less than $220V$, there is an air gap between the movable contact and input/output contact (figure 4-17(a)) and the current $I_D = 0$. When the voltage $V_G > 240V$, the movable contact makes the electrical connection with the input and output contact (figure 4-17(b)) and the current, I_D flows from input to the output electrode. The observed current saturation is due to the maximum source-current limit ($I_{max} = 100mA$) of the measuring instrument.

To observe the switching action of MEM relay, a voltage $V_G = 240V$ is manually applied, and the corresponding current I_D is measured and plotted with respect to time. Figure 4-18 shows the current vs. time plot when the relay is turned ON and OFF repeatedly. As stated earlier, the square wave nature of the current profile is due to the limit on maximum current that can be sourced from the measuring instrument.

An insulating coating between the actuator and gate electrode is essential to avoid short-circuit between the two electrodes. One of the goals of this work is to demonstrate the assembly of a MEM relay from conducting and insulating parts; as a result, a polyimide film is used as an insulating layer instead of using vapor-deposited dielectric material such as parylene.

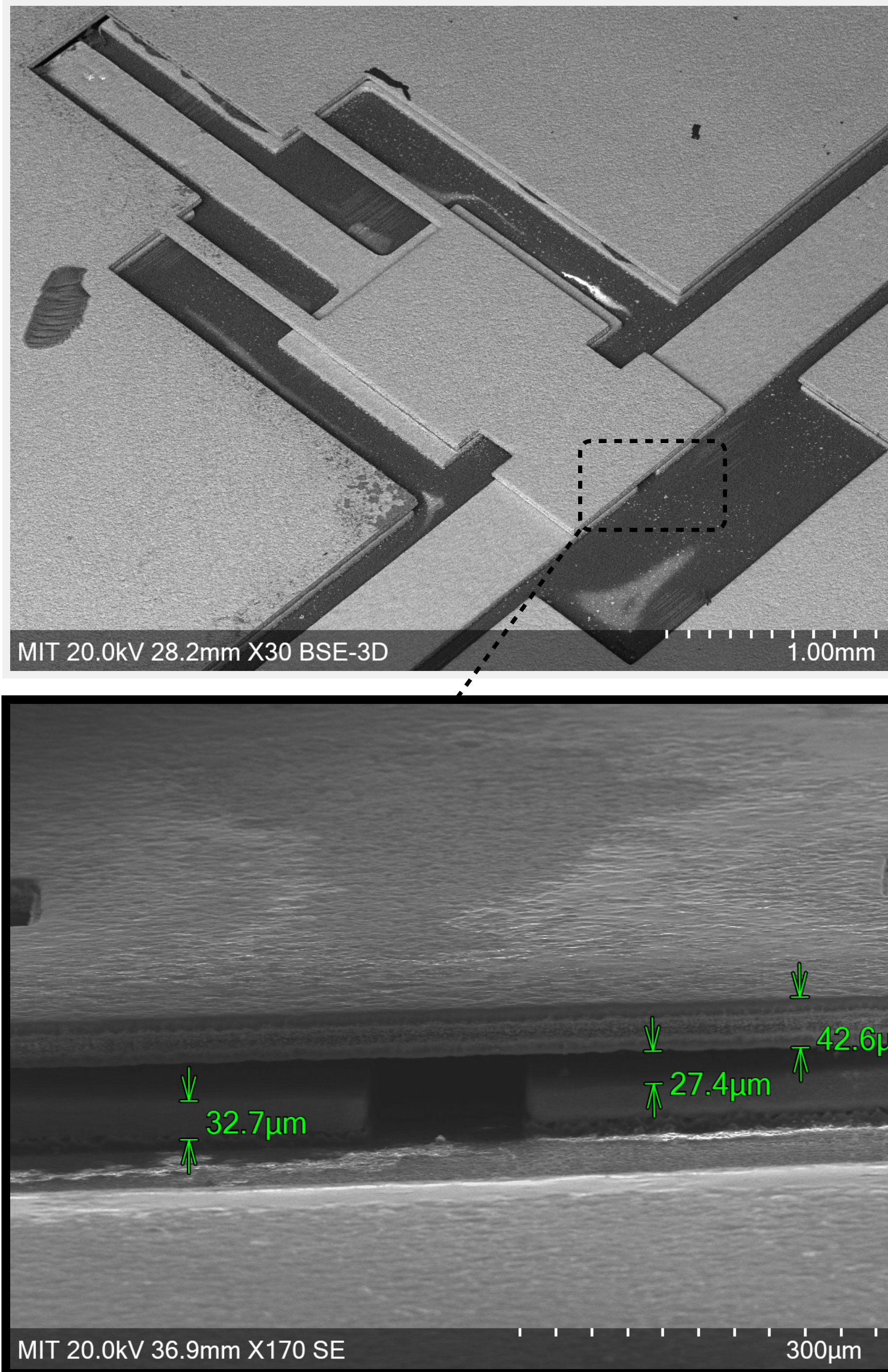

Figure 4-15: The SEM image of the assembled MEM relay. The inset shows the distance between the movable contact and input & output contacts, which is 27.4μm

.

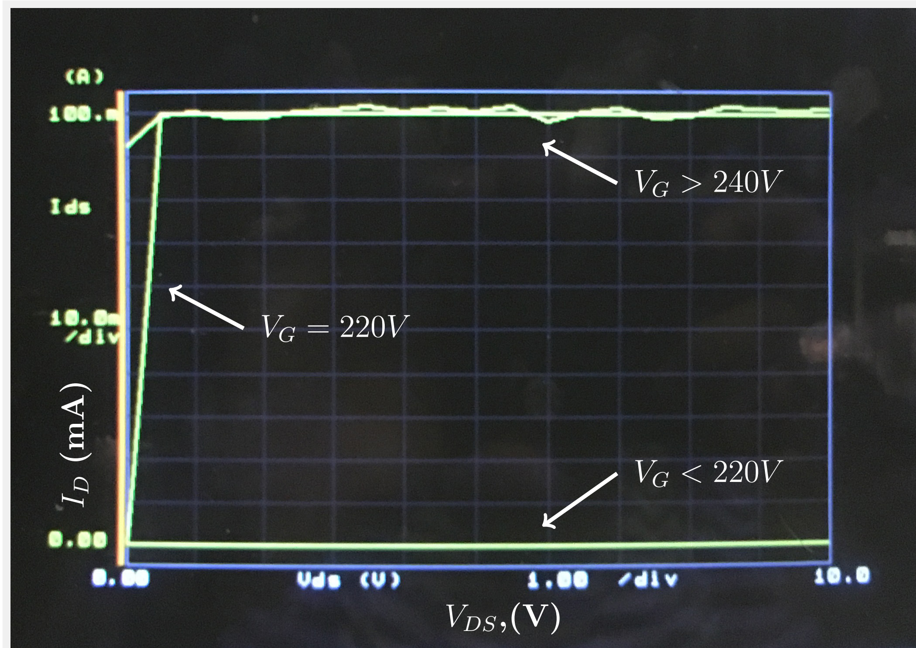

Figure 4-16: The source-drain current-voltage (I_D vs. V_{DS}) measurement at various V_G gate voltage .

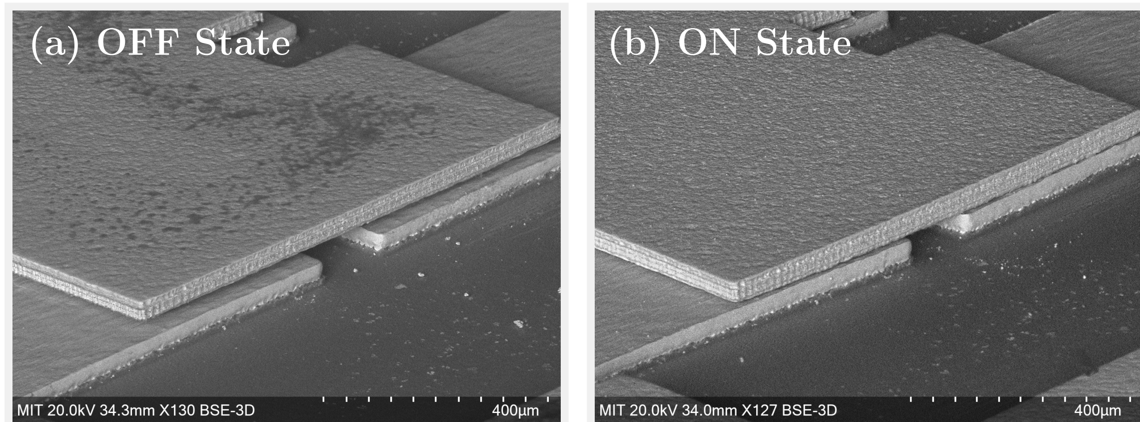

Figure 4-17: The SEM images showing the operation of MEM relay. (a) Small air-gap between the movable contact and input & output contact when the relay is off. (b) The formation of electrical contact between the movable electrode and input & output contact when the relay is turned on.

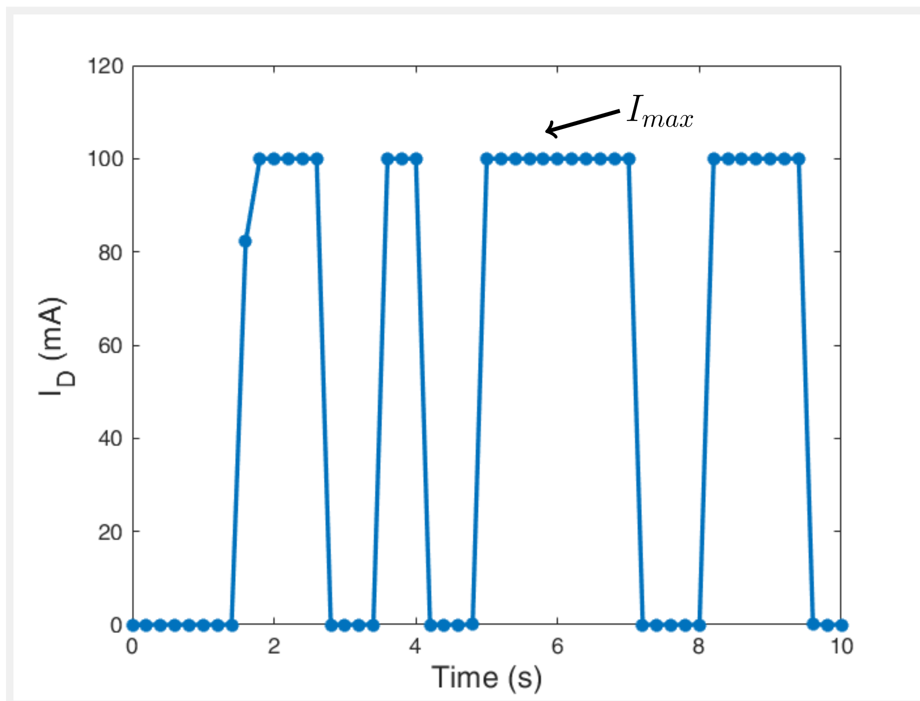

Figure 4-18: The current I_D vs. time plot of MEM relay demonstrating current switching. The current I_D is measured by applying a constant voltage $V_{GS} = 10V$ between the input and output electrode and manually cycling the gate voltage $V_G = 240V$ on and off.

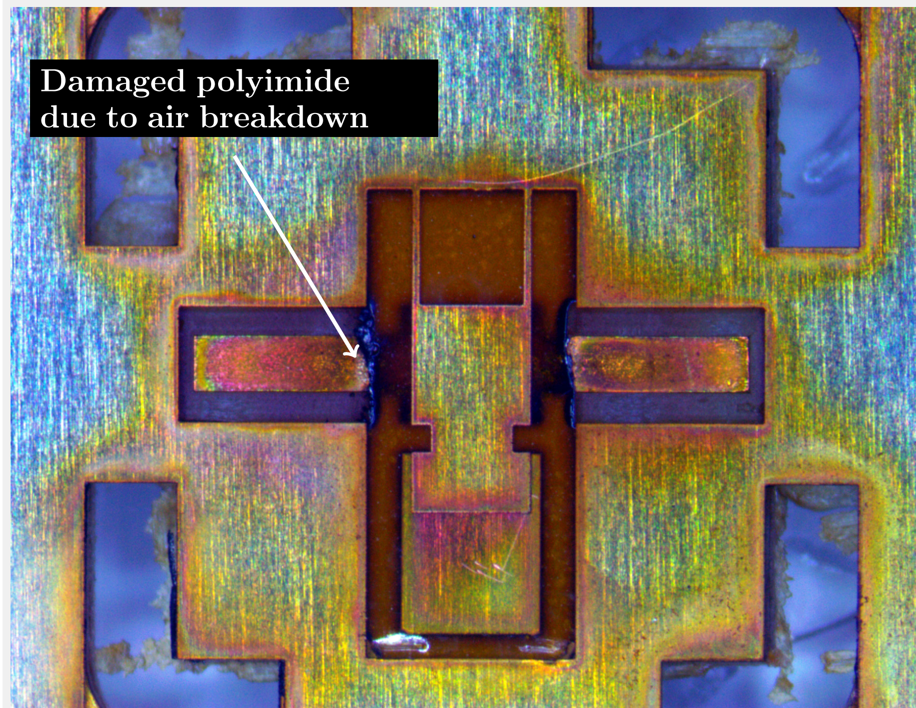

Figure 4-19: Damaged polyimide insulating layer due to the dielectric break down of air.

Unfortunately, the polyimide film results in three major complications. First, the thickness of the polyimide film adds an additional $12\mu m$ between the actuator and gate electrode, thereby increasing the pull-in voltage. Second, the polyimide film does not provide a conformal coating around the gate electrode. As a result, at high voltage, avalanche breakdown of gas molecules can occur [92][93], resulting in the destruction of the relay. This phenomenon is evident in the relay design, where the polyimide film is attached to the gate electrode, as shown in figure 4-19. As can be seen, the polyimide layer is burned due to the dielectric breakdown of air.

Third, the polyimide layer used in MEM relay fabrication causes stiction of the actuator electrode with the gate electrode. The stiction problem in MEM systems is widely known [94] and can be minimized by applying an anti-stiction coating [95][96]. In summary, using a vapor-deposited dielectric coating such as parylene coating can drastically improve the performance of MEM relay by reducing the pull-in voltage, increasing the maximum safe operating voltage, and minimizing stiction.

4.4 Diamond Rotor

4.4.1 Introduction

Amyloid fibrils are self-assembled filamentous structures associated with more than fifty diseases, including Alzheimer's and Parkinson's [97]. Determination of the atomic-resolution 3D structure of amyloid fibrils is essential to develop a cure for these diseases [98]. However, obtaining atomic-resolution structural information using classical methods such as electron microscopy, atomic force microscopy, x-ray crystallography, and solution-state NMR spectroscopy is challenging as amyloid fibrils are inherently noncrystalline, insoluble and lack 3D order.

Recent advances in magic angle spinning (MAS) [99][100] solid-state NMR spectroscopy has enabled determination of the 3D structure of amyloid fibrils [101][102]. In MAS, a sample is rotated around an axis tilted at 57.74° with respect to the static magnetic field, resulting in the averaging of anisotropy of nuclear interaction, which increases the resolution of NMR spectroscopy. The resolution of MAS NMR increases with increasing spinning frequency [103]. Unfortunately, the spinning frequency of state-of-the-art MAS probes or rotors is limited to $110KHz - 140KHz$ [104] [105]; as a result, the resolution of MAS NMR is limited.

The maximum spinning frequency of MAS rotors depends upon the fluidic properties of surrounding gas, and the speed at the circumference of the rotor must be less than the speed of sound in this gas [106][107][108]. Figure 4-20 shows the calculated maximum theoretical limit of MAS frequency of rotors with various diameters currently employed in MAS NMR. The theoretical limit is calculated using the value of the speed of sound in helium at various temperatures [109]. As can be seen, the theoretical limit on the maximum frequency increases with decreasing the diameter of the rotor. For the $0.7mm$ MAS rotor, smallest diameter rotor currently employed, the maximum theoretical limit on spinning frequency is $454.7KHz$. However, in practice, the spinning frequency is limited by the tensile strength of the zirconia material used for fabricating rotors. The maximum spinning

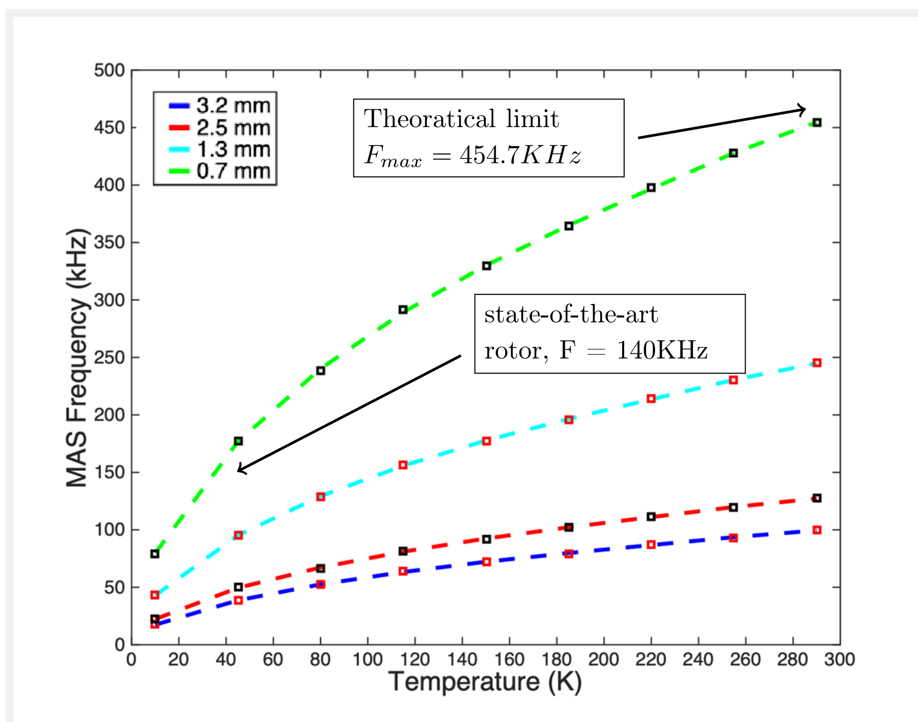

Figure 4-20: Maximum theoretical MAS frequency for various diameter rotors. As can be seen, the 0.7mm diameter rotors have the highest MAS spinning frequency.

frequency of state-of-the-art zirconia ($ZrO2$) rotor is approximately 126KHz [104][105] (figure 4-20).

4.4.2 Diamond Rotor

Diamond is the hardest material, and the tensile strength as high as 5190MPa has been reported for chemical vapor deposition (CVD) grown diamonds [110]. As a result, diamond is an excellent choice for making MAS rotors and expected to spin at a higher frequency than state-of-the-art zirconia rotors. Moreover, diamond is transparent to microwaves; as a result, ideal for dynamic nuclear polarization (DNP) experiments, which is used in conjunction with NMR. However, machining diamond is difficult because of its hardness. Although laser cutting is employed to cut diamond sheets, the process does not produce the desired aspect-ratio required for fabricating a diamond rotor. This thesis shows high aspect ratio laser micromachining of diamond and its application in making the diamond rotor for MAS NMR.

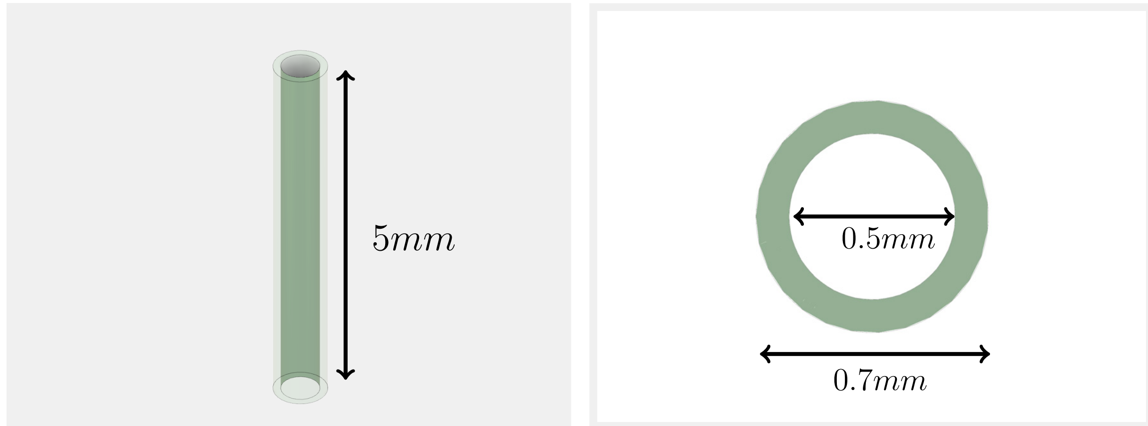

Figure 4-21: Schematic diagram showing the dimensions of the MAS diamond rotor probe.

The employed laser micromachining method is an extension of LAMPE micromachining discussed in chapter 3 and discussed next.

4.4.3 Laser Micromachining of Diamond

Figure 4-21 shows the schematic diagram of the diamond rotor. The inner diameter of the rotor is $500\mu m$, and the outer diameter is $700\mu m$. The total length of the rotor is $5mm$.

The chemical vapor deposition (CVD) grown diamond sheets are obtained from Element Six (www.e6.com). The sheet is cut into small square logs of dimension $1mm \times 1mm \times 5mm$, and the rotors are fabricated by machining these logs. For laser micromachining, the log is mounted vertically, and the laser micromachining is performed from one end to the other. The focus is gradually moved until the complete hole is drilled. Figure 4-22 shows the micromachined inner diameter and the outer diameter of the diamond rotor.

4.4.4 Theoretical Explanation

The high aspect ratio depends upon the optical penetration depth. The optical penetration depth of the CVD diamond is measured using transmission spectroscopy and described next.

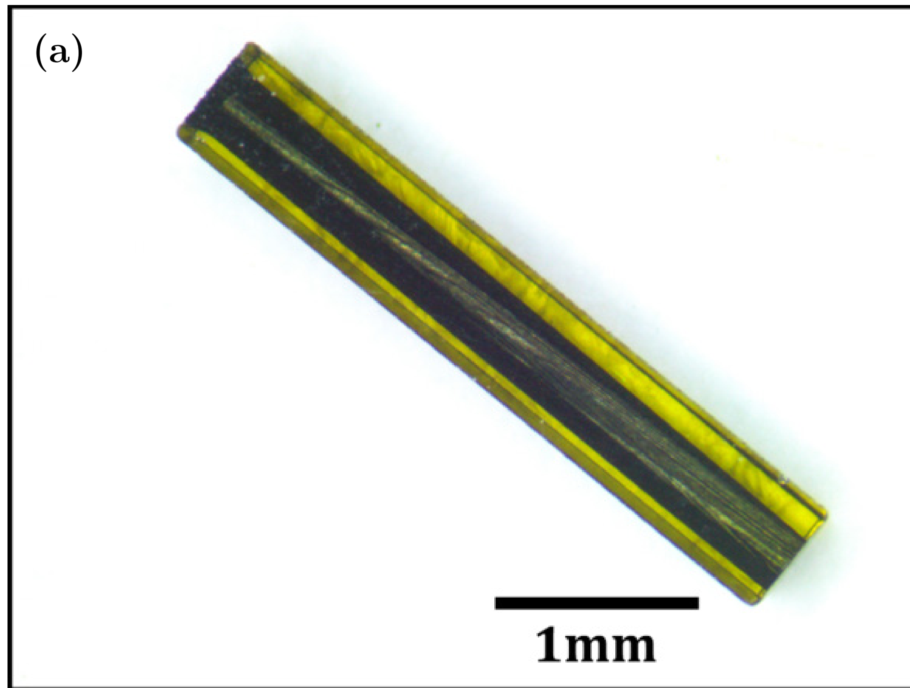

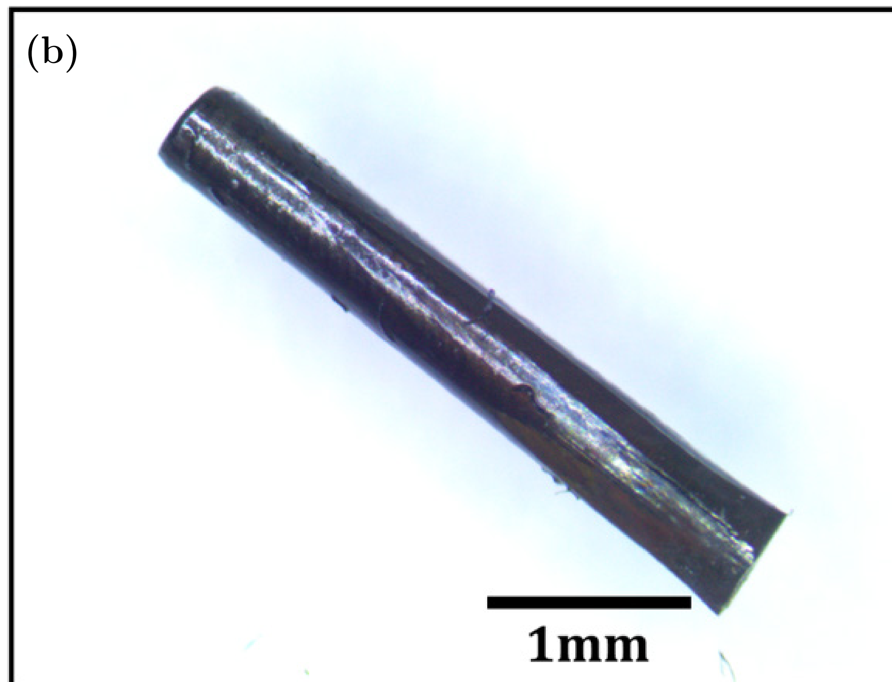

Figure 4-22: Laser micromachining of diamond rotor (a) Inner diameter. (b) Outer diameter.

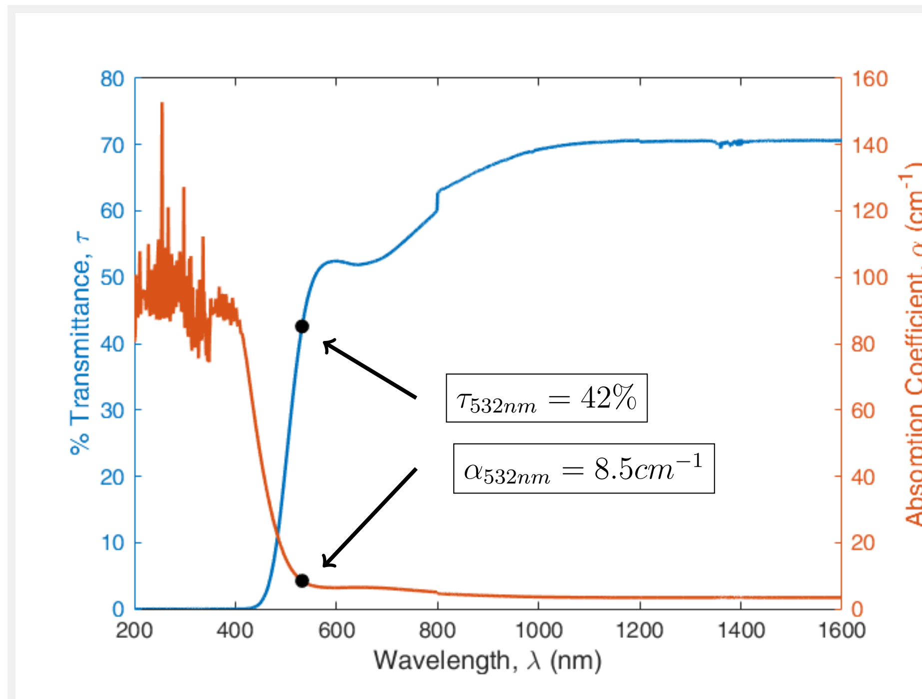

Figure 4-23: The transmittance and absorption coefficient of CVD diamond. At $532nm$ the transmittance, $\tau = 42\%$ and the absorption coefficient $\alpha = 8.5cm^{-1}$

Optical Penetration Depth

The absorption coefficient α is calculated from the transmission spectrum. Figure 4-23 shows the transmittance spectra and the absorption coefficient plot of the CVD diamond. The transmittance $\tau = 42\%$ and absorption coefficient $\alpha = 8.5cm^{-1}$ at $532nm$.

Figure 4-24 shows the variation of optical penetration depth, $l_\alpha = 1/\alpha$, with respect to the wavelength. As can be seen, at $532nm$, the absorption is sufficiently low to allow large optical penetration depth but large enough to cause laser absorption and heating. Once the laser is absorbed by the diamond, it causes a phase change resulting in graphitization of the diamond [111] [112]. The absorption coefficient of graphite is much larger than the CVD diamond, resulting in a sudden increase in the laser absorption and increase in temperature. Finally, the graphite is oxidized into CO_2 in the presence of atmospheric oxygen. Although this work uses $532nm$ wavelength for diamond micromachining, the author recommends using wavelength around $1028nm$ to take advantage of a further

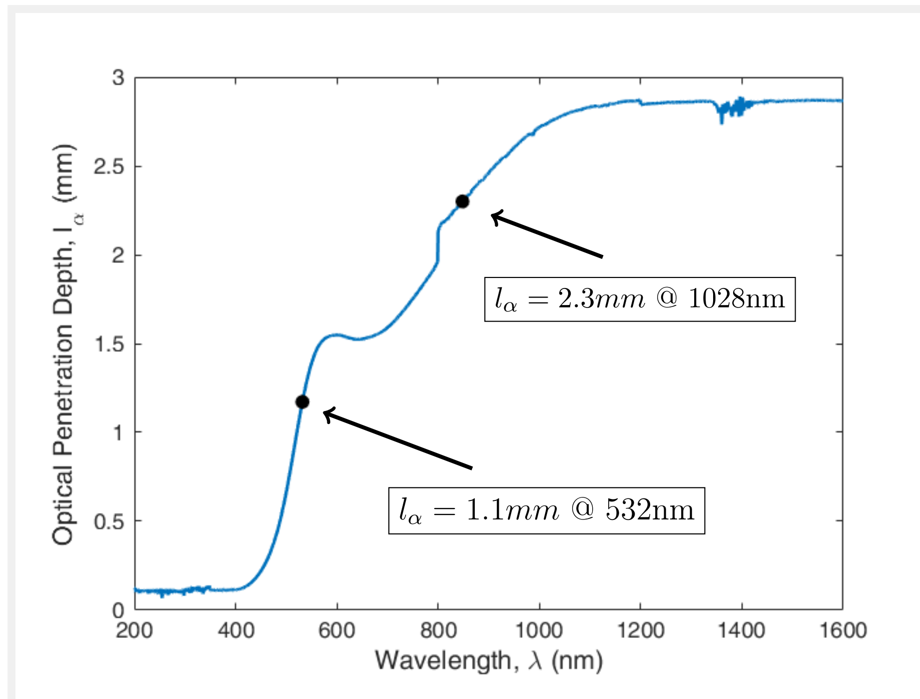

Figure 4-24: The optical penetration depth of CVD diamond at $532nm$ is $1.1mm$.

increase in optical penetration depth while still maintaining sufficient absorption (figure 4-24).

4.5 Conclusions

In conclusion, the MALL process can be used to manufacture functional MEMS devices using metals. These MEMS devices have lateral features and aspect ratio comparable to devices fabricated using DRIE. Moreover, using MALL, MEMS devices can be rapidly developed and fabricated at low cost.

In DRIE, process development is required for fabricating a new MEMS. The process parameters are optimized by performing a series of etch cycle and varying the etching parameters. Each etch cycle requires the loading and unloading of the wafer, and often the process is done manually. As a result, DRIE process development takes substantial time. However, in the MALL process, various parameters such as laser power, pulse frequency,

feed rate, and pulse duration can be tested in a single cycle, thereby considerably shortening the process development time.

In DRIE, the etch rate depends upon the device area due to the loading effect [113][72]. As a result, for each MEMS design, a new set of DRIE process parameters must be determined, which significantly hinders design iteration and increases device development time. However, in the MALL process, the laser micromachining rate is independent of the device area (or design); as a result, many MEMS designs can be tested without requiring any process development.

Chapter 5

Discussion & Conclusion

5.1 Advantages of MALL

The MALL fabrication process offers several advantages over conventional lithography-based MEMS fabrication processes such as greater material selection and integration, low cost of fabrication, rapid development, and integrated packaging. These advantages are discussed in detail in the following sections.

5.1.1 Greater Choice of Fabrication Materials

The fabrication materials used in the lithography-based MEMS manufacturing process is largely limited to silicon. On the other hand, the MALL process enables fabrication with a wide range of materials such as metals, ceramics, polymers, and composite materials. The ability to fabricate MEMS using a wide range of materials greatly enhances the functionality and performance of these systems. For example, materials with interesting properties such as magnetic, piezoelectric, pyroelectric, thermoelectric, and superconducting materials can be employed to design novel MEM systems.

The application of metals in fabricating MEM systems is especially of great interest. Metals offer a wide range of mechanical and electrical properties, and these properties can be tuned using the alloying process. Moreover, due to the roll forming process, the cost and

energy requirement for making metal foils is much less than that of silicon wafers.

5.1.2 Fabrication with Incompatible Materials

In conventional microfabrication process, MEMS are fabricated layer-by-layer by successive deposition and patterning of material layers. Each material layer is deposited and patterned using a unique process, and this process must be compatible with the previously deposited materials. The integration of these processes is often difficult due to material incompatibilities and thermal constraints. However, in the MALL fabrication process, the individual layers of MEMS are fabricated separately, and stack-assembled and bonded to make a system. As a result, materials with incompatible fabrication process can be bonded together, in any order, to manufacture MEMS.

5.1.3 Low-Cost Fabrication

The high cost of MEMS fabrication is due to two reasons. First, the large capital investment in microfabrication tools such as exposure system, mask aligners, chemical vapor deposition (CVD), and deep reactive ion etching (DRIE) systems. Second, the high cost of raw materials and chemicals such as photoresists, developers, etching solutions and gases, and silicon wafers. In contrast, the MALL process requires a laser micromachining system and electrochemical etching tools, which have a much low cost of ownership than the traditional microfabrication tools. Similarly, the raw materials used in MALL fabrication are metal foils, polymers, and ceramics. These materials are much more cost-effective than silicon wafers, utilized in conventional MEMS fabrication process.

The DRIE can produce multiple parts in parallel; as a result, after the initial investment, equipment cost shared per device is significantly reduced. In fact, the DRIE equipment cost per device for fabricating the comb-drive mentioned in section 4.2 is approximately \$0.09 (detailed calculations for cost estimates are presented in appendix A.1). However, the material cost per device in DRIE remains substantial. For the comb-drive actuator, the material cost per device is \$0.51 (Appendix A.1), which is about 85% of the total device

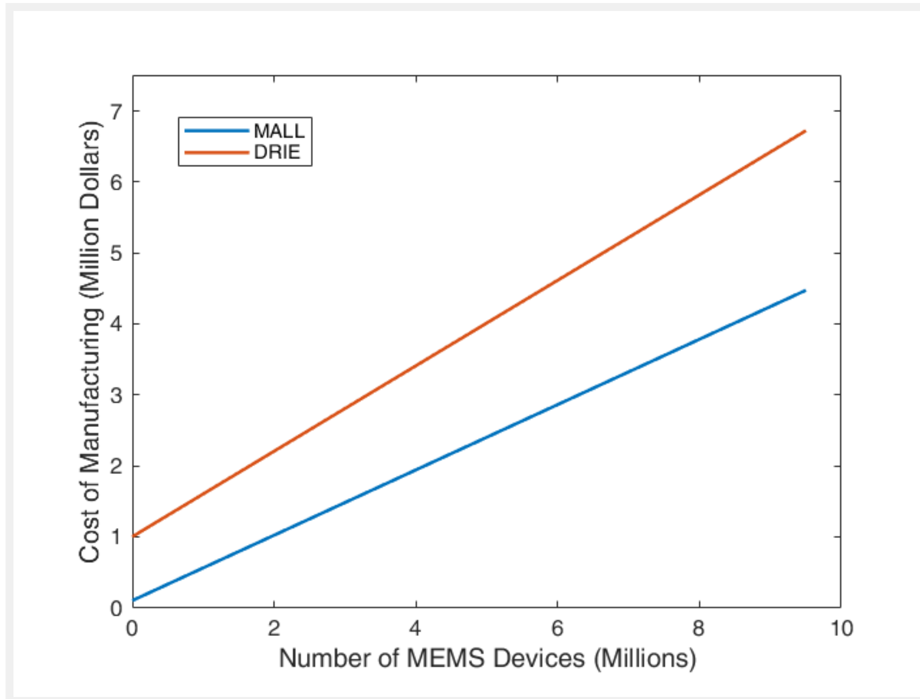

Figure 5-1: Cost of fabricating the comb-drive actuator using DRIE and MALL process.

cost.

In the MALL fabrication process, even though the initial cost of a laser micromachining system is low, the equipment cost per device is significantly high due to the low part production rate. For the comb-drive actuator discussed in section 4.2, the equipment cost per device is \$0.46 (appendix A.1). However, the material cost per device is significantly low, about \$0.0015 per device (appendix A.1). As a result, the total cost per device for both DRIE and MALL is comparable. Table 5.1 summarizes the manufacturing time and cost associated with fabricating the comb-drive actuator using DRIE and MALL process.

Although the cost per device for both the processes is comparable, the manufacturing cost for MALL is less due to low initial capital investment. Figure 5-1 compares the manufacturing cost of DRIE and MALL process. As can be seen, for a given number of fabricated MEMS, the corresponding manufacturing cost using the MALL process is $\$0.9M$ less than the cost associated with DRIE.

In MALL process, individual layers are fabricated using LAMPE micromachining, and

Parameter (per device)	**DRIE**	**MALL**
Manufacturing time	$0.2min$	$12min$
Equipment cost	\$0.09	\$0.46
Material cost	\$0.51	\$0.0015
Total manufacturing cost	\$0.51	\$0.4615

Table 5.1: Time and cost of fabricating the comb-drive actuator using DRIE and MALL fabrication process. The detailed calculations for cost estimations are presented in appendix A.1

Parameter (per device)	**DRIE**	**MALL**
Manufacturing time	4.8 seconds	30 seconds
Equipment cost	\$0.03	\$0.02
Material cost	\$0.61	\$0.0015
Total manufacturing cost	\$0.64	\$0.0215

Table 5.2: Time and cost of fabricating MEM relay using DRIE and MALL fabrication process.

the rate of machining increases with a reduction in the sheet thickness. As a result, the MALL process is especially advantageous for MEMS using thin laminates such as the relay discussed in section 4.3. The thin laminate for MEM relay is fabricated by removing the excess material using LAMPE micromachining. The boundary of the excess region is $60mm$ long, and the feed rate of $120mm/min$ is used for micromachining. As a result, one relay can be fabricated in 30 seconds. The cost of a laser micromachining system is \$100,000, and assuming the lifespan of 5 years, the cost per device comes out to be \$0.02 (including the material cost).

Fabricating the same MEM relay using DRIE costs \$0.64 per device, 95% of which comes from material cost. The cost of one wafer is \$220 [114], and each wafer can accommodate 360 devices; therefore, the material cost per device is \$0.61. The remaining \$0.03 comes from equipment cost per device. Table 5.2 summarizes the cost per device for MEM relay using DRIE and MALL, and figure 5-2 compares the manufacturing cost for these processes.

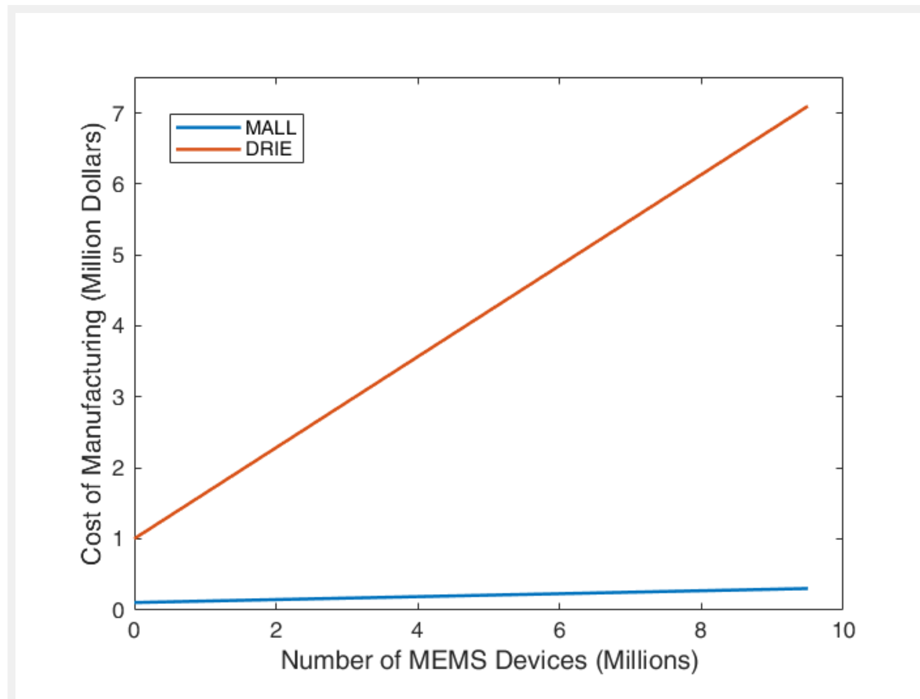

Figure 5-2: Cost of fabricating MEM relay using DRIE and MALL process.

5.1.4 Rapid Development

Rapid Material Integration

In a conventional lithography-based fabrication process, MEM systems are fabricated layer-by-layer. Fabricating each layer involves a series deposition and patterning steps such as chemical vapor deposition (CVD), spin-coating photoresist, resist exposure and development, and wet or dry etching. The fabrication process for each layer must be optimized and should be compatible with the previously deposited materials. This step-by-step process optimization and integration is extremely time-consuming. Moreover, in conventional MEMS fabrication, MEM chips and packages are fabricated separately and integrated at a later stage. This integration of chips and packages further increases the development time.

In the MALL fabrication process, individual layers can be manufactured independently with minimal process development and effortlessly bonded to make MEM systems; as a

result, significantly reducing the device development time. Moreover, laser micromachining system used in MALL can exist side by side with other macro-fabrication equipment (such as milling, molding, and embossing), and utilizes similar computer-aided design (CAD) and computer aided manufacturing (CAM) tools, thereby enabling integrated design of MEMS and packaging, simultaneous fabrication, and rapid integration.

In conventional MEMS fabrication, the three-dimensional MEMS design is converted into a series of two-dimensional lithography masks, which are subsequently used for fabrication. However, in MALL, the laser micromachining toolpath can be directly exported from the integrated CAD/CAM design tool. This integration of design, manufacturing, and finite element analysis (FEA) of MEMS in one environment enables the rapid iteration of design, simulation, and prototyping.

Rapid Process Development

In DRIE, some degree of process development is required to etch the desired MEMS structure. The etching process parameters are determined by performing a series of etch cycles and varying the etching parameters. Each etch cycle requires the loading and unloading of wafer, and often the process is done manually. As a result, the process development take substantial time.

However, in the MALL process, various laser micromachining parameters such as laser power, pulse frequency, feed rate, and pulse duration can be tested in a single cycle by performing a series of micromachining tests. As a result, considerably shortening the process development time. The laser micromachining process development time for new material or new sheet thickness is about 6 hours.

Rapid Design Iteration

In MALL, the micromachining rate of PLA or LAMPE micromachining is independent of the device area (or design). As a result, many designs can be tested without requiring any process development. However, in DRIE, the etch rate depends upon the device area due to

the loading effect [113][72]. As a result, for each MEMS design, a new set of DRIE process parameters must be determined, which significantly hinders design iteration and increases device development time.

5.1.5 Integrated Packaging

The packaging of MEMS is essential for protecting the system from a harsh environment. Moreover, in certain MEM systems, the packaging also acts as an interface between the MEMS system and the external environment. The microfabrication processes used to fabricate MEMS chips are incompatible with the macro-fabrication processes that are used to fabricate MEMS packages. As a result, the MEMS die, and the package are fabricated independently and then integrated later. This integration process is challenging and increases development time and cost. Often, the cost of MEMS packaging is higher than the cost of fabricating MEMS chips.

In MALL, the fabrication process and materials are compatible with the macro-fabrication processes. As a result, the MEMS layers and the packaging layers can be fabricated simultaneously. Moreover, these layers can be laminated in a single step, thereby enabling the fabrication of MEM systems with integrated packaging. However, the lamination process uses polymer adhesive films for bonding the packaging layers. These polymer films are permeable to water molecules [115][116]. Thus, the MALL integrated packaging can not be used for package MEMS requiring a hermetic seal.

5.2 Limitations of MALL

5.2.1 Inadequate for Fabricating 2.5D Structures

The conventional microfabrication utilizes deep reactive ion etching (DRIE) and anisotropic wet etching processes [82][117] to fabricate MEMS structures. These processes allow control over etch depth, and therefore, enable the fabrication of two-and-a-half dimension (2.5D) structures. However, the LAMPE micromachining process developed in

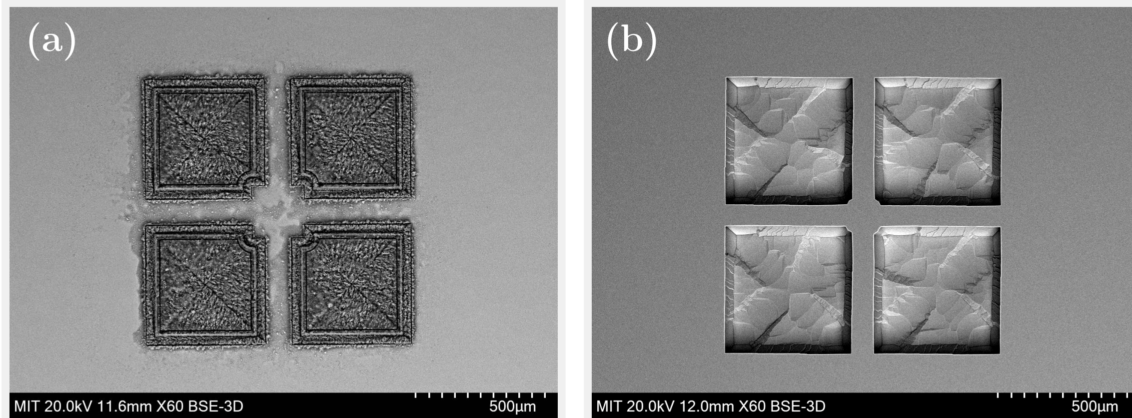

Figure 5-3: Fabrication of 2.5D structure in silicon using laser-micromachining: (a) Silicon nitride mask layer patterned using laser-micromachining. (b) KOH anisotropic etch to fabricate 2.5D structures.

this thesis is restricted to micromachining laminates.

One approach to overcome this limitation is to use $2.5D$ structures fabricated in polymers using the conventional pulsed ablation laser-micromachining process. Another approach is to integrate the laser-micromachining with silicon anisotropic etching process. In this approach, first, a silicon nitride mask layer is removed using laser-micromachining (figure 5-3(a)), and then, potassium hydroxide etching [2] is performed to create $2.5D$ structures (figure 5-3(b)). The third approach is to use micro-milling followed by the electro-deburring process (section 3.5) to create $2.5D$ structures. The micro-milling offers vertical features as small as $5\mu m$. However, the minimum achievable feature in the lateral direction is limited to $50\mu m$. figure 5-4(b) shows micro-milling $2.5D$ recess with a varying depth.

5.2.2 Limit on Minimum Thickness of Microstructures

The conventional microfabrication process utilizes surface micromachining [48][49][50] to fabricate thin free-standing microstructures. Figure 1-5 shows the schematic diagram of the surface micromachining process. First, a sacrificial layer is deposited on a substrate and patterned using photolithography and etching. Next, the structural layer is deposited and patterned on top of the sacrificial layer. Finally, the sacrificial layer is removed to create free-standing microstructures. The deposition process, such as chemical vapor deposition

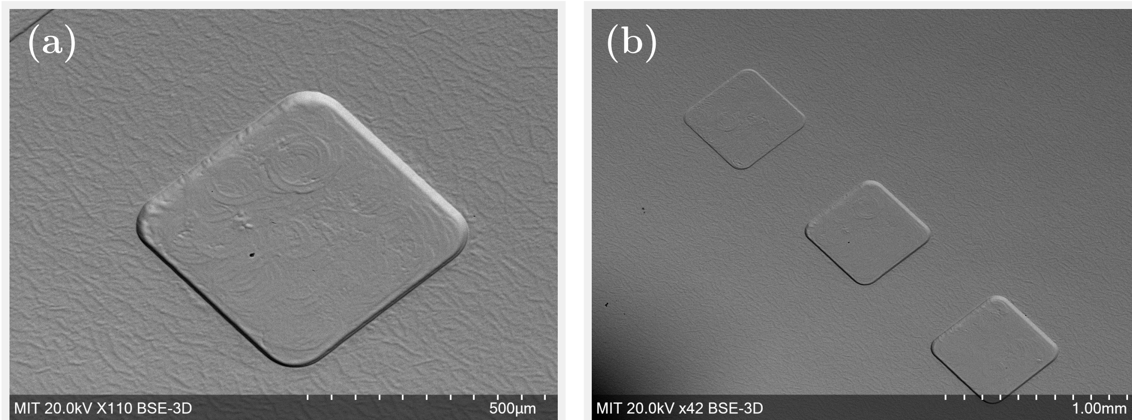

Figure 5-4: Fabrication of 2.5D structures using micro-milling. (a) Square recess fabricated using micro-milling followed by electro-deburring. Feature size as small as $100\mu m$ can be fabricated using this method. (b) The micro-milling method provides a high degree of control over the recess depth. The figure shows fabricated recess with depth $5\mu m$, $10\mu m$, and $15\mu m$.

(CVD) used to deposit the sacrificial layer or structural layer, allows a high degree of control over the thickness of the deposited material. As a result, free-standing structures with a small thickness (tens of nanometers) can be fabricated (such structures are desirable for applications such as high-speed resonators [24][118]).

However, in the MALL process, MEMS structures are fabricated with thin sheets of materials and manually assembled or roll-to-roll laminated. There is a practical limit on the thickness of sheets that can be manually handled or laminated using the roll-to-roll process. Typically, foils with thickness greater than or equal to $20\mu m$ can be used for manual assembly and roll-to-roll lamination process. As the thickness of the laminate is reduced, handling of these ultra-thin laminates becomes difficult. For a MEM device requiring sheets with a thickness between $20\mu m$ to $5\mu m$, a rigid or flexible frame can be utilized. Figure 5-5 shows a $10\mu m$ thin microstructure supported by a frame. For fabricating this structure, first, a window is micromachined in $200\mu m$ thick silicon substrate. Next, a $10\mu m$ thick silver foil is bonded to the silicon substrate. Finally, the device structure is laser micromachined on the bonded silver foil. For MEM systems requiring metal foils with thickness in the order of $5\mu m$ to $1\mu m$, the desired metal can be electrodeposited over water or solvent-soluble films, and such laminates can be used to fabricate MEMS.

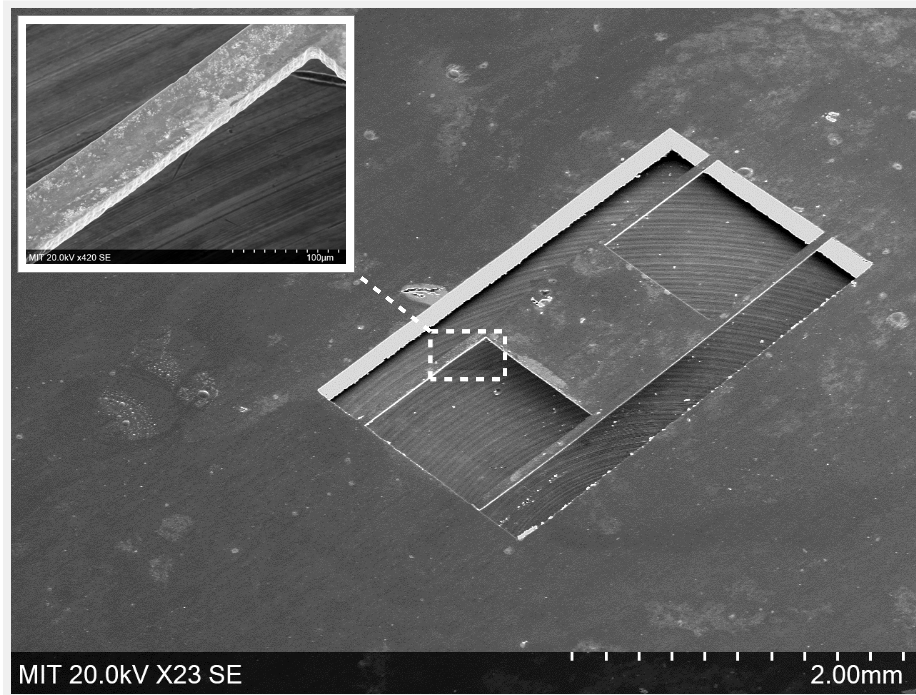

Figure 5-5: Manipulation and laser micromachining of ultra-thin metal foils using a rigid frame. First, a window is micromachined in the rigid frame. Next, a $10\mu m$ thin metal foil is laminated on this frame. Finally, laser micromachining is performed to create microstructure.

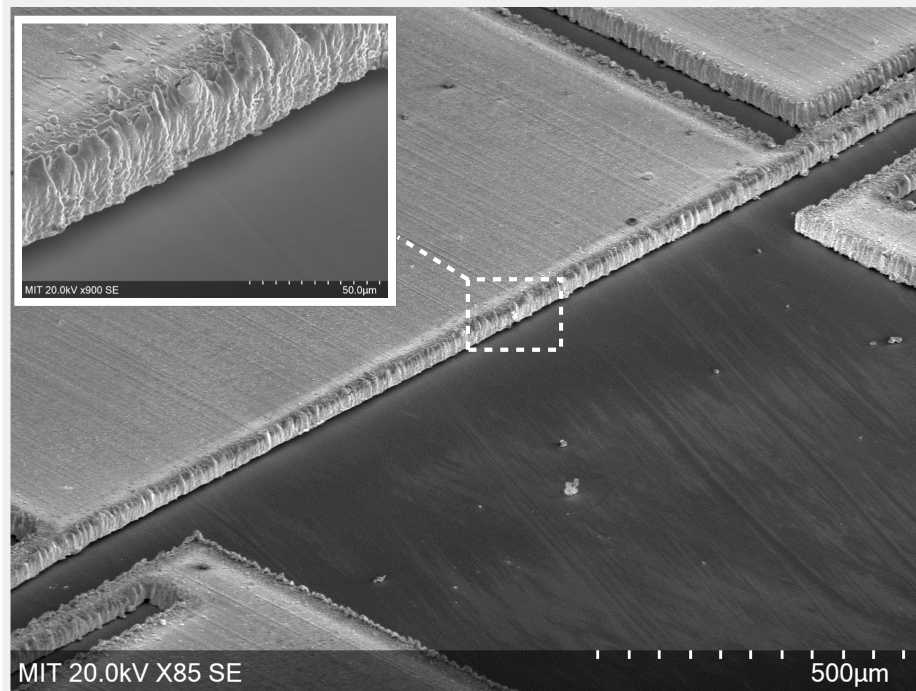

Figure 5-6: The 12.5μm gap between the freestanding structure and the substrate fabricated using a 12.5μm thick adhesive layer.

5.2.3 Limit on the Gap Between Laminates

As we saw in section 5.2.2, the gap between the MEMS structure and the substrate can be controlled by controlling the thickness of the deposited sacrificial layer (figure 1-5). As a result, a gap as small as few tens of nanometers can be fabricated using the surface micromachining process. These small gaps are desirable for certain MEMS devices such as electrostatic relays, where a small gap results in low pull-in voltage [119][120].

However, in the MALL process, the gap between the free-standing structure and substrate depends upon the thickness of the adhesive layer. This work demonstrates that a gap as small as 12.5μm can be fabricated using a 12.5μm thick adhesive layer. Figure 5-6 shows a cantilever fabricated with a 12.5μm gap between the structure and substrate. One approach to further reducing the gap can be to spin-coat the adhesive layer directly on the laminate sheet.

5.2.4 Poor Alignment Accuracy

In the conventional microfabrication process, MEMS layers can be fabricated with sub-micron alignment accuracy [121][122]. However, the alignment accuracy in the MALL process is limited to $2.5\mu m$ (figure 1-4). The alignment accuracy can be further improved by utilizing kinematic coupling [123] and passive mechanical alignment features [124].

5.2.5 Heat Affected Zone

The laser micro-machined parts suffer from the heat-affected zone (HAZ) [125]. Although the LAMPE micromachining minimizes HAZ by circumventing vaporization and plasma formation, the heat-affected zone can not be completely eliminated. This thesis relies on the scanning electron microscope pictures (such as figure 3-4 and figure 3-11) to estimate the extent of HAZ, which is found to be approximately $1\mu m$. However, additional metrology techniques must be employed to accurately estimate the heat-affected zone.

The heating of the material can lead to a change in material properties. For MEMS with a characteristic length smaller than the heat-affected zone, this change in material property can significantly affect the performance of a system. The heat-affected zone can be minimized in some materials, which have large optical penetration depth, by utilizing ultrashort pulsed laser micromachining [126].

5.3 Volume Manufacturing

In deep reactive ion etching (DRIE), many devices can be fabricated in parallel, resulting in a high part production rate. However, the laser direct-write micromachining process used in MALL is a serial process and MEMS are fabricated one device at a time. As a result, the part production rate in MALL process is low. Figure 5-7 compares the part production rate of DRIE and MALL. As can be seen, the MALL process is suitable for low-volume production and requires less initial investments. However, for investments greater than one million dollars, the part production rate of DRIE process increases significantly.

The part production rate in MALL process can be increased by implementing the following modifications:

1. Using a roll-to-roll lamination process to automate the assembly.
2. Integrating laser-micromachining and roll-to-roll lamination process by delivering the laser over the laminates using galvanometer scanner mirrors. In this system, individual layers of a device can be fabricated simultaneously, and laminated to manufacturer MEM systems. Using laser-micromachining with the roll-to-roll lamination process also eliminates the need for layer alignment, as the patterns can be spatially offset to ensure accurate alignment.
3. Using multiple laser beams to fabricate many devices in parallel. These multiple beams can be either from different laser sources or split from a single high power laser beam.
4. Using high power laser and other precision manufacturing methods such as embossing, micro-milling, knife-cutting, wire-EDM to machine large-features at a high machining rate and reserving the low-etch rate laser-micromachining for small-features.
5. Integrating MEMS packaging with the roll-to-roll lamination process by including package layers in the lamination process. These package layers can be fabricated using embossing, micro-milling, and other conventional fabrication tools

In conventional MEMS fabrication, upgrading from a 150 mm wafer facility to a 300 mm wafer facility is a significant cost. However, in MALL fabrication, adding additional lasers for parallel manufacturing is easy and the cost is incremental. After the initial investment in the laser micromachining system, for every additional \$20,000, an additional laser can be attached to the system for parallel manufacturing (see section **??**). Assuming that a laser micromachining system is $\$100,000$, and a DRIE system is $1M$. For an equal investment of $\$1M$ in MALL, a laser micromachining system with 46 lasers can be built, which can produce 46 devices in parallel. Using such system, for the comb-drive actuator discussed in

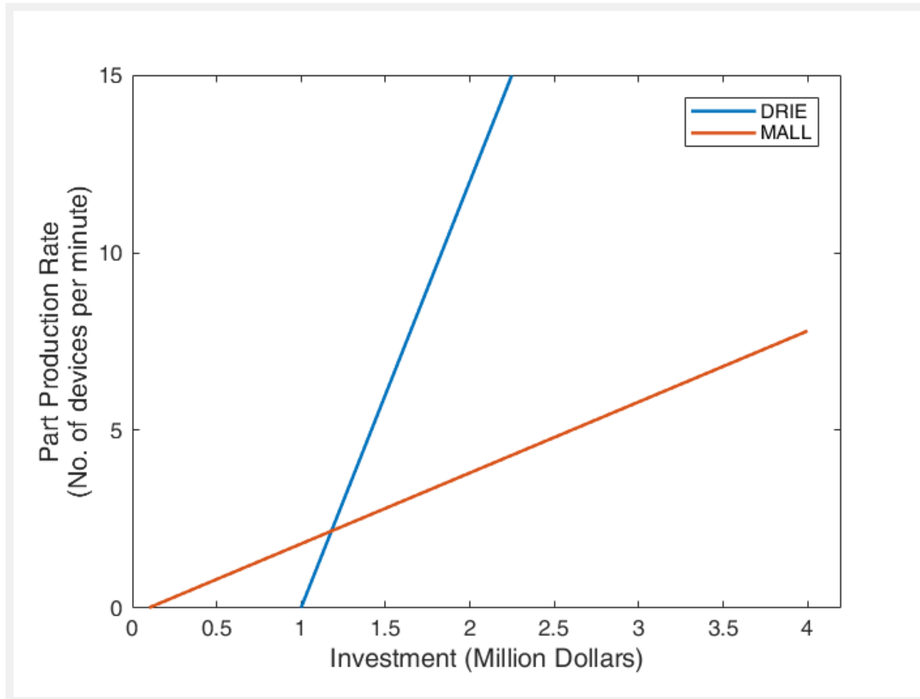

Figure 5-7: Part production rate of MEM relay fabrication using DRIE and MALL process.

section section 4.2, 46 devices can be manufactured in $12min$ or 0.26 devices per minute. Thus, the part production rate in MALL can be matched with DRIE.

5.4 MEMS for Masses

Micro-electromechanical systems have many potential applications in healthcare, automobile, and consumer electronics. Unfortunately, due to the high cost of equipment ownership, research in MEMS has been primarily limited to industries and universities with microfabrication facilities.

A typical microfabrication facility requires tools such as spin coaters, mask aligners and exposure systems, chemical vapor deposition (CVD) systems for material deposition, and etching tools such as deep reactive ion etching (DRIE). These tools are not only expensive but also require specialized buildings to house them. For example, the photolithography process should be performed in a cleanroom environment to minimize interference of dust

particles in exposure process. Similarly, the DRIE process requires specialized gas fittings for etching gases and safety alarms for leak detection. In addition, the chemicals used in lithography-based microfabrication process are expensive, hazardous, and require special storage and disposal.

In recent years, there has been considerable interest in developing table-top microfabrication tools for low-cost fabrication and rapid development of MEMS. For example, focused ion beam (FIB) milling [127][128] is extensively used as a rapid-prototyping tool for microfabrication. However, FIB systems cost approximately a million dollars and have high maintenance cost. Moreover, the gallium filaments used in FIB is consumed rapidly during operation, resulting in high operating cost.

Another approach that is gaining popularity as a table-top microfabrication tool is 3D micro-additive manufacturing [129]. This approach utilizes stereolithography [130] and two-photon polymerization [131] to fabricate MEMS. These processes have the advantage of offering true three-dimensional microfabrication. However, the fabrication material is limited to certain photo-curable polymers. Moreover, the print time is often much longer. Furthermore, for stereolithography, the print resolution is larger than the features required in many MEMS devices, and the build volume of the two-photon polymerization is small for many MEM systems.

As can be seen above, the major obstacle in engaging a larger scientific community in MEMS research is the substantial capital investment required to procure microfabrication tools. In addition, the high cost of equipment maintenance and consumables such as silicon wafer, photoresists, developers, and etchants further hinder the access of MEMS fabrication to a large portion of the scientific community.

In contrast, the MALL process utilizes a laser micromachining system, which has three advantages. First, single equipment replaces a set of tools, mainly spin coater, mask aligner, exposure system, and DRIE system, required for micromachining. Second, the cost of laser micromachining system is significantly less than conventional microfabrication tools. Third, the consumables are limited to electropolishing solution and metal foils. These materials

cost \$0.0015 per device, significantly lower than of silicon wafers used in conventional MEMS fabrication.

This thesis uses a commercially available laser micromachining system from Oxford Lasers Ltd [56], which has a high cost of ownership. However, the laser micromachining systems can be built at a much lower cost and used to fabricate MEM systems. The major cost in the Oxford Laser micromachining system comes from the 2-axis motion system and the laser source. The high cost of the 2-axis stage is due to its long-travel range of $100mm$. However, for fabricating MEMS, a travel range of $10mm$ is sufficient. As a result, the expensive 2-axis stage can be replaced with 2-axis galvanometer mirrors (costs around \$2500 [60]) or a piezo linear stage (costs around \$750 per axis [132]). A $5W$ pulsed laser system costs about $\$15,000$ (D. Roland, personal communication, November 6, 2018). The recent development in rapid prototyping of rapid prototyping machines [133][134] has considerably reduced the complexity and cost of machine building. Assuming another \$2500 for focusing optics and machine building, the total cost of the system comes out to be $\$20,000$.

As can be seen above, the major cost in a laser micromachining system comes from the laser source. The cost of the laser source depends upon its average power. A high power laser requires a high-intensity pumping source, resulting in increase in the cost of the laser. For example, the diode-pumped laser used in this work uses an array of light-emitting diode (LED) to pump the laser medium. These diode-arrays require specialized high-current power supply and cooling system, which are not only expensive but also have a large footprint.

The LAMPE micromachining process requires average power in the range of $280mW$ (Table 3.2), thereby needing a laser with significantly low power. The low power lasers require less intense pumping source; as a result, cost less and have a small footprint. The low-cost laser system, in conjunction with low-cost machine building can be used to develop low-cost table-top MEMS manufacturing systems.

The table-top MEMS manufacturing can reduce the cost of MEMS fabrication and enable rapid prototyping, thereby democratizing MEMS fabrication and accelerating the

development of novel micro-electromechanical systems.

5.5 Thesis Contributions

The key contributions of this thesis are as follows:

1. The LAMPE micromachining process to fabricate high aspect ratio (as large as 10:1) structures with diffraction-limited lateral features. The LAMPE micromachining can be used to process a wide range of materials, including metals, silicon, and diamond. In LAMPE micromachining of metals, laser is used to melt (i.e., induce phase-change) the metal, and then the liquid-metal is expelled by the pressure generated from vapor baubles formed at the laser-metal interface. Similarly, in LAMPE micromachining of silicon, the laser is used to oxidize the silicon (i.e. induce phase-change), which transmits the laser (due to low absorption coefficient), causing further oxidation of silicon beneath. The formed silicon oxide is granular and expelled by pressure generated from vapor baubles formed at the laser-material interface due to partial vaporization of silicon. Likewise, in LAMPE micromachining of diamond, laser is used to convert the diamond into graphite (i.e., induce phase-change), and then the newly formed graphite is oxidized into carbon dioxide in the presence of environmental oxygen.

2. The electro-deburring process to remove the burrs present in laser micromachined parts, thereby enabling their application in MEMS parts.

3. The MALL MEMS fabrication process, which can potentially enable greater material selection and integration, greater design flexibility, easier packaging, low-cost manufacturing, and rapid development of micro-electromechanical systems.

4. An electrostatic comb-drive actuator fabricated from metal. Previously, it was assumed that these parts with such small features and high aspect ratio could be fabricated from silicon alone, using the lithography-based deep reactive ion etching (DRIE) process.

5. MEM relays for high-current switching application. These relays can be assembled from the elementary conducting and insulating parts and could be used as the logic organ for Von Neumann universal constructor [135].

6. Demonstrating high-aspect-ratio machining of diamond and its application in fabricating diamond rotors for magic-angle spinning nuclear magnetic resonance (MAS-NMR) spectroscopy.

5.6 Conclusion

In conclusion, the MALL MEMS fabrication process presented in this thesis has the potential to replace the conventional microfabrication process used for MEMS manufacturing. The MALL process enables MEMS fabrication with a wide range of material, thereby empowering a new paradigm in MEMS design, functionality, and applications. Moreover, the manufacturing cost per device in MALL fabrication is low due to using low-cost fabrication materials such as metal foils. In contrast, in conventional microfabrication, the fabrication material is largely limited to silicon, which restricts the design, functionality, and application of MEMS, and increases the manufacturing cost per device.

The development time and cost in MALL is less due to the independent development of device layers and their effortless integration. The MALL process is well suited for one-of-a-kind and low-demand MEMS market because of the low cost of development. In contrast, creating new MEMS devices in conventional microfabrication requires developing and integrating various material deposition/etching processes, which increases the development time and cost. Thus, even though the cost of manufacturing per device is low, the total cost per device is large. Due to this limitation, the commercialization of MEMS products has been largely limited to markets in which the huge demand can compensate for the high cost of development.

The tools and material cost of MALL fabrication is approximately $\$25,000$, which is

affordable to a wider scientific community. This democratization of MEMS fabrication can expedite the development of novel MEMS systems. Traditionally, the research and development of novel MEMS devices have been largely limited to a few industries and universities, due to the high cost of equipment ownership.

5.7 Recommendations for Future Work

The recommendations for future work are listed below:

1. This work relies on optical microscope image and X-ray dispersion spectroscopy (EDS) analysis to conclude oxidation of silicon during LAMPE micromachining. The laser-assisted oxidation of silicon can be further confirmed by performing LAMPE micromachining in an inert environment. My hypothesis is that in an inert environment, the LAMPE micromachining of silicon should not result in any material removal, due to the absence of oxidation.

2. To further increase the aspect ratio in LAMPE micromachining of silicon, the I recommend performing LAMPE micromachining in HF vapor environment. My hypothesis is that the HF vapor will react with the newly formed SiO_2 to form colorless gaseous silicon tetrafluoride SiF_4, which would be removed efficiently. As a result, the depth of the micromachining can be further increased by gradually moving the focus downwards as the material is removed.

3. An x-ray diffraction measurement is recommended to verify the graphitization of diamond. Moreover, the oxidation of graphite into CO_2 in the oxygen environment can be verified by performing LAMPE micromachining in an inert environment. My hypothesis is that in the inert environment, the LAMPE micromachining of diamond would not lead to any material removal due to the absence of oxidation of graphite.

4. This work uses a 3-axis stage to move the machining target with respect to the laser. However, using a galvanometer scanner is recommended to increase the LAMPE

micromachining rate.

5. For the MEM relay discussed in section 4.3, it is recommended to apply a conformal coating of a dielectric material such as parylene on the gate electrode to isolate it from the actuator electrode. The application of parylene coating is expected to reduce the pull-in voltage and increase the maximum safe operating voltage.

6. For materials with low absorption coefficient such as silicon and diamond, it is recommended to use ultra-short laser (in the order of femtoseconds to picoseconds) for LAMPE micromachining. The ultra-short laser is expected induce phase-change while minimizing the heat-affected zone (HAZ). However, it must be noted that the LAMPE micromachining of metals requires long pulses in the order of nanoseconds. In metals, the optical penetration depth is very small (a few nanometer) and the metal is melted through heat conduction. As a result, long pulses in the order of nanoseconds are required to dump sufficient energy to induce the melting and expulsion.

7. For machining films with thickness less than $10\mu m$, it is recommended to use ultra-short pulsed lasers irrespective of the absorption coefficient of the material. In ultra-short pulsed laser micromachining, the micromachining depth per pulse is equal to the optical penetration depth of the material. The high pulse energy and repetition rate ($100KHz$) lead to sufficient number of pulse irradiation per spot, resulting in machining depth in the order $10\mu m$.

Appendix A

A.1 Manufacturing Cost Estimates for DRIE and MALL

The cost of producing one device is given by the expression:

$$Cost\ per\ device = Material\ cost\ per\ device + Equipment\ cost\ per\ device \tag{A.1}$$

The material consumable cost can be calculated by adding the cost of wafer, etching gas, and electricity etc. Due to lack of reliable information about the etching gas and electricity consumption, only wafer cost is included in the presented calculation.

The material cost per device is given by the expression:

$$Material\ cost\ per\ device = \frac{Cost\ of\ wafer \times Area\ of\ device}{Area\ of\ wafer} \tag{A.2}$$

The equipment cost per part can be calculated by dividing the equipment cost with total number of parts produced in the lifespan of the equipment and given by the expression:

$$Equipment\ cost\ per\ device = \frac{Cost\ of\ Equipment}{Device\ production\ rate \times Equipment\ lifetime} \tag{A.3}$$

The total number of parts produces is given by the expression:

$$Number\ of\ parts\ = Parts\ produced\ per\ dollar \times Total\ investment \quad \text{(A.4)}$$

The *Cost per device* and *Device production rate* depends upon the design of the device. The calculations presented here are for the comb-drive actuator discussed in section 4.2. The assumptions and values of different variables used for calculations are listed in Table A.1

A.1.1 Cost of Manufacturing Using DRIE

Part Production Rate

It is assumed that the device is fabricated on SOI wafer and DRIE is used to etch the comb-drive structures. The etch rate is $1\mu m/min$ and the device thickness is $100\mu m$. Therefore, it will take $100min$ to process a wafer (neglecting wafer loading/unloading time).

The length of the comb-drive actuator is $6.5mm$ and the width is $4.5mm$. Assuming $150mm$ diameter SOI wafers are used for production, and $500\mu m$ margin is kept around the device for dicing the wafer, the total number of devices produced per wafer is 428. As a result, number of devices produced per minute or production rate is 4.28 devices per minute.

$$DRIE\ Part\ Production\ Rate = 4.28\ devices/min$$

Manufacturing Cost

Assuming that the lifespan of DRIE system is 5 years or 2628000 minutes, the total number of the devices that can be produced during the lifespan of the system is 11 million parts. If the cost of the equipment is $\$1M$, the equipment consumable cost per device is \$0.09

Assuming SOI wafer is used for fabrication and each wafer costs \$220 [114]. Since 428 devices can be fabricated per wafer, the material cost per device is \$220/428 = \$0.51. The total cost of fabrication per device using DRIE is \$0.6, and 6.94 devices can be produced with one dollar. As can be seen, 85% of the total cost is due to material cost.

$$DRIE\ Cost\ per\ Device = \$0.51$$

A.1.2 Cost of Manufacturing Using MALL

Part Production Rate

The laser micromachining process is a serial process and the part production rate depends upon the actual design of the device. Moreover, depending upon the design, laser bulk micromachining (LBM) can be employed to rapidly remove the material from the region with large features, while LAMPE micromachining can be employed for region with small features and high aspect ratio. As a result, unlike DRIE, the part production rate in MALL depends upon the actual design of the MEMS device.

To calculate the MALL manufacturing cost, the comb-drive design discussed in section 4.2 is used. The device is fabricated by first removing the excess material around the beam springs and interdigitated fingers using LBM, followed by LAMPE micro-machining interdigitated fingers. The etch rate of the laser bulk micromachining is given by the equation:

$$E_{LBM} = \eta A_\phi A_h F$$

where η is .25, A_ϕ is diameter of ablation profile, A_h is depth of the ablation profile, and F is feed rate. The expression for feed rate is given by the equation:

$$F \leq \eta A_\phi F_p$$

For laser bulk micromachining copper in fabricating comb-drive actuator, $\eta = 0.25$, $A_\phi = 25\mu m$, $A_h = 25\mu m$, and $F_p = 10KHz$. As a result,

$F_{max} = 100mm/s$

The practical limit on achieving feed-rate depends upon the acceleration/deceleration rating and inertia of the motion system. The laser micromachining system used in this

work has acceleration/deceleration rating of $10,000mm/s^2$ and large inertia; as a result, the maximum achievable feed-rate for MEMS length-scale distance is of the order of $1mm/sec$. However, using galvanometer mirrors, much higher feed rate can be achieved. A typical 2-axis galvanometer mirror can operate at $100Hz$ frequency [60]. Assuming, the scan distance of $1mm$, a feed rate of $100mm/s$ can be easily achieved. For the presented calculation, a feed rate of $50mm/sec$ is used, to account for acceleration/deceleration limits of galvanometer mirrors, resulting in material removal rate of $E_{LBM} = 0.29mm^3/min$. For fabricating the comb-drive actuator, about 18% of the device volume is removed, which takes approximately 1.8 minutes.

Finally, the comb-drive fingers are fabricated using LAMPE micromachining. The machining length is $24.6mm$ and cutting feed rate is $2.4mm/min$ (or $40\mu m/s$); therefore it requires $10.2min$ to LAMPE micromachine the comb-drive actuator. The total time required to fabricate a comb-drive actuator in MALL process is 12 minutes. The part production rate is:

$$MALL\ Part\ Production\ Rate = 0.08\ devices/min$$

Manufacturing Cost

Assuming the lifespan of laser micromachining system is 5 years or 2628000 minutes, the total number of the devices that can be produced during the lifespan of the system is 0.22 million parts. Assuming the cost of the laser micromachining is \$100,000, the equipment cost per device comes out to be \$0.46.

The material for MALL fabrication is $100\mu m$ thick copper foil. A roll of copper foil 6" wide & $268ft$ long cost \$449 [136] and can accommodate 297040 devices; therefore, the material cost for each device is \$0.0015. The total cost of device fabrication is:

$$MALL\ Cost\ per\ Device = \$0.4615$$

Variable	**Value**
DRIE	
Cost of DRIE	\$1M
Lifetime of DRIE	5 years
Yield	100%
DRIE etch rate	$1\mu m/min$
Wafer loading/unloading time	$10min$
Cost of SOI wafer [114]	\$220
Diameter of SOI wafer	$150mm$
Comb-drive area	$6.5mm \times 4.5mm$
Comb-drive thickness	$100\mu m$
Dice-saw margin	$500\mu m$ each side
MALL	
Cost of laser micromachining system	$\$100,000$
Lifetime of laser micromachining system	5 years
Cost of copper foil ($6^{"} \times 268ft$)[136]	\$449
Comb-drive critical machining length (for LAMPE Micromachining)	$24.4mm$
Percentage of total volume removed using LBM micromachining	18%

Table A.1: The values of variables used for calculating manufacturing cost.

Appendix B

Here, I describe the MALL fabrication process in detail.

B.1 Equipment Required for MALL Fabrication

Below is the list of tools required for MALL MEMS fabrication:

1. A laser micromachining system. This thesis uses a laser micromachining system from Oxford Laser Ltd [56]. (I am interested in building a low-cost DIY laser micromachining system in future. Please check http://mtm.cba.mit.edu/ for updates.)

2. Depending upon the feature size of the device, a scanning electron microscope or a high resolution optical microscope is required to inspect the MEMS device during fabrication. A low magnification stereo microscope is also useful for quick inspection.

3. A chemical hood and a voltage source is required to perform electro-deburring process.

4. A critical point dryer may be required. In my experience, for MEMS fabricated with metals, dipping the device in isopropanol (IPA) and drying on a hot plate is sufficient. However, for MEMS fabricated with silicon and containing small features, a critical point dryer is desirable.

5. A hot plate is useful for quickly drying the wafers.

6. A toaster oven with a temperature controller is required for certain adhesive that need curing at higher temperature. Particularly, the Dupont FR1500 adhesive used in MEM relay, require baking at 185 degree centigrade. Other adhesive that is used in this work is 3M thermal bonding film 583, which can be either solvent activated or pressure activated, and does not requires baking.

7. A vacuum tweezer is desirable to facilitate manipulating the delicate sheets after laser micromachining process.

8. Depending upon the MEMS device, addition tools may be required for device testing. For example, in this thesis, the MEM relay is tested using a semiconductor parameter analyzer. A probe station is also required for electrical testing of the device.

9. For certain MEMS devices, a table-top precision milling machine can be useful. The bottom layer of MEM relay discussed in section 4.3 is fabricated using a table-top precision milling machine.

Below is the list of materials required for MALL fabrication:

1. The main material used in MALL MEMS fabrication is metal foils. These metal foils can be sourced from https://www.mcmaster.com/.

2. The main adhesive layers used in this work are Dupont FR1500, 3M thermal bonding film 583, and scotch double sided tape. These adhesives can be sourced from there corresponding vendors.

3. Electrolyte for electro-deburring process. For copper, either copper sulfate or phosphoric acid can be used.

4. Dowel pins or gauge pins for using them as alignment pins.

B.2 MEMS Design

In this thesis, I use Fusion 360 for designing MEMS. The software offers the advantage of integrating the computer aided design (CAD) and computer aided manufacturing (CAM), and is well suited for MALL MEMS design. Since the MALL process is a laminate process, it is advantageous to design the MEMS system in form of layers. Once the design is finished, the g-code for laser toolpath can be exported using the CAM interface of the Fusion 360 program. This g-code program is used for performing the laser micromachining.

Depending upon the MEMS device design it is advisable to export two different laser toolpath. The first toolpath is for the part of the region where small feature sizes are not required and high power laser can be used to remove the material at high micromachining rate. The second toolpath is for parts of the MEMS design which have small features, and require LAMPE micromachining process.

B.3 Fabrication

B.3.1 Laser Micromachining

In this thesis, the laser micromachining is performed using a commercially available laser micromachining system from Oxford Laser Ltd [56]. Following are steps for

S1: The metal foil is clamped to the stage using a clip. For metal foils with thickness up to $20\mu m$, tweezers can be used for manipulations. However, for thickness below $20\mu m$, it is desirable to attach the metal foil with to a rigid frame for easy manipulation.

S2: Selecting the laser source: For metals, the laser micromachining process is generally independent of the laser wavelength. This is due to the fact that the absorption of laser by the metal is low in the UV, Vis, and IR range. The pulse duration of the laser is essential to get the small feature size. Use equation (3.5) to determine the required pulse width for a desired feature size. Often the laser pulse width is fixed, and the

user only has control over the pulse power. The laser system used in this work has fixed pulse duration of 20 ns.

S3: Selecting the focusing optics: Depending upon the feature size, the desired lens or objective is installed. The laser micromachining system is equipped with a digital camera for sample inspection. Next, the sample is brought into the focal plane of the lens by inspecting in the imaging system.

S4: Selecting laser power and process development: Use equation (3.6) to determine the required laser power for the laser micromachining. A series of power tests in the vicinity of this calculated laser power can be used to determine the exact value of the power which gives the minimum feature size. The laser micromachining should be performed at this value. It must be noted that, the feature size also depends upon the degree to which the sample is at the focal plane. Usually, before performing the power test, I perform a series of focus tests to determine the best focus. Sometimes a second pass might be required if the laser micromachined part does not fall off during the laser micromachining process.

B.3.2 Electro-deburring

The steps for performing electro-deburring are as follows:

S1: Selecting the electrolyte: The choice of electrolyte depends upon the deburring metal. Since the eletro-deburring process is similar to electropolishing and electroplating process, the choice of electrolyte is same as of that used for electropolishing or electroplating. There is a great body of work on available electrolytes for various metals. In this work, copper is used for fabricating MEMS. For copper, 14M phosphoric acid is used as the electrolytic solution.

S2: Electro-deburring setup: The laser micromachined copper part is connected to anode and another copper sheet is connected to the cathode. Both electrodes are dipped inside 4M phosphoric acid solution.

S3: Selecting the electro-deburring voltage: Setting the right voltage is essential to remove burrs. As can be seen in figure 3-9, the electro-deburring voltage must be greater than the electropolishing temperature to ensure the removal of the burrs. The electropolishing process is well studied and the value of the electropolishing voltage for a given metal and electrolyte can be found in the literature. The electro-deburring voltage should be above this value. In this work, the electro-deburring of laser micromachined parts is performed at $5V$ for 30 seconds. Generally, the electro-deburring voltage is a little less than the votlage at which the bubbles starts to form at the anode.

S4: For some MEMS devices, a gold electroplating may be desirable to prevent oxidation of the metal.

S5: After the electro-deburring, the laser micromachined part can be rinsed in DI water followed by isopropanol rinse. The cleaned laser micromachining part can be either air dried at room temperature or at 85 degree centigrade inside an oven.

B.3.3 Lamination Process

The steps for lamination are as follows:

S1: For the lamination process, the adhesive layer is first tack bonded to the substrate layer. For tack bonding the Dupont FR1500 adhesive layer, the curing is performed at $120°C$.

S2: Once the adhesive is tack bonded to the substrate, the backing layer is removed and the top device layer is attached. Alignment pins are used for the alignment. For devices requiring high alignment accuracy, alignment pins with diameter of $500\mu m$ is used to improve the alignment accuracy. However, for the device which does not require a high alignment accuracy, thicker alignment pins (for example, $1.5mm$ diameter dowel pins) can be used to simplify the assembly process.

S3: Once aligned, the laminate structure is sandwiched between a custom-made alignment fixture and clamped using a paper clip and put inside the oven for full curing. The temperature of the oven is set to $185°C$, and the baking is performed for $5-20$ minutes depending upon the device and adhesive layer thickness.

S4: After the lamination process, the MEMS device can be cut-out from the laminate structure using laser cutting. However, this step is not required during the device development.

B.4 MEMS Device Testing

The actual steps for testing the device depend upon the actual design of the device. Here, I outline the general steps which are common to many MEMS devices:

S1: After the device fabrication, it is advised to inspect the device in an optical microscope to check the integrity of the device.

S2: Care must be taken to handle the MEMS devices, as they are very fragile. Do not blow air to dry or remove dust particles, it will break the device.

S3: For electrical testing, use probe station probes to make the electrical connection. A wire-bonder can be used as well. In my experience, for devices made out of copper, using gold ball-bonding at $100°C$ works very well.

B.5 Things That did Not work

Here, I list all the failed experiments and things that did not work:

1. First time observed high diffraction-limited features while trying to machine $50\mu m$ silicon wafer. Unfortunately, the success was very short lived, the wafer was very fragile and the device broke. Figure B-1(a) shows the the broken comb-drive structure.

2. Decided to use brass as it is less fragile and cheaper. However, the part had much carbon deposited as shown in figure B-1(b).

3. Tried all sorts of way to remove the carbon and burrs with no success. Tried physical scrubs, but the MEMS parts were very fragile and would deform. Tried sonication but it won't remove the burrs. Tried prolonged sonication, and broke many devices. Figure B-1(c) shows once such device. Concluded sonication can not be used to remove the burrs.

4. Tried many adhesive layers with no success. The Dupont FR1500 would stick but the bonding was not sufficient and the device layer will come off as shown in figure B-1(d). It turned out that I wasn't baking it at right temperature. The right baking temperature is $185°C$.

5. Decided to make comb-drive device in a nitride wafer by patterning the top layer and then performing a potassium hydroxide etch. Figure B-5(a) shows the device after laser micromachining. Unfortunately, the device did not survive the etch step (figure B-5(b))

6. I tried making 2.5D structure in silicon using laser micromachining, however, the surface roughness was very high as shown in figure

7. I tried to use normal pulsed laser ablation micromachining to fabricate comb-drive actuators. Despite of spending months, it did not work. Either the distance between the comb-drive was too large ($\sim 30 = 40\mu m$) or there was some material left between the comb-drive fingers (figure B-2(a)) which resulted in a short-circuit between the fingers. Any amount of electro-deburring would not remove this left-over material. The LAMPE micromachining ensures complete removal of material, while maintaining the small lateral features.

8. After using LAMPE micromachining, I was able to fabricate a device, in which, there was no short-circuit between the comb-drive. I tested the device and the fingers moved.

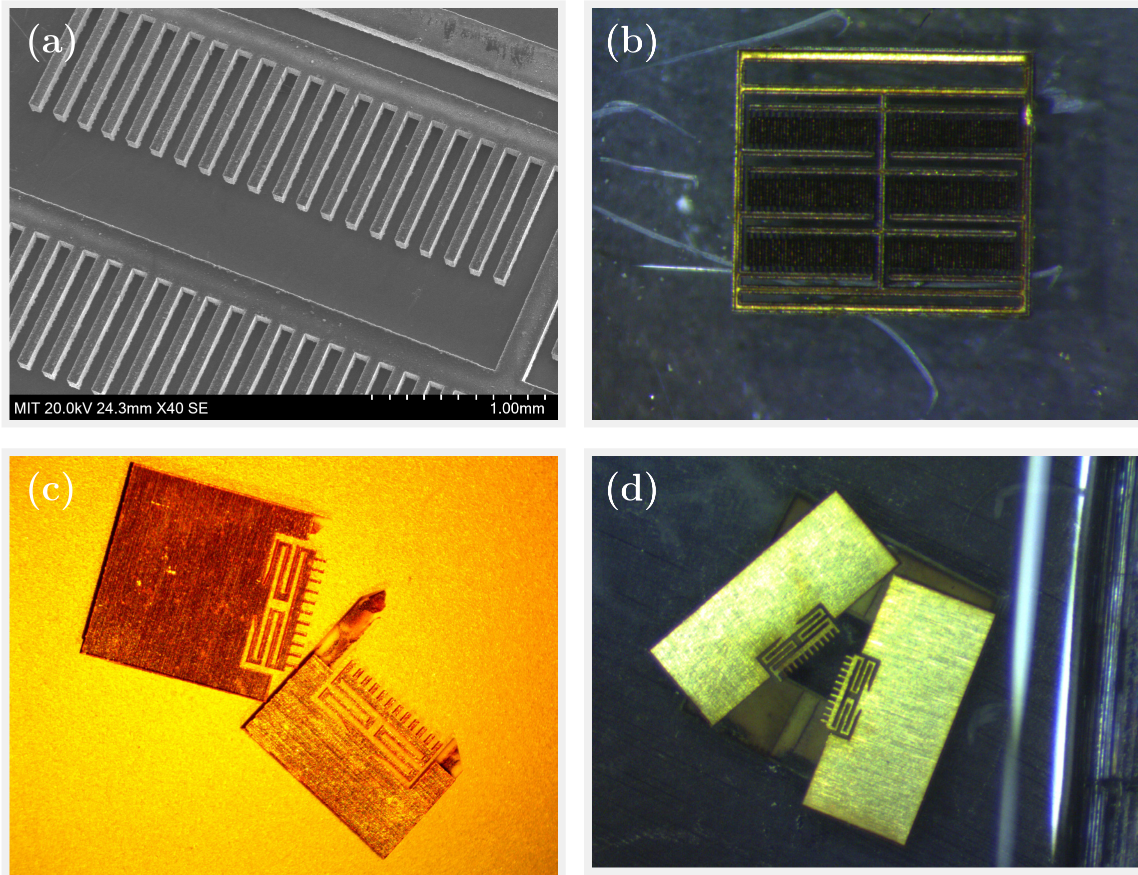

Figure B-1: (a) Broken comb-drive structure device fabricated in $50\mu m$ silicon wafer. (b) Comb-drive in $250\mu m$ brass. The micromachined part had much carbon deposits. (c) Broken device after 5 minutes of sonication to try to remove burrs. The sonication was carried in a brass cleaner, which is a mild enchant. (d) Broken device due to insufficient adhesive of the device layer to the substrate layer.

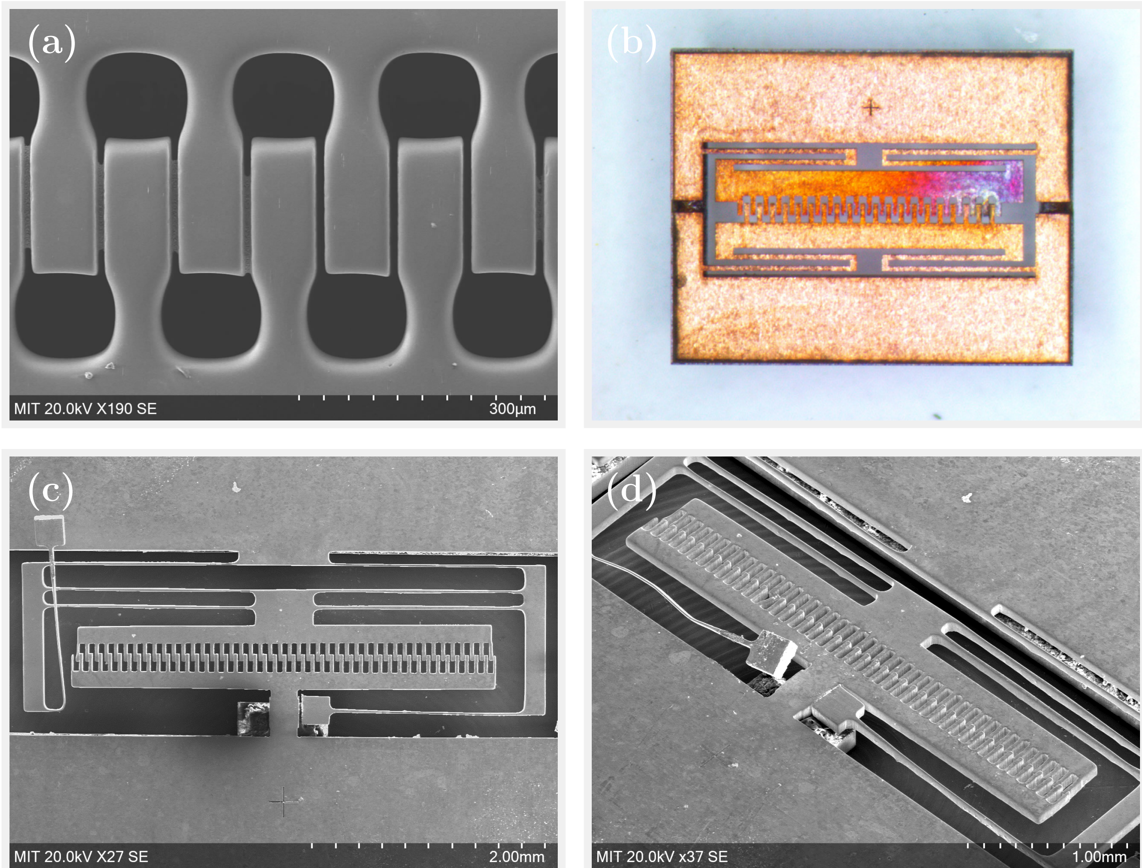

Figure B-2: (a) Material left between the comb-drive fingers when normal pulsed laser ablation micromachining is used. (b) Comb-drive actuator after the short-circuit due to side-pull. (c) & (d) Broken device because the beam-spring will come off from the post. It required increasing the pressure during the lamination and baking process to make sure the beam spring is securely bonded to the post.

However, as usual the success for short lived. The design of the beam spring was not suitable for the comb-drive, and could not resist the side-pull. After a certain voltage, the fingers got connected resulting in short circuit. Figure B-2(b) shows the first device that worked and then resulted in short circuit.

9. Changed the design and used folded-flexure springs to minimize the side-pull. However, the spring won't stick to the post as shown in figure B-2(c). It required increasing the pressure during laminate assembly and baking process to make the beam spring stick to the post.

10. I tried multiple device design for MEM relays. Figure B-3(a) shows the cantilever design. This was fabricated by laminating the top cantilever laminate on a silicon substrate. I decided not pursue this direction because it required silicon substrate, however, I wanted to show device demonstration with metal. Moreover, it required depositing gold electrodes on the substrate. Furthermore, I was worried about the stiction problem.

11. I also tried $10\mu m$ thick silver layer attached to $200\mu m$ thick silicon frame for the actuator electrode. Figure B-3(b) shows the fabricated device. I decided to not pursue it for the same reasons as above. It used silicon wafer, and required deposited metal electrodes on the bottom substrate.

12. Another design that I tried is shown in figure B-3(c). It did not work because the cantilever was making electrical contact with the gate and output electrode simultaneously. The MEM relay shown in figure B-3(d) has similar design and failed due to the same reason.

13. I spent a large amount of time trying to solve the problem of actuator electrode making electrical connection with the gate electrode. First, I tried reducing the height of the gate electrode below the input/output electrode. I was hoping that the actuator electrode will make contact with the input/output and will be blocked to further move and make connection with the gate electrode (figure B-4(a)). However, I was wrong. The actuator electrode plate is thin and can easily bend to cause electrical connection with the gate electrode.

14. Next, I tried bringing the input/output electrode closer to the center to minimize the bending of the cantilever plate (figure B-4(b)). However, it was not sufficient, and the actuator electrode was still making the electrical connection with the gate electrode.

15. I also tried attaching a stop layer on the cantilever as shown in figure B-4(c). However, when the voltage was applied, it made the contact with gate electrode first, thereby,

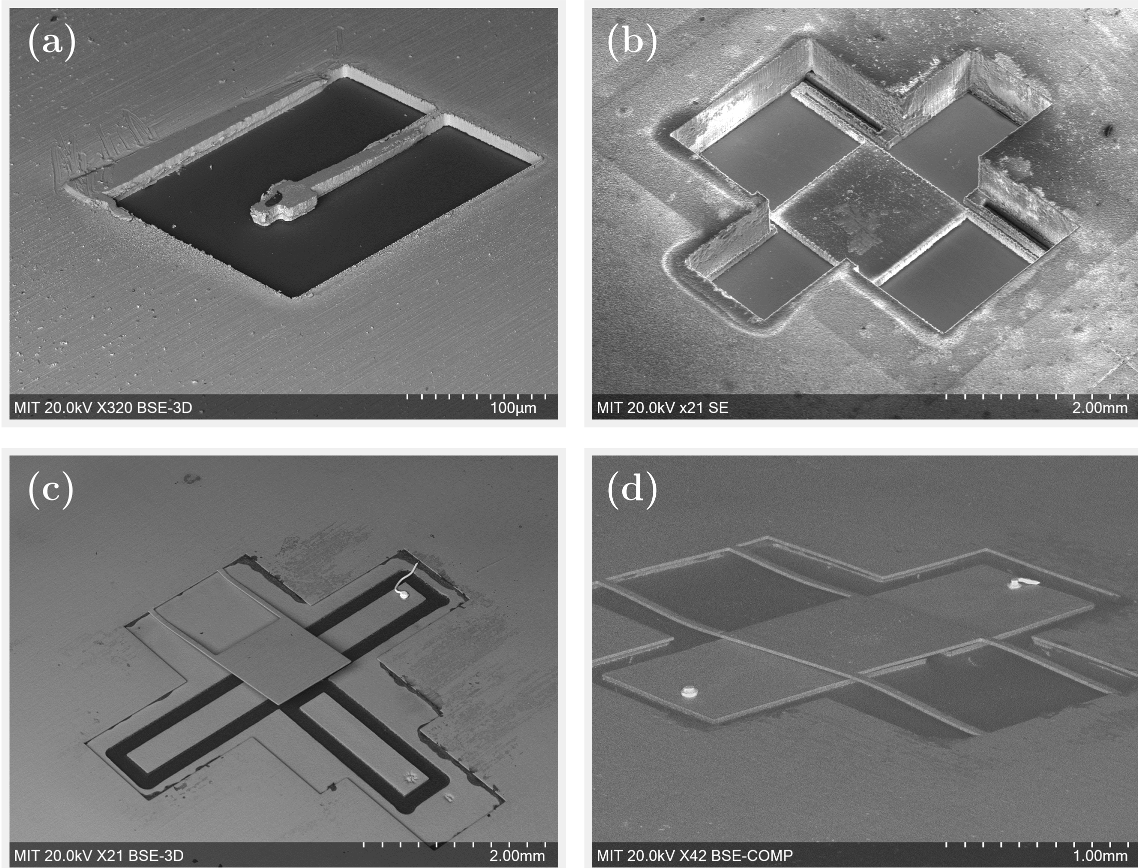

Figure B-3: (a) MEM Relay with cantilever design. I decided to not pursue this direction as it required deposited electrodes on the bottom silicon substrate. Moreover, I was worried about the stiction. (b) MEM relay design using $200\mu m$ thick silicon wafer as the frame. I decided to not pursue it because I wanted to show silicon-less MEMS fabrication. Moreover, it required depositing gold electron on the bottom substrate. (c) MEM relay with cantilever design. This design failed because the cantilever was making electrical connection with both the gate electrode and drain electron simultaneously. (d) Another MEM relay design which failed due to similar reason.

hindering the connection of actuator contact with the input/output contact.

16. I tried $25\mu m$ thick layer of corona dope (MG chemicals) to isolate the actuator electrode with the gate electrode B-4(d). To make the electrical contact with the gate electrode, the corona dope layer is removed from the edges as shown in the figure B-4(d). It worked very well. However, the pull-in voltage was between $500 - 600V$. Finally, I settled with the design discussed in section 4.3.

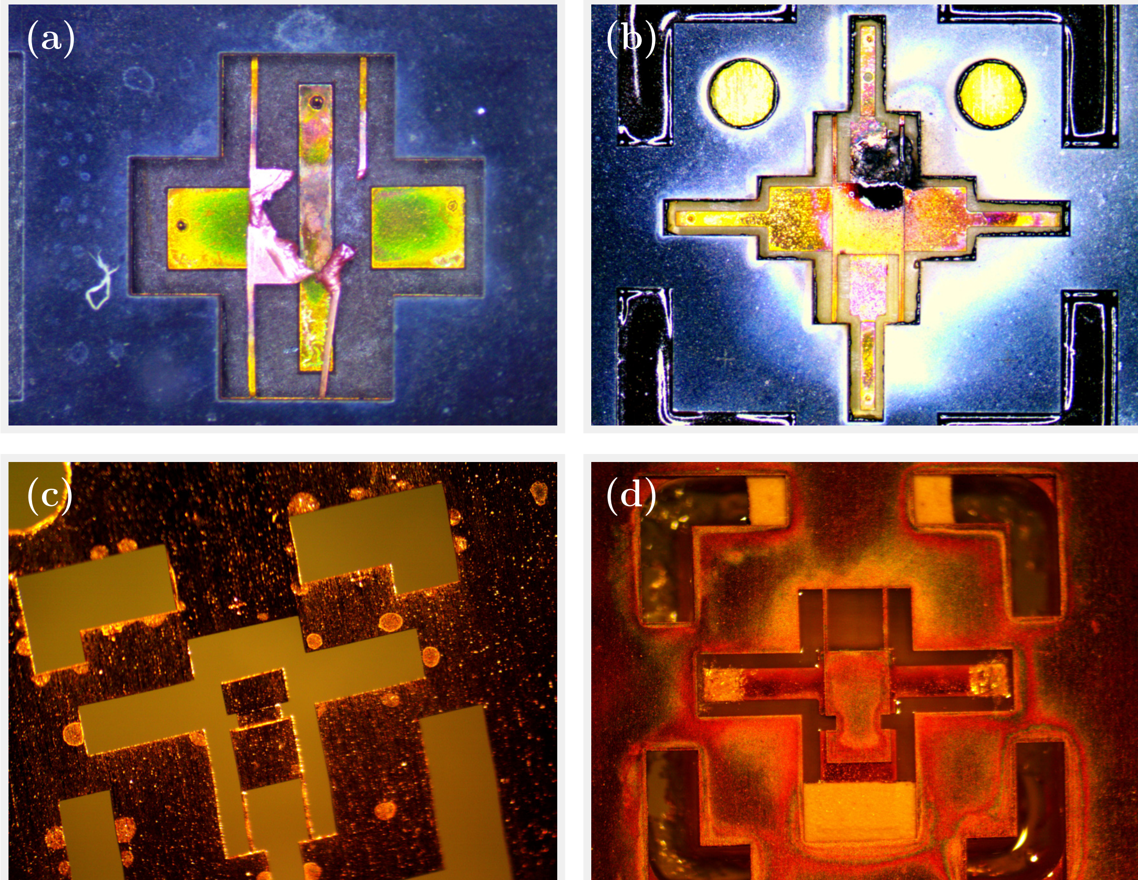

Figure B-4: (a) MEM relay design which broke due to the short circuit between the actuator electrode and the gate electrode (b) Another MEM relay design which broke due to similar reasons. (c) MEM relay design in which a post was attached to the cantilever to isolate actuator and the gate electrode. Unfortunately, the post made contact with electrode, thereby, hindering the connection between movable contact and the input/ouput contact (d) MEM relay design using a $25\mu m$ thick corona dope (MG chemicals) layer to isolate gate and actuator electrode. The device worked, however, the pull-in voltage was between $500 - 600V$ due to large thickness of the insulating layer.

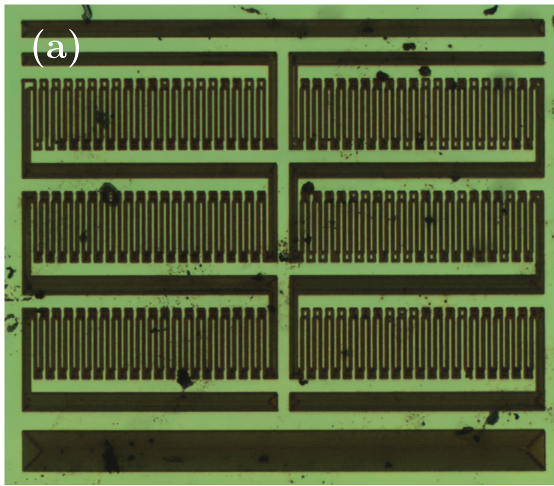

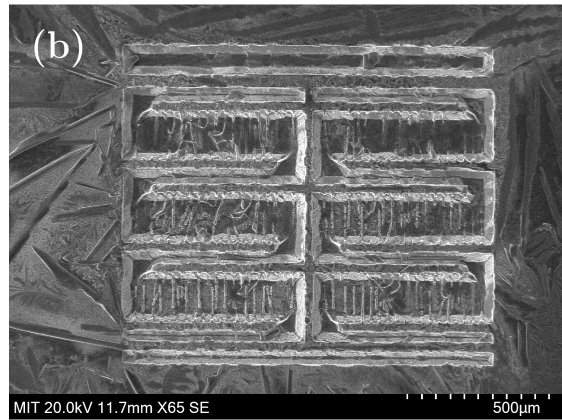

Figure B-5: (a) Comb-drive structure Laser micromachined on nitride wafer (b) Comb-drive device after potassium hydroxide etch

Bibliography

[1] D. Niarchos, "Magnetic MEMS: key issues and some applications," *Sensors and Actuators, A: Physical*, vol. 109, no. 1-2, pp. 166–173, 2003.

[2] S. D. Senturia, *Microsystem Design.* Springer Science & Business Media, 2007.

[3] R. Ramadoss, S. Lee, Y. C. Lee, V. M. Bright, and K. C. Gupta, "Fabrication, Assembly, and Testing of RF MEMS Capacitive Switches Using Flexible Printed Circuit Technology," *IEEE Transactions on Advanced Packaging*, vol. 26, no. 3, pp. 248–254, 2003.

[4] M. Weber B S and L. C. Kretly, "PCB-MEMS RF switch: Parametric analysis and design guide lines," *SBMO/IEEE MTT-S International Microwave and Optoelectronics Conference Proceedings*, pp. 141–144, 2007.

[5] H. P. Chang, J. Qian, B. A. Cetiner, F. De Flaviis, M. Bachman, and G. P. Li, "RF MEMS switches fabricated on microwave-laminate printed circuit boards," *IEEE Electron Device Letters*, vol. 24, no. 4, pp. 227–229, 2003.

[6] M. A. Mapar and M. Omidian, "Laminate MEMS for Heterogeneous Integrated Systems," *MRS Online Proceedings Library Archive*, vol. 1427, 2012.

[7] J. Tsai, A. Y. Zhang, G. P. Li, and M. Bachman, "A laminate cantilever waveguide optical switch," *Proceedings - Electronic Components and Technology Conference*, pp. 203–207, 2012.

[8] M. Bachman and G.-P. Li, "MEMS in laminates and package substrates," *2013 IEEE International Symposium on Advanced Packaging Materials*, vol. 1, no. Paper 32, pp. 121–125, 2013.

[9] J. P. Whitney, P. S. Sreetharan, K. Y. Ma, and R. J. Wood, "Pop-up book MEMS," *Journal of Micromechanics and Microengineering*, vol. 21, no. 11, 2011.

[10] H. McClintock, F. Z. Temel, N. Doshi, J.-S. Koh, and R. J. Wood, "The milliDelta: A high-bandwidth, high-precision, millimeter-scale Delta robot," *Science Robotics*, vol. 3, no. 14, p. eaar3018, 2018.

[11] M. Bachman and G. P. Li, "Laminates for MEMS and BioMEMS," *14th International Conference on Electronic Materials and Packaging, EMAP 2012*, no. figure 2, 2012.

[12] A. S. Holmes, "Laser processes for MEMS manufacture," *Proceedings of SPIE - The International Society for Optical Engineering*, vol. 4426, no. 43, pp. 203–209, 2002.

[13] M. C. Gower, "Laser micromachining for manufacturing MEMS devices," *MEMS Components and Applications for Industry, Automobiles, Aerospace, and Communication*, vol. 4559, no. October 2001, pp. 53–59, 2001.

[14] M. El-Bandrawy and M. Gupta, "Femtosecond laser micromachining of silicon for MEMS," *Proc. SPIE 4977, Photon Processing in Microelectronics and Photonics II*, vol. 4977, no. October 2003, pp. 219–225, 2003.

[15] C. Abbott, R. M. Allott, B. Bann, K. L. Boehlen, M. C. Gower, P. T. Rumsby, I. Stassen Boehlen, and N. Sykes, "New techniques for laser micromachining MEMS devices," *High-Power Laser Ablation IV*, vol. 4760, no. September 2002, pp. 281–288, 2002.

[16] M. R. H. Knowles, G. Rutterford, D. Karnakis, and A. Ferguson, "Micro-machining of metals, ceramics and polymers using nanosecond lasers," *International Journal of Advanced Manufacturing Technology*, vol. 33, no. 1-2, pp. 95–102, 2007.

[17] H. K. Tönshoff, C. Momma, A. Ostendorf, S. Nolte, and G. Kamlage, "Microdrilling of metals with ultrashort laser pulses," *Journal of Laser Applications*, vol. 12, no. 1, pp. 23–27, 2000.

[18] N. H. Rizvi, "Femtosecond Laser Micromachining: Current Status and Applications," *Optics Communications*, vol. 114, no. 1-2, pp. 5660–7, 2002.

[19] R. A. Lawes, A. S. Holmes, and F. N. Goodall, "The formation of moulds for 3D microstructures using excimer laser ablation," *Microsystem Technologies*, vol. 3, no. 1, pp. 17–19, 1996.

[20] J. Yeom, Y. Wu, J. C. Selby, and M. A. Shannon, "Maximum achievable aspect ratio in deep reactive ion etching of silicon due to aspect ratio dependent transport and the microloading effect," *Journal of Vacuum Science & Technology B: Microelectronics and Nanometer Structures*, vol. 23, no. 6, p. 2319, 2005.

[21] P. Jaecklin, C. Linder, N. F. D. Rooij, and R. Vuilleumier, "Optical Microshutters and Torsional Micromirrors for Light Modulator Arrays," *Cycle*, pp. 124–127, 2007.

[22] K. C. Yung, S. M. Mei, and T. M. Yue, "Rapid prototyping of polymer-based MEMS devices using UV YAG laser," *Journal of Micromechanics and Microengineering*, vol. 14, no. 12, pp. 1682–1686, 2004.

[23] W. C. Tang, T. C. H. Nguyen, and R. T. Howe, "Laterally driven polysilicon resonant microstructures," *Micromechanics and MEMS: Classic and Seminal Papers to 1990*, vol. 20, pp. 187–193, 1997.

[24] L. Lin, C.-C. Nguyen, R. Howe, and A. Pisano, "Microelectromechanical filters for signal processing," *Proceedings IEEE Micro Electro Mechanical Systems*, vol. 7, no. 3, pp. 226–231, 1992.

[25] J. N. Palasagaram and R. Ramadoss, "MEMS-capacitive pressure sensor fabricated using printed-circuit-processing techniques," *IEEE Sensors Journal*, vol. 6, no. 6, pp. 1374–1375, 2006.

[26] B. J. Janney, J. J. Christilda, and S. S. Mary, "MEMS Accelerometer Fabricated Using Printed Circuit Processing Techniques," in *IEEE International Symposium on Industrial Electronics*, pp. 3250–3254, 2007.

[27] M. Bachman, S. J. Kim, G.-P. Li, Y. Zhang, and M. Wang, "Latched microswitches in laminates for high power 0–6.5 GHz applications," *Electronics Letters*, vol. 50, no. 14, pp. 1010–1012, 2014.

[28] J. Henri, G. Han, B. Meint de, E. Miko, and F. Jan, "A survey on the reactive ion etching of silicon in microtechnology," *Journal of Micromechanics and Microengineering*, vol. 6, no. 1, p. 14, 1996.

[29] F. Marty, L. Rousseau, B. Saadany, B. Mercier, O. Français, Y. Mita, and T. Bourouina, "Advanced etching of silicon based on deep reactive ion etching for silicon high aspect ratio microstructures and three-dimensional micro-and nanostructures," *Microelectronics journal*, vol. 36, no. 7, pp. 673–677, 2005.

[30] A. Ayon, R. Bayt, and K. Breuer, "Deep reactive ion etching: a promising technology for micro-and nanosatellites," *Smart materials and structures*, vol. 10, no. 6, p. 1135, 2001.

[31] K. Fujimoto, N. Maeda, H. Kitada, Y. Kim, A. Kawai, K. Arai, T. Nakamura, K. Suzuki, and T. Ohba, "Development of multi-stack process on wafer-on-wafer (wow)," in *2010 IEEE CPMT Symposium Japan*, pp. 1–4, IEEE, 2010.

[32] A. Luque, J. M. Soto, F. Perdigones, C. Aracil, and J. M. Quero, "Electroosmotic impulsion device for integration in PCB-MEMS," *Proceedings of the 2013 Spanish Conference on Electron Devices, CDE 2013*, pp. 119–122, 2013.

[33] M. Bachman and G. P. Li, "MEMS in laminates," *Proceedings - Electronic Components and Technology Conference*, pp. 262–267, 2011.

[34] M. Bachman and G. Li, "Integrated mems in package," *Circuit World*, vol. 38, no. 4, pp. 184–192, 2012.

[35] Y. Shim, J. Ruan, Z. Wu, and M. Rais-Zadeh, "An integrated rf mems tunable filter," in *2012 IEEE 25th International Conference on Micro Electro Mechanical Systems (MEMS)*, pp. 15–18, IEEE, 2012.

[36] P. Goel, "Mems non-silicon fabrication technologies," *Sensors & Transducers*, vol. 139, no. 4, p. 1, 2012.

[37] M. Bachman and G.-P. Li, "Laminates for mems and biomems," in *2012 14th International Conference on Electronic Materials and Packaging (EMAP)*, pp. 1–5, IEEE, 2012.

[38] M. Maddela, R. Ramadoss, and R. Lempkowski, "A mems-based tunable coplanar patch antenna fabricated using pcb processing techniques," *Journal of Micromechanics and Microengineering*, vol. 17, no. 4, p. 812, 2007.

[39] A. Luque, G. Flores, F. Perdigones, D. Medina, J. Garcia, and J. Quero, "Single axis accelerometer fabricated using printed circuit board techniques and laser ablation," *Sensors and Actuators A: Physical*, vol. 192, pp. 119–123, 2013.

[40] J. Rogers, R. Ramadoss, P. Ozmun, and R. Dean, "A microelectromechanical accelerometer fabricated using printed circuit processing techniques," *Journal of Micromechanics and Microengineering*, vol. 18, no. 1, p. 015013, 2007.

[41] A. Cardenas-Valencia, J. Dlutowski, S. Knighton, C. Biver, J. Bumgarner, and L. Langebrake, "Aluminum-anode, silicon-based micro-cells for powering expendable mems and lab-on-a-chip devices," *Sensors and Actuators B: Chemical*, vol. 122, no. 1, pp. 328–336, 2007.

[42] J. P. Whitney, P. S. Sreetharan, K. Y. Ma, and R. J. Wood, "Pop-up book MEMS," *Journal of Micromechanics and Microengineering*, vol. 21, no. 11, 2011.

[43] P. A. York, N. T. Jafferis, and R. J. Wood, "Meso scale flextensional piezoelectric actuators," *Smart Materials and Structures*, vol. 27, no. 1, p. 015008, 2017.

[44] J. Lessing, A. C. Glavan, S. B. Walker, C. Keplinger, J. A. Lewis, and G. M. Whitesides, "Inkjet printing of conductive inks with high lateral resolution on omniphobic "rf paper" for paper-based electronics and mems," *Advanced Materials*, vol. 26, no. 27, pp. 4677–4682, 2014.

[45] J. A. Lewis, "Direct-write assembly of ceramics from colloidal inks," *Current Opinion in Solid State and Materials Science*, vol. 6, no. 3, pp. 245–250, 2002.

[46] C. W. Visser, R. Pohl, C. Sun, G.-W. Römer, B. Huis in 't Veld, and D. Lohse, "Toward 3d printing of pure metals by laser-induced forward transfer," *Advanced materials*, vol. 27, no. 27, pp. 4087–4092, 2015.

[47] C. G. K. Malek, "Su8 resist for low-cost x-ray patterning of high-resolution, high-aspect-ratio mems," *Microelectronics Journal*, vol. 33, no. 1-2, pp. 101–105, 2002.

[48] R. T. Howe, "Surface micromachining for microsensors and microactuators," *Journal of Vacuum Science & Technology B: Microelectronics and Nanometer Structures*, vol. 6, no. 6, p. 1809, 1988.

[49] J. W. Gardner, O. O. Awadelkarim, and V. K. Varadan, *Microsensors, MEMS, and Smart Devices.* Wiley New York, 2001.

[50] J. G. Korvink, *MEMS : A Practical Guide to Design , Analysis and Applications.* Springer Science \& Business Media, 2010.

[51] L. L. Wu, S. Babikian, G. P. Li, and M. Bachman, "Microfluidic printed circuit boards," *Proceedings - Electronic Components and Technology Conference*, pp. 1576–1581, 2011.

[52] B. H. Weigl, R. Bardell, T. Schulte, F. Battrell, and J. Hayenga, "Design and rapid prototyping of thin-film laminate-based microfluidic devices," *Biomedical Microdevices*, vol. 3, no. 4, pp. 267–274, 2001.

[53] B.N.Chichkov, C.Momma, S.Nolte, F. von Alvensleben, and A.Tiinnermann, "Femtosecond, picosecond and nanosecond laser ablation of solids," *Appl. Phys*, vol. 63, pp. 109–115, 1996.

[54] K. H. Leitz, B. Redlingshöer, Y. Reg, A. Otto, and M. Schmidt, "Metal ablation with short and ultrashort laser pulses," *Physics Procedia*, vol. 12, no. PART 2, pp. 230–238, 2011.

[55] D. Bauerle, *Laser Processing and Chemistry.* Springer Science \& Business Media, third ed., 2013.

[56] *Laser micromachining*, accessed August 10, 2019. `https://www.oxfordlasers.com/laser-micromachining/`.

[57] W. M. Steen and J. Mazumder, *Laser Material Porcessing.* springer science \& business media, 2010.

[58] R. Paschotta *et al.*, *Encyclopedia of laser physics and technology*, vol. 1. Wiley Online Library, 2008.

[59] *Optical Intensity*, accessed August 8, 2019. `https://www.rp-photonics.com/optical_intensity.html`.

[60] *Small Beam Diameter Scanning Galvo Mirror Systems*, accessed August 2, 2019. `https://www.thorlabs.com/thorproduct.cfm?partnumber=GVS202`.

[61] W. F. Hosford and R. M. Caddell, *Metal forming: mechanics and metallurgy.* Cambridge University Press, 2011.

[62] D. Karnakis, G. Rutterford, M. Knowles, T. Dobrev, P. Petkov, and S. Dimov, "High quality laser milling of ceramics, dielectrics and metals using nanosecond

and picosecond lasers," in *Photon Processing in Microelectronics and Photonics V*, vol. 6106, p. 610604, 2006.

[63] P. Heyl, T. Olschewski, and R. W. Wijnaendts, "Manufacturing of 3D structures for micro-tools using laser ablation," *Microelectronic Engineering*, vol. 57-58, pp. 775–780, 2001.

[64] J. Meijer, "Laser beam machining (LBM), state of the art and new opportunities," *Journal of Materials Processing Technology*, vol. 149, no. 1-3, pp. 2–17, 2004.

[65] D. Breitling, A. Ruf, and F. Dausinger, "Fundamental aspects in machining of metals with short and ultrashort laser pulses," *Photon Processing in Microelectronics and Photonics III*, vol. 5339, no. July 2004, p. 49, 2004.

[66] A. C. Forsman, P. S. Banks, M. D. Perry, E. M. Campbell, A. L. Dodell, and M. S. Armas, "Double-pulse machining as a technique for the enhancement of material removal rates in laser machining of metals," *Journal of Applied Physics*, vol. 98, no. 3, 2005.

[67] R. W. Pryor, *Multiphysics modeling using COMSOL: a first principles approach*. Jones & Bartlett Publishers, 2009.

[68] *Modeling thermal ablation for material removal*, accessed August 8, 2019. `https://www.comsol.com/blogs/modeling-thermal-ablation-for-material-removal/`.

[69] D. B. Go and A. Venkattraman, "Microscale gas breakdown: Ion-enhanced field emission and the modified Paschen's curve," *Journal of Physics D: Applied Physics*, vol. 47, no. 50, 2014.

[70] D. Landolt, "Fundamental Aspects of Electropolishing," *Ekcuochimiru Aore*, vol. 12, 1987.

[71] K. E. Petersen, "Silicon as a mechanical material," in *Proceedings of the IEEE*, vol. 70, pp. 420–457, IEEE, 1982.

[72] B. Wu, A. Kumar, and S. Pamarthy, "High aspect ratio silicon etch: A review," *Journal of Applied Physics*, vol. 108, no. 5, 2010.

[73] F. Brandi, N. Burdet, R. Carzino, and A. Diaspro, "Very large spot size effect in nanosecond laser drilling efficiency of silicon," *Optics Express*, vol. 18, no. 22, p. 23488, 2010.

[74] C. Molpeceres, S. Lauzurica, J. L. Ocãa, J. J. Gandía, L. Urbina, and J. Cárabe, "Microprocessing of ITO and a-Si thin films using ns laser sources," *Journal of Micromechanics and Microengineering*, vol. 15, no. 6, pp. 1271–1278, 2005.

[75] J. Kaspar, A. Luft, S. Nolte, M. Will, and E. Beyer, "Laser helical drilling of silicon wafers with ns to fs pulses: Scanning electron microscopy and transmission electron microscopy characterization of drilled through-holes," *Journal of Laser Applications*, vol. 18, no. 2, pp. 85–92, 2006.

[76] S. T. Hendow and S. A. Shakir, "Structuring materials with nanosecond laser pulses," *Optics Express*, vol. 18, no. 10, p. 10188, 2010.

[77] D. J. Lim, H. Ki, and J. Mazumder, "Mass removal modes in the laser ablation of silicon by a Q-switched diode-pumped solid-state laser (DPSSL)," *Journal of Physics D: Applied Physics*, vol. 39, no. 12, pp. 2624–2635, 2006.

[78] Y. H. Lee and K. J. Choi, "Analysis of silicon via hole drilling for wafer level chip stacking by UV laser," *International Journal of Precision Engineering and Manufacturing*, vol. 11, no. 4, pp. 501–507, 2010.

[79] H. Herfurth, R. Patwa, T. Lauterborn, S. Heinemann, and H. Pantsar, "Micromachining with tailored nanosecond pulses," *Photonics North 2007*, vol. 6796, no. October 2007, p. 67961G, 2007.

[80] D. Karnakis, G. Rutterford, and M. Knowles, "High power dpss laser micromachining of silicon and stainless steel," in *Proceedings of the Third International WLT-Conference on Lasers in Manufacturing*, no. June, 2005.

[81] J. H. Yoo, S. H. Jeong, X. L. Mao, R. Greif, and R. E. Russo, "Evidence for phase-explosion and generation of large particles during high power nanosecond laser ablation of silicon," *Applied Physics Letters*, vol. 76, no. 6, pp. 783–785, 2000.

[82] B. Wu, A. Kumar, and S. Pamarthy, "High aspect ratio silicon etch: A review," *Journal of Applied Physics*, vol. 108, no. 5, 2010.

[83] F. Beyeler, A. Neild, and S. Oberti, "Monolithically Fabricated Microgripper With Integrated Force Sensor for Manipulating Microobjects and Biological Cells Aligned in an Ultrasonic Field," *Journal of Microelectromechanical Systems*, vol. 16, no. 1, pp. 7–15, 2007.

[84] E. J. Garcia and J. J. Sniegowski, "Surface Micromachined Microengine as the Driver for Electromechanical Gears," *Eurosensors IX*, pp. 365–368, 1995.

[85] *Lynx Evo Eyepiece-less Stereo Microscope*, accessed August 10, 2019. `http://www.visioneng.us/products/stereo-microscopes/lynx-evo-dynascope-inspection/`.

[86] X. Xie and C. Livermore, "Passively self-aligned assembly of compact barrel hinges for high-performance, out-of-plane mems actuators," *Proceedings of the IEEE International Conference on Micro Electro Mechanical Systems (MEMS)*, pp. 813–816, 2017.

[87] X. Xie and C. Livermore, "A pivot-hinged, multilayer SU-8 micro motion amplifier assembled by a self-aligned approach," *Proceedings of the IEEE International Conference on Micro Electro Mechanical Systems (MEMS)*, vol. 2016-Febru, no. January, pp. 75–78, 2016.

[88] S. H. Lee, F. Niklaus, J. J. McMahon, J. Yu, R. J. Kumar, H.-f. Li, R. J. Gutmann, T. S. Cale, and J.-Q. Lu, "Fine Keyed Alignment and Bonding for Wafer-Level 3D ICs," *MRS Proc.*, vol. 914, pp. F10–05, 2006.

[89] M. Elwenspoek, R. Legtenberg, and a. W. Groeneveld, "Comb-drive actuators for large displacements," *Journal of Micromechanics and Microengineering*, vol. 6, no. 3, pp. 320–329, 1999.

[90] L. J. Durney, *Graham's Electroplating Engineering Handbook.* Springer Science & Business Media, 1984.

[91] V. Kaajakari, *Practical MEMS.* Small Gear Publishing, 2009.

[92] F. W. Strong, J. L. Skinner, P. M. Dentinger, and N. C. Tien, "Electrical breakdown across micron scale gaps in MEMS structures," *Reliability, Packaging, Testing, and Characterization of MEMS/MOEMS V*, vol. 6111, p. 611103, 2006.

[93] M. Klas, S. Matejík, B. Radjenović, and M. Radmilović-Radjenović, "Experimental and theoretical studies of the breakdown voltage characteristics at micrometre separations in air," *Epl*, vol. 95, no. 3, 2011.

[94] A. Hariri, J. W. Zu, and R. Ben Mrad, "Modeling of dry stiction in micro electro-mechanical systems (MEMS)," *Journal of Micromechanics and Microengineering*, vol. 16, no. 7, pp. 1195–1206, 2006.

[95] Y. X. Zhuang, O. Hansen, T. Knieling, C. Wang, P. Rombach, W. Lang, W. Benecke, M. Kehlenbeck, and J. Koblitz, "Vapor-phase self-assembled monolayers for anti-stiction applications in MEMS," *Journal of Microelectromechanical Systems*, vol. 16, no. 6, pp. 1451–1460, 2007.

[96] W. R. Ashurst, C. Carraro, and R. Maboudian, "Vapor phase anti-stiction coatings for MEMS," *IEEE Transactions on Device and Materials Reliability*, vol. 3, no. 4, pp. 173–178, 2003.

[97] T. P. Knowles, M. Vendruscolo, and C. M. Dobson, "The amyloid state and its association with protein misfolding diseases," *Nature Reviews Molecular Cell Biology*, vol. 15, no. 6, pp. 384–396, 2014.

[98] H. Jang, J. Zheng, R. Lal, and R. Nussinov, "New structures help the modeling of toxic amyloidß ion channels," *Trends in Biochemical Sciences*, vol. 33, no. 2, pp. 91–100, 2008.

[99] R. Andrew, ER and Bradbury, A and Eades, "Nuclear magnetic resonance spectra from a crystal rotated at high speed," *Nature*, vol. 182, no. 4650, p. 1658, 1958.

[100] M. Cohen, R. P. Feynman, and L. J. Lowe, "Physical Review Letters Free Induction Decays of Rotating Solids," *Phys. Rev. Lett*, vol. 2, no. 7, p. 71, 1957.

[101] C. P. Jaroniec, C. E. MacPhee, V. S. Bajaj, M. T. McMahon, C. M. Dobson, and R. G. Griffin, "High-resolution molecular structure of a peptide in an amyloid fibril determined by magic angle spinning NMR spectroscopy," *Proceedings of the National Academy of Sciences of the United States of America*, vol. 101, no. 3, pp. 711–716, 2004.

[102] R. Tycko, "Solid State NMR Studies of Amyloid Fibril Structure Robert," *Annual review of physical chemistry*, vol. 62, no. 1, pp. 279—-299, 2011.

[103] A. Böckmann, M. Ernst, and B. H. Meier, "Spinning proteins, the faster, the better?," *Journal of Magnetic Resonance*, vol. 253, pp. 71–79, 2015.

[104] T. Polenova1, R. Gupta, and A. Goldbourt, "Magic Angle Spinning NMR Spectroscopy: A Versatile Technique for Structural and Dynamic Analysis of Solid-Phase Systems," vol. 25, no. 3, pp. 289–313, 2016.

[105] S. Penzel, A. Oss, M. L. Org, A. Samoson, A. Böckmann, M. Ernst, and B. H. Meier, "Spinning faster: protein NMR at MAS frequencies up to 126 kHz," *Journal of Biomolecular NMR*, vol. 73, no. 1-2, pp. 19–29, 2019.

[106] E. Bouleau, P. Saint-Bonnet, F. Mentink-Vigier, H. Takahashi, J. F. Jacquot, M. Bardet, F. Aussenac, A. Purea, F. Engelke, S. Hediger, D. Lee, and G. De Paëpe, "Pushing NMR sensitivity limits using dynamic nuclear polarization with closed-loop cryogenic helium sample spinning," *Chemical Science*, vol. 6, no. 12, pp. 6806–6812, 2015.

[107] W. H. Potter, "Apparatus to rotate samples rapidly at temperatures less than 2 K in high transverse magnetic fields," *Review of Scientific Instruments*, vol. 42, no. 5, pp. 618–625, 1971.

[108] S. Wegner, *Solid State NMR News and Updates*, accessed August 10, 2019. https://www.bruker.com/fileadmin/user_upload/8-PDF-Docs/MagneticResonance/Events_NMR/UM_DE18/Solid_State_NMR_Workshop_2.pdf.

[109] J. Jensen, R. G. Stewart, W. Tuttle, and H. Brechna, *Brookhaven national laboratory selected cryogenic data notebook: sections I-IX*, vol. 1. Brookhaven National Laboratory, 1980.

[110] D. Olson, G. Reynolds, G. Virshup, F. Friedlander, B. James, and L. Partain, "Tensile strength of synthetic chemical- vapor-deposited diamond," *Journal of Applied Physics*, vol. 5177, no. August, 1995.

[111] A. G. Hamlir, B. J. Roberts, U. Kingdom, and A. Energy, "February 20, 1960," *Nature*, vol. 185, no. 4712, p. 522, 1960.

[112] A. D. Vita, G. Galli, A. Canningt, and R. Car, "Diamond-To-Graphite Transitions," vol. 379, no. February, pp. 523–526, 1996.

[113] C. Hedlund, H. Blom, and S. Berg, "Microloading effect in reactive ion etching," *Journal of Vacuum Science & Technology A: Vacuum, Surfaces, and Films*, vol. 12, no. 4, pp. 1962–1965, 1994.

[114] *University wafer*, accessed August 10, 2019. https://order.universitywafer.com.

[115] P. Ramm, J. J.-Q. Lu, and M. M. Taklo, *Handbook of wafer bonding.* John Wiley & Sons, 2011.

[116] S. Beeby, G. Ensel, N. M. White, and M. Kraft, *MEMS mechanical sensors.* Artech House, 2004.

[117] J. Henri, G. Han, B. Meint de, E. Miko, and F. Jan, "A survey on the reactive ion etching of silicon in microtechnology," *Journal of Micromechanics and Microengineering*, vol. 6, no. 1, p. 14, 1996.

[118] M. W. Judy and R. T. Howe, "Polysilicon Hollow Lateral Resonators," in *[1993] Proceedings IEEE Micro Electro Mechanical Systems*, pp. 265—-271, IEEE, 1993.

[119] Y.-H. Yoon, Y. Jin, C.-K. Kim, and S. Hong, "4-Terminal MEMS relay with an extremely low contact resistance employing a novel one-contact design," in *2017 19th International Conference on Solid-State Sensors, Actuators and Microsystems (TRANSDUCERS)*, pp. 906–909, IEEE, 2017.

[120] R. Nathanael, V. Pott, H. Kam, J. Jeon, E. Alon, and T. J. K. Liu, "Four-terminal-relay body-biasing schemes for complementary logic circuits," *IEEE Electron Device Letters*, vol. 31, no. 8, pp. 890–892, 2010.

[121] S. Farrens, *Wafer level 3-D ICs process technology.* Springer Science \& Business Media, 2009.

[122] S. H. Lee, K. N. Chen, and J. J. Q. Lu, "Wafer-to-wafer alignment for three-dimensional integration: A review," *Journal of Microelectromechanical Systems*, vol. 20, no. 4, pp. 885–898, 2011.

[123] B. T. Tung, N. Watanabe, F. Kato, K. Kikuchi, and M. Aoyagi, "Flip-chip bonding alignment accuracy enhancement using self-aligned interconnection elements to realize low-temperature construction of ultrafine-pitch copper bump interconnections," *Proceedings - Electronic Components and Technology Conference*, pp. 62–67, 2014.

[124] A. H. Slocum and A. C. Weber, "Precision passive mechanical alignment of wafers," *Journal of Microelectromechanical Systems*, vol. 12, no. 6, pp. 826–834, 2003.

[125] M. Stafe, A. Marcu, and N. Puscas, *Pulsed Laser Ablation of Solids: Basics, Theory and Applications*, vol. 53. Springer Science \& Business Media, 2013.

[126] K. Sugioka and Y. Cheng, "Femtosecond laser three-dimensional micro-and nanofabrication," *Applied Physics Reviews*, vol. 1, no. 4, 2014.

[127] A. A. Tseng, "Recent developments in micromilling using focused ion beam technology," *Journal of micromechanics and microengineering*, vol. 14, no. 4, p. R15, 2004.

[128] K. Watanabe, M. Kinoshita, T. Mine, M. Morishita, K. Fujisaki, R. Matsui, M. Sagawa, S. Machida, H. Oba, Y. Sugiyama, *et al.*, "Plasma ion-beam 3d printing: A novel method for rapid fabrication of customized mems sensors," in *2018 IEEE Micro Electro Mechanical Systems (MEMS)*, pp. 459–462, IEEE, 2018.

[129] M. Vaezi, H. Seitz, and S. Yang, "A review on 3D micro-additive manufacturing technologies," *International Journal of Advanced Manufacturing Technology*, vol. 67, no. 5-8, pp. 1721–1754, 2013.

[130] S. Maruo and K. Ikuta, "Submicron stereolithography for the production of freely movable mechanisms by using single-photon polymerization," *Sensors and Actuators, A: Physical*, vol. 100, no. 1, pp. 70–76, 2002.

[131] S. Maruo and K. Ikuta, "Movable microstructures made by two-photon three-dimensional microfabrication," in *MHS'99. Proceedings of 1999 International Symposium on Micromechatronics and Human Science (Cat. No. 99TH8478)*, pp. 173–178, IEEE, 1999.

[132] *Agilis Piezo Motor Driven Linear Stages*, accessed August 2, 2019. `https://www.newport.com/f/agilis-piezo-motor-linear-stages`.

[133] N. N. M. Peek, *Making machines that make: object-oriented hardware meets object-oriented software.* PhD thesis, Massachusetts Institute of Technology, 2016.

[134] *Machine That Makes*, accessed August 2, 2019. http://mtm.cba.mit.edu/.

[135] J. T. Schwartz, J. von Neumann, and A. W. Burks, "Theory of Self-Reproducing Automata," 2006.

[136] *Nimrod copper*, accessed August 10, 2019. https://www.nimrodcopper.com/shop/4-mil-copper-foils-(-004)-13250.